Radiation Pressure Acceleration and Laser Induced Focusing

Strahlendruckbeschleunigung und Lasergetriebene Fokussierung

Zur Erlangung des Grades eines Doktors der Naturwissenschaften (Dr. rer. nat.) genehmigte Dissertation von M.Sc. Peter Schmidt aus Wiesbaden
— Darmstadt 2016 — D 17

TECHNISCHE UNIVERSITÄT DARMSTADT

Fachbereich Elektrotechnik
und Informationstechnik
Institut für
Theorie Elektromagnetischer Felder

Radiation Pressure Acceleration and Laser Induced Focusing
Strahlendruckbeschleunigung und Lasergetriebene Fokussierung

Genehmigte Dissertation von M.Sc. Peter Schmidt aus Wiesbaden

1. Gutachten: Prof. Dr. rer. nat. Oliver Boine-Frankenheim
2. Gutachten: Prof. Dr. rer. nat. Wolfgang F. Ellermeier

Tag der Einreichung: 1. Juni 2016
Tag der Prüfung: 29. August 2016

Darmstadt — D 17

Erklärung zur Dissertation

Hiermit versichere ich, die vorliegende Dissertation ohne Hilfe Dritter nur mit den angegebenen Quellen und Hilfsmitteln angefertigt zu haben. Alle Stellen, die aus Quellen entnommen wurden, sind als solche kenntlich gemacht. Diese Arbeit hat in gleicher oder ähnlicher Form noch keiner Prüfungsbehörde vorgelegen.

Darmstadt, den September 14, 2016

(P. Schmidt)

Zusammenfassung

Seit Mitte der 80er Jahre hat sich das Feld der Laser-Plasma-Beschleunigung zu einem schnell wachsenden Forschungsgebiet entwickelt. Laserbeschleuniger sind lasergetriebene Linearbeschleuniger und zeichnen sich durch geringe Kosten, kompakte Bauweise und hohe Teilchen-Strahlintensität aus. Dabei hat sich die Strahlendruckbeschleunigung (engl. Radiation Pressure Acceleration, kurz RPA) als eine vielversprechende Methode zur Erzeugung hochintensiver Schwer- und Leichtionenstrahlen herausgestellt.

Gegenstand dieser Arbeit ist die Untersuchung der dynamischen Prozesse, die bei der RPA ablaufen. Die unterschiedlichen Laser-Beschleunigungsmechanismen gehen fließend ineinander über, die zum Erzielen eines bestimmten Mechanismus notwendigen Laser- und Plasmaparameter werden üblicherweise anhand von Erfahrungswerten angegeben. In dieser Arbeit wird die analytische Lücke geschlossen, indem die zum Erzielen einer RPA notwendigen Parameter in Form von analytische Gleichungen angegeben werden. Zu diesem Zweck werden die asymptotischen Grenzfälle des multi-Skalen-Problems untersucht.

Auf kurzen Skalen wird ein analytisches Kriterium für die untere Schranke der Zieldicke (engl. target) ermittelt: Im Gegensatz zu den Vorhersagen vorherrschender Modelle, wird für sehr dünne targets keine stärkere Beschleunigung erreicht. Stattdessen durchdringt der Laserpuls das Plasma und die Beschleunigung bricht zusammen.

Auf langen Skalen reduziert sich das Problem auf die Gleichungen der klassischen Gasdynamik. Aus diesem Model wird die zum Eintreten der RPA minimal nötige Laserintensität berechnet. Dieser Grenzwert separiert zugleich die RPA von anderen lasergetriebenen Beschleunigungsmechanismen. Zudem stellt diese Berechnung die Bedeutung der Elektronentemperatur heraus, die in vorhergehenden Arbeiten unterschätzt wurde.

Alle analytischen Modelle werden mit Simulationsergebnissen verglichen und überprüft. Die durchgeführten zweidimensionalen Simulationen zeigen, dass die Divergenz des bei der RPA entstehenden Plasmas in vorhergehenden Arbeiten unterschätzt wurde. Dieser Umstand motiviert die Entwicklung eines neuen Transportverfahrens für überkritische Plasmen, da sich magnetische Transportverfahren im Falle intensiver Plasmastrahlen als ungeeignet herausstellen. Das in dieser Arbeit entwickelte Transportverfahren verwendet einen gegenläufigen Laser und benötigt aus diesem Grund keine sperrigen Bauteile.

Abstract

Since the mid-80s, the field of laser plasma acceleration is a rapidly advancing field of research. Laser accelerators are laser driven LINACs and stand out due to low costs, compact design and high particle beam intensity. In particular, the radiation pressure acceleration (RPA) turns out to be a promising method for generating high intense heavy and light ion beams.

Subject of this work is the investigation of the dynamic processes occurring at the RPA. The transition between different acceleration mechanisms is fluent and the laser and plasma parameters required to achieve a certain mechanism are usually indicated by empirical values. In this work the analytical gap is closed by the derivation of analytic equations for the parameters required to achieve a RPA. For this purpose, the asymptotic limits of the multi-scale problem are investigated.

From the short scales limit, an analytical criterion for the lower target thickness is obtained: In contrast to the predictions of prevailing models, no increase of the acceleration is achieved for very thin targets. Instead, the laser pulse passes through the plasma and the acceleration collapses.

On large scales, the problem reduced to the equations of classical gas-dynamics. From this model one obtains the required minimum laser intensity to start a RPA. At the same time this limit separates the RPA from other laser-driven acceleration mechanisms. Moreover, this calculation emphasizes the significance of the electron temperature, which has been underestimated in previous work.

All analytical work is validated against simulation results. The two-dimensional simulations carried out in this work reveal that the divergence of the emerging plasma has been underestimated previously. This motivates the development of a new transport method for super-critical plasmas, since traditional transport methods, e.g. solenoids, turn out to be unsuitable for intense plasma jets. The unconventional transport method developed in this work uses a counter-propagating laser and therefore requires no bulky components.

Contents

1 Introduction

Particle beams are a common tool in science, industry and medicine. Commonly, high energy particle beams are generated with traditional accelerators, e.g. cyclotrons or synchrotron accelerators. Applications in fundamental particle physics, radiography diagnostics and radio therapy in medicine, advance the development of particle accelerators. Besides classic accelerators, the non-traditional laser plasma accelerators are an active field of research[1] since the late 1980s.

Due to the rapid advance in laser technology, a variety of high power pulsed lasers have become available for scientific applications. Laser intensities $I > 10^{18}\,\mathrm{W/cm^2}$ have been first achieved in 1985 by applying the chirped pulse amplification (CPA) [2]. For these laser intensities, field ionization occurs and a plasma forms in laser matter interaction. By that, scientists enter the field of laser plasma physics and in particular, the field of laser plasma acceleration. Worldwide experimental [3, 4, 5] and theoretical [6, 7, 8] effort in the research fields of laser- and plasma physics rapidly advances the frontier of laser driven electron- and ion acceleration. Particularly, the discovery of new acceleration mechanisms for laser driven ion acceleration drives the research efforts.

One of the latest acceleration mechanisms is the *Radiation Pressure Acceleration* (RPA), that is subject of the present work. Simulations predict high intense, heavy ion beams with narrow band kinetic energies up to GeV, generated within a distance of a few microns on a sub-pico-second temporal scale by pulsed Petawatt lasers. The capability of generating high intense particle beams with a desktop size setup using high intense, pulsed power lasers leads to a variety of proposed applications [9, 10], e.g. the generation of warm dense matter states for material science, the generation of proton beams for proton radiography, the generation of intense light and heavy ion beams for tumor radiotherapy, the generation of ion beams as a driver for polarized neutron sources, to mention only a few.

Compared to traditional accelerator and particle sources, laser accelerators are characterized by their small dimension, low cost and high beam intensities combined with a high total amount of particles. These advantages are balanced by a large shot to shot variation of the beam intensity, as well as a worse beam quality in terms of divergence and energy spread, compared to classic accelerators and ion sources.

1.1 Laser acceleration setup

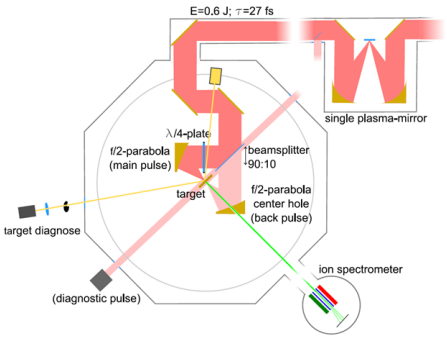

Figure 1.1.: Schematic of the experimental setup used by [3]: The laser is focused onto a small film target, the emerging plasma is diagnosed by several detectors. The setup has an approximate diameter of half a meter. Taken from [3].

Basically, laser plasma acceleration can be divided into two different branches: Electron- and ion accelerators, where the latter may be sub-divided into light ion and heavy ion acceleration. A typical setup of a laser plasma accelerator is shown in fig. 1.1: A high power pulsed laser is focused on a target, generates a plasma and drives the acceleration. Subsequent to the acceleration stage the plasma drifts and is diagnosed. In order to compensate the transverse divergence of the plasma, the beam line is completed with transport elements, e.g. solenoids.

The basic setup is very similar for all types of laser accelerators. The main difference between one type of laser driven accelerator and another one are the target and laser parameters. This reveals another strength of laser accelerators: one type of laser driven plasma accelerator can be converted into another type by slightly changing, e.g. the target type and the laser intensity without the necessity of rebuilding the surrounding setup. For example a laser driven electron wakefield accelerator[11, 12] can be converted into a light ion accelerator. Today (time: September 14, 2016) state of the art high power pulsed lasers are capable of producing laser pulses with intensities of $I \approx 10^{21}\,\mathrm{W/cm^2}$ and pulse durations of $50 - 500\,\mathrm{fs}$[13], with a total energy of $W_{EM} \approx 100\,\mathrm{J} - 1\,\mathrm{kJ}$ per pulse. The focal spot has a diameter of $\approx 2 - 10\lambda$ [14, 15] and $\lambda = 800\,\mathrm{nm} - 1\,\mu\mathrm{m}$ [5] is a usual wavelength. Petawatt-lasers with field strengths of $10^{12} - 10^{14}\,\mathrm{V/m}$ are capable of generating MeV light ion beams within a distance of only a few microns on a sub-pico-second time scale. The most prominent laser ion acceleration mechanism,

the *Target Normal Sheath Acceleration* (TNSA)[16, 17, 6, 18, 19] is subject of high experimental and theoretical effort. For the TNSA, a linearly polarized (LP) laser with an intensity $I = 10^{19} - 10^{20}\,\mathrm{W/cm^2}$ [20] and a pulse durations of $100 - 500\,\mathrm{fs}$ is focused on a micrometer scale metal or plastic target. Electrons heated by the laser penetrate the entire target and accelerate a contamination layer of light particles, e.g. hydrogen/protons on the target rear surface by an electrostatic field. The protons are accelerated to energies of $3 - 50\,\mathrm{MeV}$ [21, 22, 23] with an exponentially decaying spectrum. Thereby, the achievable maximum kinetic energy scales with the laser intensity as $W_{kin} \propto (I\lambda^2)^{1/2}$ [24].

Apart from the mentioned processes, there are many different mix-regimes using compound or multiple-layer targets, or special shaped laser pulses. A deeper treatment of all acceleration mechanisms is beyond the scope of this work, the interested reader is referred to: compound targets[25], three-stage acceleration using multiple-layer targets [26, 27], *Dual-Peaked Electrostatic-Field Acceleration* (DPEFA) [28] and the Break Out Afterburner (BOA) [29, 30], to mention only a few.

1.2 Radiation pressure acceleration

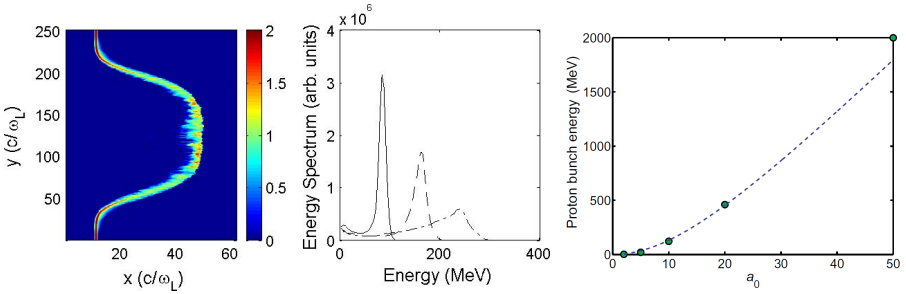

(a) Light sail plasma (left), and energy (right) for different times achieved with RPA. Taken from [31].

(b) Achievable ion energy with RPA as a function of the acceleration parameter $A_0 \propto I\tau$. Taken from [32].

Figure 1.2.: Plasma density, energy and energy scaling for RPA in the light sail regime. The achievable energy scales with $W_{kin} \propto I^2$.

Upcoming laser plasma facilities, such as the **Jü**lich **S**hort-**P**ulsed p**A**rticle and **R**adiation **C**enter (JuSPARC) will operate a new generation of high power pulsed lasers with intensities $I > 10^{21}\,\mathrm{W/cm^2}$ and repetition rates of $0.1\,\mathrm{Hz} - 10\,\mathrm{kHz}$.

For laser intensities above $I > 10^{21}\,\mathrm{W/cm^2}$ and target widths of $L \propto 10\text{—}100\,\mathrm{nm}$, theoretical studies [33] predict a new acceleration mechanism: The *Radiation Pressure Acceleration* (RPA) [34, 35, 36, 37], which is subject of this work. Within this acceleration mechanism, the laser pulse ionizes the film target and the radiation pressure of the laser pulse „pushes“ the resulting plasma and the entire target is accelerated.

Figure 1.2a shows simulation results for the plasma density and energy distribution achieved by RPA: Simulations predict heavy ion plasma beams with ideally narrow band energy spectra up to GeV energies and nearly solid body densities, identified as *light sail regime* [38, 39]. The achievable maximum energy scales with $W_{kin} \propto (I\lambda^2)^2$[40] (cf. fig. 1.2b), making the RPA a promising method for generating high energy particles beams[1]. For that reason, high experimental effort[41, 42, 43, 44, 45] is pursued on achieving a stable light sail RPA, e.g. at the Helmholtzinstitut Jena (see also fig. 1.1 for setup used). At the Helmholtzinstitut Jena, the JETI40 Laser (**Je**naer **Ti**tan:Saphir **40** Terawatt)[3, 4] system is used to experimentally investigate the RPA.

1.3 Motivation

Existing analytical models predict a light sail acceleration for a wide range of laser and target parameters. Figure 1.3 shows the energy spectra obtained in the experiment at the Helmholtzinstitut Jena (setup shown in fig. 1.1) in comparison with the energy distribution obtained from computer simulation[32]: Contrary to the prediction of the prevalent models, the experimentally obtained energy spectra are far-off a sharp peak spectrum. This indicates, that a RPA in the light sail regime has not been achieved yet. Additionally, computer simulations reveal the requirement of certain laser and target parameters in order to obtain a RPA. However, these parameters are obtained by empirical values, rather than from analytical theory. These indications reveal that the prevalent analytical models are deficient and the RPA has not been fully understood yet.

In order to explore the RPA dynamics not covered by the inadequate prevalent models, this work addresses the development of advanced models and aims at bridging the analytical gap. Particularly, the RPA dynamics splits into small scale dynamics, dominated by the electrodynamics of the plasma electrons and large scale dynamics, dominated by the gas-dynamic properties of the plasma. Both sections are evaluated analytically in this work, supported by Particle In Cell (PIC) simulations, performed with the simulation software package VSim© [46]. As mentioned in section 1.1, the setup for the different laser ion acceleration mechanisms

[1] Precisely speaking, this scaling law fits for non-relativistic ion energies. For higher energies, the scaling is $E_{kin} \propto (I\lambda^2)^\alpha$, where $\{\alpha \in \mathbb{R} : 1 < \alpha < 2\}$ holds.

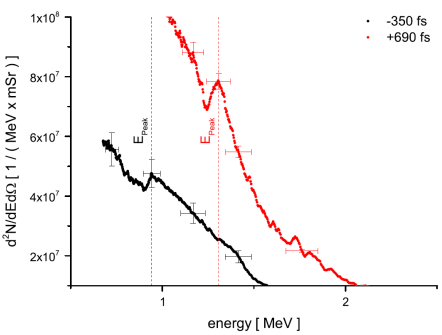

(a) Ion energy spectra experimentally obtained at the Helmholtzinstitut Jena: The small, marked peak indicates the occurrence of radiation pressure acceleration. From [3]

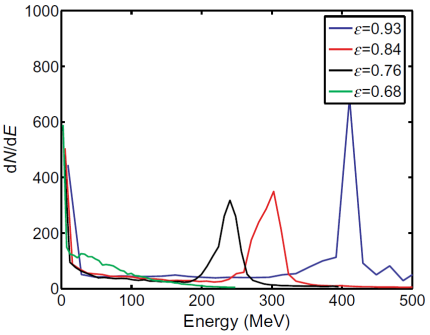

(b) One dimensional simulation results for RPA for different target materials and laser parameters. Simulations predict sharp peak spectra with energies up to several 100 MeV. From [32].

Figure 1.3.: Ion energy spectra obtained experimentally and by PIC simulation. Clearly visible is severe difference.

is very similar. This raises the question, for which target and laser parameters one acceleration mechanism turns over to another one. Obviously, the transition from one to another acceleration mechanism is fluent and also strongly depends on the polarization of the laser. In this work, analytical scaling laws are derived, that fix the requirements for laser and target parameters precisely, e.g. to obtain a RPA in the light sail regime. Within this context, the gas dynamics approach to the RPA reveals the importance of the electron temperature in the plasma, which was formerly given less importance: a condition is worked out which directly connects the required laser intensity with the electron density and temperature.

Ideally, a narrow band energy spectrum is produced by RPA, as shown in fig. 1.3b. Consequently, the optimization of the RPA in terms of energy spread is also part of the present work. Contrary to previous conjectures, the short scale analysis demonstrates that longer laser pulses substantially reduce the beam energy spread compared to short laser pulses with an equivalent pulse energy. The two dimensional investigation of the RPA confirms existing results[33] that the divergence of the emerging plasma has been formerly underestimated. In addition, an analytical expression for the divergence angle is given.

This observation also serves as a motivation for the development of a non-traditional transport concept for over-dense plasma beams: As usual experimen-

tal setups involve beam lines with spatial dimensions of cm to m, beam transport methods are required. However, it turns out, that traditional transport elements, e.g. magnetic focusing devices such as solenoids are not suitable for RPA generated plasma beams. From the point of view of scales, it seems consistent, that a plasma generated by a high power pulsed laser may also be focused and transported by such. For this reason, the second part of this work presents the advanced transport method of *laser induced focusing* (LIF).

1.4 Organization of the thesis

To simplify the handling with the thesis, this section provides a short outline. Chapter 2 introduces a classification of laser plasmas in comparison with other plasma branches and introduces the most prominent plasma quantities, namely the electron density and temperature, as well as the so called plasma parameter. Particularly, the plasma model used across this work is presented. The subsequent section 2.2 continues the introduction of the most important quantities and glossary, including an overview of the typical scales of all RPA related quantities. Section 2.3 contains a rough approximation for the average ion charge state and the electron-ion collision frequency in a RPA plasma in order to justify the postulated plasma model.

Chapter 3 starts with a brief introduction of the prevalent analytical models in section 3.1, followed by the derivation of the more adequate analytical models used in the present work: section 3.2 give a brief overview of the related electrodynamics, as well as general coordinate transformation, followed by the most general representation of a relativistic two fluid model in section 3.3. Reduced models are obtained for different asymptotic limits in the subsequent sections. After the introduction of the simulation software VSim© [46] in chapter 4, the relation of entropy production and laser polarization is examined in chapter 5. The RPA is further investigated in one-dimensional investigation in 6: the examination of the short scale effects in section 6.2 reveals the advantage of long laser pulses compared to short laser pulses, whereas important conditions for laser and target parameters are obtained from the large scale analysis in section 6.3. The two dimensional (2D) investigation of the RPA in chapter 7 starts with the validation of the previously derived conditions for the 2D process, followed by the examination of the beam divergence.

Motivated by the divergence, chapter 8 presents a non-traditional cure for the divergence in terms of a laser driven focusing method. The work is finalized by the conclusions in chapter 9. The appendix contains additional information, long formulas and derivations to all chapters presented.

2 Laser plasmas

This chapter provides the most prominent quantities characterizing a plasma. The orders of magnitude related to radiation pressure acceleration (RPA) are listed in table 2.1.

2.1 Classification of laser plasmas

Any fully or partially ionized gas, whose dynamics is dominated by the electromagnetic interaction of its accompanied free charges, is identified as an *ideal plasma*. Since a plasma always contains free charges, it thus has an electric conductivity. Due to the fact that a plasma can be generated by an additional energy input into a gas, a plasma is often referred to as the 4^{th} state of matter. Besides this definition, there exist many other in literature, that extend the term plasma based on its properties (see e.g. [47, 48, 49, 50]).

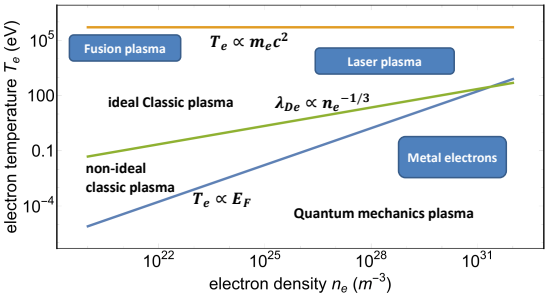

Figure 2.1.: Classification of laser plasmas by their characteristic electron temperature T_e and electron number density n_e in comparison with other plasmas.

A plasma is characterized by its electron number density n_e and the related electron temperature T_e. Figure 2.1 shows a map for characterizing plasmas: Plasma physics is roughly divided into three branches: *Classic ideal plasmas* have a *plasma parameter* $N_D \gg 1$, whereas plasmas satisfying $N_D \ll 1$ are identified as *non-ideal classic plasmas*.

Across this work, ideal, classic and collisionless plasmas are assumed. A justification of these assumptions is given in this chapter.

The *plasma parameter* N_D is defined as the number of electrons in a *Debye sphere* [48]:

$$N_D = \frac{4}{3}\pi\lambda_D^3 n_e. \tag{2.1}$$

The Debye sphere is a sphere where the radius equals the *Debye length*, defined as [48]:

$$\lambda_D = \sqrt{\left(\frac{n_e e^2}{\epsilon_0 k_B T_e} + \frac{n_i Z^2 e^2}{\epsilon_0 k_B T_i}\right)^{-1}}. \tag{2.2}$$

The Debye length relates the electron density and temperature and defines a radius or length[1], above which a charge fluctuation is shielded[2]. For typical laser plasmas the electron temperature T_e is much larger than the ion temperature, $T_e \gg T_i$. For fast oscillating fields the Debye length simplifies to the *electron Debye length* [49]:

$$\lambda_D \approx \lambda_{De} = \sqrt{\frac{\epsilon_0 k_B T_e}{n_e e^2}}, \tag{2.3}$$

where ϵ_0 is the vacuum permittivity, k_B is the Boltzmann constant, $n_i = n_i(\vec{x}, t)$ is the number density of the ions, Z is the charge number of the ions and $n_e = n_e(\vec{x}, t)$ is the electron number density. If the plasma expansion L is much larger than the Debye length $L \gg \lambda_D$, the plasma is *quasi neutral* and the charge fluctuation is small compared to the overall electron density[47]:

$$\frac{Z n_i - n_e}{n_e} \ll 1. \tag{2.4}$$

In case the electron thermal energy is in the region of the electron rest mass $f k_B T_e/2 \propto m_e c^2$ (cf. fig. 2.1), the contribution of the thermal energy to the electron's mass density is not negligible and the plasma is relativistic. *Cold plasmas* with an electron thermal energy in the region of the Fermi Energy $f k_B T_e/2 \propto E_F$ (cf. fig. 2.1) may be treated as ideal Fermi gases and the physics is governed by quantum mechanics. Typically, laser plasmas are ideal with a thermal energy below the relativistic limit but much larger than the Fermi energy, so that quantum mechanical effects are negligible.

[1] Depending on the dimension and geometry treated.

[2] More precisely speaking, λ_D is the distance for which the electrical potential of the source charge drops by a factor of $1/e$.

2.2 Properties of RPA plasmas

If an electron is displaced in a quasi-neutral plasma, it will start oscillating with the electron plasma frequency:

$$\omega_{pe} = \sqrt{\frac{n_e e^2}{\epsilon_0 \gamma_e m_e}}. \tag{2.5}$$

Here $\gamma_e = 1/\sqrt{1-u_e^2/c^2}$ denotes the electron's Lorentz factor. This oscillation will excite Langmuir waves, which follow the BOHM-GROSS DISPERSION RELATION[3] [51]:

$$\omega^2 = \omega_{pe,0}^2 + a_e^2 k^2, \tag{2.6}$$

where $a_e = \sqrt{\varkappa_e k_B T_e / m_e}$ is the electron speed of sound. The electron plasma frequency is directly connected to the electron relaxation time $\tau_{relax} \propto 1/\omega_{pe}$, which determines the time scale on which a charge perturbation in a plasma is canceled out by an electron redistribution. For a given laser frequency ω, the *critical electron density* n_c is defined as the electron density for which the plasma frequency equals the laser frequency: $\omega = \omega_{pe}$. From the definition of the plasma frequency one obtains:

$$n_c = \frac{\gamma_e \epsilon_0 m_e \omega^2}{e^2} \tag{2.7}$$

Plasmas with $n_e > n_c$ are referred to as over-dense to the laser, while the case $n_e < n_c$ is identified as a thin plasma. For the RPA highly over-dense plasmas with electron density of $n_e \cong 100 - 1000 n_c$ are required.

Figure 2.2 illustrates the interaction of an electromagnetic (EM) wave with an over-dense plasma: In the plasma, the electromagnetic wave is evanescent rather than a propagating wave and the field amplitude attenuates exponentially. Hence, the EM wave will penetrate the plasma up to a *skin-depth*

$$\delta = c/\omega_{pe}. \tag{2.8}$$

The skin-depth is also identified as *penetration depth*. For typical RPA plasmas, the skin-depth is much smaller than the dimension of the plasma slab $\delta \ll L$. This section is finalized by a summary of the typical RPA plasma parameters, given in table 2.1.

[3] The Bohm-Gross dispersion relation is also known as the dispersion relation for the Klein-Gordon-Equation.

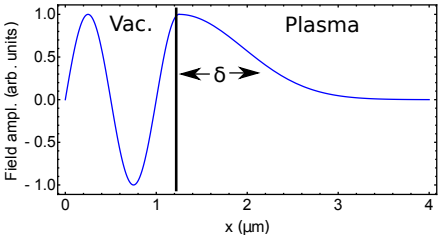

Figure 2.2.: Interaction of an electromagnetic wave (blue line) with an over-dense plasma: In the plasma the electromagnetic wave is evanescent and attenuates exponentially. The plasma skin-depth δ defines the distance at which the wave amplitude has dropped by a factor of $\mathrm{e} \approx 2.71$.

Table 2.1.: Summary of the typical RPA plasma parameters.

$n_e(\times 10^{30}\,\mathrm{m}^{-3})$	$\lambda_{De}\,(\mathrm{nm})$	ω_{pe}/ω	$\delta\,(\mathrm{nm})$	$I(\times 10^{20}\,\mathrm{W/cm^2})$	$\tau_L\,(\mathrm{fs})$
$0.1-10$	$0.1-10$	$10-100$	$1-10$	$1-20$	$50-500$

2.3 Charge state and collisions in laser plasmas

For this work, a collisionless, ideal plasma consisting of only one ion species with maximum charge state is assumed. Therefore, this section provides a rough approximation for the average charge state, as well as for the electron-ion collision frequency in order to justify the assumptions. A plasma is characterized by the fact that it consists of free charge carriers. Therefore the electrons' thermal energy has to be much larger than the ionization energy of the plasma atoms, $W_{e,th} \gg W_i$. Otherwise recombination would lead to a dilution of the free charge carriers after some time. Identifying the electrons as an ideal gas of f degrees of freedom, $W_{e,th} = f/2 k_B T_e$ is the electron thermal energy. From this, one obtains the condition:

$$T_e \gg \frac{2W_i}{f\,k_B} \tag{2.9}$$

A numerical example provides an estimate for the order of magnitude of the electron temperature: consider a plasma of fully ionized carbon ions and the corresponding electrons. The maximum ionization energy of carbon is $W_i \approx 490\,\mathrm{eV}$,

which corresponds to an electron temperature of $T_e \gg 3.8 \cdot 10^6\,\mathrm{K}$ for $f = 3$. Given the initial number density of the neutral atoms n_A and the average ionization energy $\bar{W}_i$, the average charge state in the plasma is obtained from SAHA EQUATION[52]:

$$\bar{Z} = \frac{2}{n_A}\left(\frac{m_e k_B T_e}{2\pi\hbar^2}\right)^{3/2} \exp\left(-\frac{\bar{W}_i}{k_B T_e}\right) \tag{2.10}$$

By applying condition Eq. 2.9, expression 2.10 simplifies to:

$$k_B T_e \gg W_i \rightarrow \bar{Z} \approx \frac{2}{n_A}\left(\frac{m_e k_B T_e}{2\pi\hbar^2}\right)^{3/2} \propto 10^3 - 10^4, \tag{2.11}$$

where the numerical value applies to typical RPA parameters. Since the estimate value $\bar{Z}$ from Eq. 2.11 is much larger than the maximum achievable charge state of any atom, it is reasonable to assume fully ionized plasmas without recombination. A description of the specific ionization mechanisms is beyond the scope of this work. Hence the interested reader is referred to the common literature. As from now on, the target is assumed to be ionized ab initio instead. In case the electron-electron collision frequency ν_{ee}, electron-ion collision frequency ν_{ei}[49] and the ion-ion collision frequency ν_{ii} are negligible compared to the plasma frequency $\nu_{ee}, \nu_{ei}, \nu_{ii} \ll \nu_{pe}$ the plasma is identified as non-collisional. The electron ion collision frequency is[52]:

$$\begin{aligned} \nu_{ei} &= \frac{4}{3}\frac{\sqrt{\pi} n_e e^4 \ln(\Lambda)}{(4\pi\epsilon_0)^2 \sqrt{m_e}(k_B T_e)^{3/2}}, \quad \Lambda = \frac{3}{2}\frac{(k_B T_e)^{3/2}}{\sqrt{4\pi n_e} e^3} \\ \rightarrow \nu_{ei} &\approx \frac{1}{16}\frac{\ln(\Lambda)}{\Lambda}\nu_{pe} \propto 10^{11}\,\mathrm{s}^{-1} \ll \nu_{pe} \propto 10^{16}\,\mathrm{s}^{-1} \end{aligned} \tag{2.12}$$

Given that $\nu_{ei} \approx \nu_{ee}$, $\nu_{ii} \ll \nu_{ei}$ and $\nu_{ei} \ll \nu_{pe}$, the plasma is assumed as non-collisional. Moreover, the electric and thermal resistivity caused by collisions are negligible for $\nu_{ei} \ll \nu_{pe}$.

Hence, the present work assumes collisionless, fully ionized plasmas.

3 Analytical models for the radiation pressure acceleration

This section contains the derivation of the analytical models used across this work. The introduction of Maxwell's Equations is followed by a brief overview over coordinate transformations, followed by the introduction of the co-variant two fluid picture of a plasma. Subsequently, this set (PDE) equations is gradually reduced to a more manageable size.

3.1 The prevalent model of a flying mirror

This sections presents an abbreviated derivation of the prevalent *Flying Mirror Model* also identified as *light sail model* [53, 32]. The interested reader is referred to the literature for details. The RPA is modeled as a relativistic, ideal mirror (reflective index $R = 1$), accelerated by the radiation pressure $p_L = 2I/c$ of the laser in one dimension. The relativistic equations of motion are:

$$d_t \gamma\beta = \frac{1-\beta}{1+\beta}\frac{2I(x-\beta ct)}{\rho Lc}, \quad d_t x = \beta c, \tag{3.1}$$

where $\rho = const$ is the target density, $L = const$ is the target thickness, $\beta = u/c$ is the target u velocity with respect to the speed of light c and $I(x-\beta ct)$ is the retarded laser intensity.

3.2 Electrodynamics

This section contains the basic concepts for the electrodynamic description of a plasma. By definition, a plasma consists of mobile charge carriers (e.g. ions and electrons). Thus, a plasma is capable of interacting with electromagnetic field, as well as emitting electromagnetic fields itself. The description of a plasma is thus always connected to the well known macroscopic Maxwell's Equations [54]:

$$\begin{aligned} \text{Amperè's Law:} \quad & \nabla \times \vec{H} = \vec{j} + \partial_t \vec{D} \\ \text{Faraday's Law:} \quad & \nabla \times \vec{E} = -\partial_t \vec{B} \\ \text{Gauss' Laws:} \quad & \nabla \cdot \vec{D} = \rho_{el}, \quad \nabla \cdot \vec{B} = 0, \end{aligned} \tag{3.2}$$

where $\vec{H} = \vec{H}(\vec{x}, t)$ is the magnetic field strength, $\vec{D} = \vec{D}(\vec{x}, t)$ is the electric displacement field, $\vec{E} = \vec{E}(\vec{x}, t)$ is the electric field strength and $\vec{B} = \vec{B}(\vec{x}, t)$ is the magnetic flux density. The sources of the field are the current density $\vec{j} = \vec{j}(\vec{x}, t)$ and the charge density $\rho_{el} = \rho_{el}(\vec{x}, t)$. This system of PDEs is completed by a set of material laws $B = B(H)$ and $D = D(E)$, equations for the current- and charge density, as well as a set of proposed boundary and initial conditions. In the two fluid picture, the plasma consists of an electron gas, with density $n_e = n_e(\vec{x}, t)$ and velocity field $\vec{u}_e = \vec{u}_e(\vec{x}, t)$ and a respective ion gas, with density $n_i = n_i(\vec{x}, t)$ and velocity field $\vec{u}_i = \vec{u}_i(\vec{x}, t)$. The definitions

$$\begin{aligned} \vec{j} &= \vec{j}_i + \vec{j}_e = Zen_i\vec{u}_i - en_e\vec{u}_e \\ \rho_{el} &= Zen_i - en_e, \end{aligned} \tag{3.3}$$

together with the isotropic, linear material laws

$$\vec{B} = \mu_0\vec{H}, \quad \vec{D} = \epsilon_0\vec{E}, \tag{3.4}$$

complete the Maxwell Equations 3.2[54]. In the two fluid picture, the continuity equation of electrodynamics is a direct consequence of the electrons and ions continuity equations:

$$\Rightarrow \partial_t(Zen_i - en_e) + \nabla \cdot (Zen_i\vec{u}_i - en_e\vec{u}_e) = \partial_t\rho_{el} + \nabla \cdot \vec{j} = 0 \tag{3.5}$$

Within this formalism, material laws are a result of the electron dynamics consistently. Another advantage of the two-fluid model is, that the relativistic generalization of the electrodynamic equations is much more straight forward. Within laser plasma acceleration one is often confronted with particle velocities of a substantial fraction of the speed of light. Therefore, the *4-vector notation*, LORENTZ TRANSFORMATION and *general coordinate transformation* are briefly introduced. However, an extensive treatment is beyond the scope of this work and the interested reader is referred to the common literature [54, 55]. In order to perform a Lorentz transformation of the Maxwell's Equations and the fluid equations, it turns out to be very beneficial to rewrite all quantities and equations in 4-vector notation in the MINKOWSKI SPACE[1] $\mathbb{M}^4$. Defining the 4-current $j^\alpha = (c\rho_{el}, \vec{j})^T$ and the *Field Strength Tensor* $F^{\alpha\beta}$

[1] For more details, see appendix A.

$$F^{\alpha\beta} = \begin{pmatrix} 0 & -E_x/c & -E_y/c & -E_z/c \\ E_x/c & 0 & -B_z & B_y \\ E_y/c & B_z & 0 & -B_x \\ E_z/c & -B_y & B_x & 0 \end{pmatrix}, \tag{3.6}$$

the Maxwell Equation 3.2 and 3.3 in 4-vector notation are:

$$\begin{aligned} \partial_\alpha F^{\alpha\beta} &= \mu_0 \left(j_e^\beta + j_i^\beta \right) \\ \epsilon^{\alpha\beta\gamma\delta} \partial_\beta F_{\gamma\delta} &= 0, \end{aligned} \tag{3.7}$$

where the relation $c^{-2} = \mu_0 \epsilon_0$ is used. All Greek indices run from zero to three $\alpha, \beta = 0, 1, 2, 3$ and EINSTEIN NOTATION is used (cf. appendix A). However, the linear Lorentz Transformation can only be applied to non-accelerated inertial systems. Unfortunately, accelerated inertial systems frequently occur in laser plasma acceleration and the particle velocity field $\vec{u} = \vec{u}(\vec{x}, t)$ depends on space and time with $\nabla \times \vec{u} \neq 0$. Accordingly, the most general system treated is rotational, which can not be described by the above presented Lorentz Transformation. In fact one has to perform a general coordinate transformation in RIEMANN SPACE[2]. The co-variant formulation of the Maxwell's Equations 3.7 and the continuity equation 3.5 read:

$$\begin{aligned} \frac{1}{\sqrt{|g|}} \partial_\mu \sqrt{|g|} F^{\mu\nu} &= \mu_0 \left(j_e^\nu + j_i^\nu \right) \\ \epsilon^{\alpha\beta\gamma\delta} \partial_\beta F_{\gamma\delta} &= 0 \\ \partial_\mu \sqrt{|g|} j^\mu &= 0 \end{aligned} \tag{3.8}$$

Here, $g^{\mu\nu}$ is the *metric tensor* and $|g| = |\det(g^{\mu\nu})|$ denotes the absolute value of the determinant of the metric tensor. The homogeneous Maxwell Equations remain unchanged. Applying the chain rule to the above equations, one obtains:

$$\begin{aligned} \partial_\mu F^{\mu\nu} - \mu_0 \left(j_e^\nu + j_i^\nu \right) &= -\frac{1}{2} \frac{1}{|g|} F^{\mu\nu} \partial_\mu |g| \\ \partial_\mu j^\mu &= -\frac{1}{2} \frac{1}{|g|} j^\mu \partial_\mu |g| \end{aligned} \tag{3.9}$$

The left hand side of each equation corresponds to the Lorentz invariant Maxwell's equations (cf. Eqs. 3.7), whereas the right hand side contains gyroscopic sources.

[2] More details are provided in appendix A.

3.3 Fluid picture of a plasma

A plasma is a state of matter, where positive and negative charge carriers are loosely bound and mobile. For an ideal plasma it is additionally required that the expansion of the plasma is much larger than the electron Debye length and the plasma parameter is much larger than one. Typically, the number of particles (electrons and ions) in a plasma is very large. It is thus reasonable to apply a continuity description to the plasma. The simplest two fluid plasma consists of one ion species with the corresponding electrons and the co-variant description in 4-tensor notation yields:

$$\partial_\nu T_k^{\mu\nu} - F^{\mu\nu} j_\nu^k = -\frac{1}{2}\frac{1}{|g|} T_k^{\mu\nu} \partial_\nu |g|, \quad k = e, i \tag{3.10}$$

where $T_k^{\mu\nu} \in \mathbb{R}^{4\times4}$ is the *Energy Stress Tensor* of the electrons or ions with species index $k = e, i$, respectively, $F^{\mu\nu}$ the field strength tensor (cf. section 3.2), $\partial_\nu = \partial/\partial x^\nu$ is the co-variant 4-divergence and $g^{\mu\nu}$ is the metric tensor, where $\mu, \nu = 0, 1, 2, 3$. The 0-component of Eqs. 3.10 expresses the power balance, whereas components 1-3 are identified with the momentum balance. The left hand side of Eqs. 3.10 corresponds to the Lorentz invariant formalism of fluid theory, whilst the right hand side contains the gyroscopic forces resulting from $(\nabla \times \vec{u} \neq 0)$. If the velocity u only slowly changes with respect to the transverse coordinate y on the scale of a laser wavelength λ: $\lambda|\partial_y u| \ll |u|$, the metric tensor can be series expanded: $g_{\mu\nu} \approx \eta_{\mu\nu} + h_{\mu\nu}$, with $|h_{\mu\nu}| = \varepsilon \ll 1$ and the MINKOWSKI TENSOR $\eta_{\mu\nu} = \mathrm{diag}(1, -1, -1, -1)$. A series expansion of Eq. 3.10, using $\sqrt{|g|} \approx 1 + 1/2\mathrm{tr}(\eta^{\alpha\beta} h_{\nu\beta})$, yields:

$$\partial_\nu T_k^{\mu\nu} - F^{\mu\nu} j_\nu^k = -\frac{1}{2} T_k^{\mu\nu} \partial_\nu \mathrm{tr}(\eta^{\alpha\beta} h_{\nu\beta}) + \mathcal{O}(\varepsilon^2) \tag{3.11}$$

In the further course of this work this model is identified as *co-variant picture* or *co-variant model*. A derivation with respect to $\mathcal{O}(\varepsilon)$, results in the Lorentz invariant description of the plasma:

$$\partial_\nu T_k^{\mu\nu} - F^{\mu\nu} j_\nu^k = 0 \tag{3.12}$$

Assuming isotropic pressure p_k of the ions and electrons, the energy stress tensor $T_k^{\alpha\beta}$ takes the form:

$$T_k^{\alpha\beta} = \left(\rho_k + c^{-2} p_k\right) u_k^\alpha u_k^\beta - \eta^{\alpha\beta} p_k, \quad k = e, i, \tag{3.13}$$

where the mass density ρ_k is:

$$\rho_k = n_{0,k}\left(m_k + c^{-2}e_{0,k}\right) \tag{3.14}$$

Here, $e_{0,k}$ denotes the specific internal energy of a particle of fluid species k. In the relativistic picture, all kinds of energy contribute to mass, e.g. internal energy $\varpi_{th,k} = n_{0,k}e_{0,k}$, as well as power transferred from electric fields to the fluid $\varpi_{el,k} = \vec{j}_k \cdot \vec{E}$. The conservation of the particle number n_k does not immediately follow from the mass balance, as it does in the non-relativistic case. It is thus proposed it in addition:

$$\partial_\alpha\left(n_k u_k^\alpha\right) = 0 \tag{3.15}$$

Equation 3.14 considerably reduces in case the particles rest energy is much larger than the thermal energy: $m_{0,k}c^2 \gg e_{0,k}$. For an ideal gas the specific thermal energy of a particle is: $e_{0,k} = f/2k_B T_k$. For an electron temperature lower than $T_e \ll 2m_e c^2/(f k_B) \approx 4 \cdot 10^9\,\mathrm{K}$, or equivalently $e_{0,e} \ll 0.5\,\mathrm{MeV}$, the contribution of the thermal energy to the mass is negligible. For typical RPA plasmas $p_k/(n_{0,k}m_k c^2) \ll 1$ holds and terms of this type are left away in Eq. 3.12 and 3.14. By that, the energy stress tensor acquires the much more manageable size:

$$m_k c^2 \gg e_k: \quad T_k^{\alpha\beta} \approx m_k n_k u_k^\alpha u_k^\beta - \eta^{\alpha\beta} p_k \tag{3.16}$$

Equations 3.16 are identified as RELATIVISTIC TWO FLUID PICTURE or LORENTZ INVARIANT DESCRIPTION. A power series expansion up to first order in $\mathcal{O}(u_k/c)$ results in the traditional, non-relativistic fluid equations for electrons and ions:

$$\begin{aligned} \partial_t n_e + \nabla\cdot(n_e\vec{u}_e) &= 0 \\ m_e n_e\left(\partial_t\vec{u}_e + (\vec{u}_e\cdot\nabla)\vec{u}_e\right) &= -\nabla p_e - e n_e\vec{E} - e n_e\vec{u}_e\times\vec{B} \end{aligned} \tag{3.17}$$

$$\begin{aligned} \partial_t n_i + \nabla\cdot(n_i\vec{u}_i) &= 0 \\ m_i n_i\left(\partial_t\vec{u}_i + (\vec{u}_i\cdot\nabla)\vec{u}_i\right) &= -\nabla p_i + Z e n_i\vec{E} + Z e n_i\vec{u}_i\times\vec{B}, \end{aligned} \tag{3.18}$$

where isotropic pressure p_k and the absence of shear stresses is assumed. An expression for the pressure p_k can be obtained by setting up a balance equation for the conservation of energy. For the plasma represented by Eqs. 3.17 and 3.18 the energy balance yields:

$$\begin{aligned} \partial_t E_k + \vec{u}_k \cdot \nabla E_k + \frac{1}{m_k n_k} \nabla \cdot (p_k \vec{u}_k) &= \frac{1}{m_k n_k} \vec{j}_k \cdot \vec{E} \\ E_k &= \frac{e_k}{m_k} + \frac{1}{2} \vec{u}_k^2, \end{aligned} \tag{3.19}$$

where $p_k = p_k(s_k, n_k, T_k)$ and $e_k = e_k(s_k, n_k, T_k)$ are in general function of the entropy s_k, particle density n_k and species temperature T_k. However, it is more convenient to propose an equation of state $p_k = p_k(\rho_k, T_k, s_k)$ to obtain a correlation between pressure, density and temperature. The isentropic equation of state $p_k = p_k(\rho)$, $s_k = const$ is:

$$p_k = p_{k,0} \left(\frac{\rho_k}{\rho_{k,0}} \right)^{\varkappa} \tag{3.20}$$

Here $p_{k,0} = p_{k,0}(n_{k,0}, T_{k,0})$ denotes the initial pressure of the ions ($k = i$) and electrons ($k = e$) and $\varkappa = (f+2)/f$ is the heat capacity ratio, with f being the degrees of freedom. For an ideal gas there are only translational degrees of freedom and f meets the number of dimensions n of the correlated space $\mathbb{R}^n$. Equations 3.17, 3.18 together with the Maxwell's Equations 3.2 and the definitions 3.3, as well as the equation of state 3.20 are the complete set of equations for a non-relativistic, collision free, two fluid plasma. For a quasi neutral plasma of finite dimension the ions and electrons thermal velocity is nearly equal: $u_{th,i} \approx u_{th,e}$. It immediately follows:

$$\frac{u_{th,e}^2}{u_{th,i}^2} \approx 1 = \frac{m_i T_e}{m_e T_i} \Rightarrow \frac{T_e}{T_i} \approx \frac{m_i}{m_e} \gg 1 \tag{3.21}$$

Given that $n_e \propto n_i$, Eq. 3.21 implies that $p_i \ll p_e$ and p_i is thus negligible. Rearranging MAXWELL'S EQUATIONS 3.2, an expression for the electric field is obtained:

$$\partial_{tt} \vec{E} - c^2 \Delta \vec{E} + c^2 \nabla \left(\nabla \cdot \vec{E} \right) + \mu_0 c^2 \partial_t \vec{j} = 0 \tag{3.22}$$

Applying the electron momentum balance from Eqs. 3.17 to the definition Eq. 3.3 and assuming $|\partial_t \vec{j}_i| \ll |\partial_t \vec{j}_e|$[3], one obtains:

$$\partial_t \vec{j} \approx \partial_t \vec{j}_e = -e \partial_t (n_e \vec{u}_e) = \frac{e}{m_e} \nabla p_e + e (\vec{u}_e \cdot \nabla) n_e \vec{u}_e + \frac{e^2 n_e}{m_e} \left(\vec{E} + \vec{u}_e \times \vec{B} \right) \tag{3.23}$$

[3] A proof of this assumption is given in appendix B.2.

Combining Eqs. 3.22 and 3.23 and applying the equation of state 3.20 results in:

$$\begin{aligned}\partial_{tt}\vec{E} - c^2\Delta\vec{E} + c^2\nabla\left(\nabla\cdot\vec{E}\right) + \omega_{pe}^2\left(\vec{E} + \vec{u}_e\times\vec{B}\right)\\ + \frac{e}{\epsilon_0}\left(\vec{u}_e\cdot\nabla\right)n_e\vec{u}_e + \frac{e}{\epsilon_0}a_{e,0}^2\left(\frac{n_e}{n_{e,0}}\right)^{\varkappa-1}\nabla n_e = 0\end{aligned} \tag{3.24}$$

Here the definition of the plasma frequency Eq. 2.5 and the electron isentropic speed of sound $a_{e,0} = \sqrt{\varkappa_e k_B T_{e,0}/m_e}$ are used. An expression for ∇n_e is derived from GAUSS' LAW:

$$\nabla n_e = -\frac{\epsilon_0}{e}\nabla\left(\nabla\cdot\vec{E}\right) + Zn_i \tag{3.25}$$

Introducing the new variables: $\vec{E} = E_0\vec{\varepsilon}$, $\vec{B} = E_0/c\vec{\beta}$, $n_e = n_{e,0}\tilde{n}_e$, $n_i = n_{e,0}\tilde{n}_i$, $\vec{u}_e = c\vec{v}_e$, $\vec{x} = l\vec{\xi}$, $t = T\tau$, the final equation reads:

$$\begin{aligned}\frac{1}{\omega_{pe}T^2}\partial_{\tau\tau}\vec{\varepsilon} - \frac{\delta^2}{l^2}\Delta_{\xi\xi}\vec{\varepsilon} + \frac{\delta^2}{l^2}(1-M_c^2)\nabla_\xi\nabla_\xi\vec{\varepsilon}\\ + \frac{\lambda_{a0}}{l}\tilde{n}_e^{\varkappa-2}\nabla_\xi\tilde{n}_i + \frac{\lambda_c}{l}\tilde{n}_e^{-1}\vec{v}_e\nabla_\xi\tilde{n}_e\vec{v}_e + \vec{\varepsilon} + \vec{v}_e\times\vec{\beta} = 0,\end{aligned} \tag{3.26}$$

with the definitions:

$$\omega_{pe}^2 = \frac{n_e e^2}{\epsilon_0 m_e},\quad \delta = \frac{c}{\omega_{pe}},\quad \lambda_{a0} = \frac{m_e a_0^2}{eE_0},\quad \lambda_c = \frac{m_e c^2}{eE_0},\quad M_c^2 = \frac{a_0^2}{c^2}\tilde{n}_e^{\varkappa-1} \tag{3.27}$$

Here, ω_{pe} is the plasma frequency, δ is the skin-depth, l, T are a characteristic length or time, respectively, M_c^2 is a sonic Mach number with respect to c, $\lambda_{a0} \approx 10^{-14}-10^{-12}$ m is the width of the sonic shock and $\lambda_c \approx 10^{-11}-10^{-9}$ m is the width of the EM shock. l, T can be either given by intrinsic scales (e.g. penetration depth and relaxation time), boundary conditions or external quantities, e.g. as a scale. Since $\lambda_{a0}, \lambda_c \ll l$ for any characteristic length l, one obtains:

$$\frac{1}{\omega_{pe}T^2}\partial_{\tau\tau}\vec{\varepsilon} - \frac{\delta^2}{l^2}\Delta_{\xi\xi}\vec{\varepsilon} + \frac{\delta^2}{l^2}(1-M_c^2)\nabla_\xi\nabla_\xi\vec{\varepsilon} + \vec{\varepsilon} + \vec{v}_e\times\vec{\beta} = 0 \tag{3.28}$$

Equation 3.28 is an important result: Given small or large scales l, T, one obtains from Eq. 3.28 the asymptotic limits of the RPA dynamics.

3.3.1 Asymptotic limit of short scales

The dynamics related to short intrinsic scales $l \propto \delta$ and $T \propto \omega_{pe}^{-1}$ is dominated by the electrodynamic interaction of the electrons and the laser wave. For this scale, Eq. 3.28 yields:

$$\partial_{\tau\tau}\vec{\varepsilon} - \Delta_{\xi\xi}\vec{\varepsilon} + (1 - M_c^2)\nabla_\xi \nabla_\xi \vec{\varepsilon} + \vec{\varepsilon} + \vec{v}_e \times \vec{\beta} = 0 \tag{3.29}$$

For ultra hot plasmas, $\kappa_e k_B T_e \approx m_e c^2$, holds and $M_c \to 1$. In this case the effect of space charge $\nabla_\xi \vec{\varepsilon}$ vanishes. This is in coincidence with the view of an infinite Debye-length. Assuming $\vec{v}_e \ll 1$, for the transverse field $\vec{\varepsilon}_\perp$ in one dimension, Eq. 3.29 reduces to the well known KLEIN-GORDON EQUATION:

$$\partial_{\tau\tau}\vec{\varepsilon}_\perp - \partial_{\xi\xi}\vec{\varepsilon}_\perp + \vec{\varepsilon}_\perp = 0 \tag{3.30}$$

3.3.2 Asymptotic limit of large scales

For effects related to large scales $l \gg \delta$, $T \gg \omega_{pe}^{-1}$,[4] Eq. 3.28 yields:

$$\vec{\varepsilon} + \vec{v}_e \times \vec{\beta} = 0 \tag{3.31}$$

According to Eq. 3.31, electrodynamic effects do not contribute to the dynamics on a large scale. Since the electron dynamics is negligible on large scales, a further simplification of the fluid picture is achieved by merging the two fluid model to a *one fluid formalism*. Using the definitions for the overall mass density ρ and the barycentric velocity $\vec{u}$

$$\begin{aligned} \rho &= \rho_i + \rho_e \\ \vec{u} &= \frac{\rho_i \vec{u}_i + \rho_e \vec{u}_e}{\rho_i + \rho_e}, \end{aligned} \tag{3.32}$$

and adding the first of Eqs. 3.17 and 3.18 yields:

$$\begin{aligned} \partial_t (m_e n_e + m_i n_i) + \nabla \cdot (m_e n_e \vec{u}_e + m_i n_i \vec{u}_i) = 0 \\ \Rightarrow \partial_t \rho + \nabla \cdot (\rho \vec{u}) = 0 \end{aligned} \tag{3.33}$$

[4] Or equivalently, $\delta \to 0 \Leftrightarrow \omega_{pe} \to \infty$.

Given that $n_e \approx Z n_i$ and $m_e \ll m_i$, the electron mass density is much smaller than the ion mass density: $\rho_e/\rho_i = \varepsilon \ll 1$. A series expansion of the mass density ρ and the barycentric velocity $\vec{u}$ in ascending powers of ε provides:

$$\begin{aligned} \rho &= \rho_i + \rho_e = \rho_i + \varepsilon\rho_i \\ \vec{u} &= \frac{\rho_i\vec{u}_i + \rho_e\vec{u}_e}{\rho_i + \rho_e} = \frac{\vec{u}_i + \varepsilon\vec{u}_e}{1+\varepsilon} \approx \vec{u}_i + (\vec{u}_e - \vec{u}_i)\,\varepsilon + \mathcal{O}(\varepsilon^2) \end{aligned} \tag{3.34}$$

During the RPA the electrons and ions are co-moving, $|\vec{u}_e - \vec{u}_i| \propto \varepsilon\vec{u}_i \ll \vec{u}$. Adding the second of Eqs. 3.17 to the second of Eqs. 3.18 one obtains:

$$\rho\left[\partial_t\vec{u} + (\vec{u}\cdot\nabla)\,\vec{u}\right] = -\nabla p_e + \rho_{el}\vec{E} + \vec{j}\times\vec{B} \tag{3.35}$$

An expression of the pressure gradient ∇p_e in terms of the new variables ρ and $\vec{u}$ is:

$$\nabla p_e = \frac{\partial p_e}{\partial \rho_e}\nabla\rho_e = a_0^2\left(\frac{\rho}{\rho_0}\right)^{\varkappa-1}\nabla\rho, \quad a_0^2 = \frac{Z\varkappa k_B T_{e,0}}{m_i} \tag{3.36}$$

Finally the Eqs.

$$\begin{aligned} \partial_t\rho + \nabla\cdot(\rho\vec{u}) &= 0 \\ \rho\left[\partial_t\vec{u} + (\vec{u}\cdot\nabla)\,\vec{u}\right] &= -a_0^2\left(\frac{\rho}{\rho_0}\right)^{\varkappa-1}\nabla\rho + \rho_{el}\vec{E} + \vec{j}\times\vec{B} \end{aligned} \tag{3.37}$$

together with the Maxwell's Equations 3.2 and the material laws 3.3 are the complete set of equations in the ONE FLUID PICTURE. It is important to note the composition of the equilibrium isentropic sound speed a_0: the electrons contribute temperature $T_{e,0}$ and number density (see the charge state Z in Eq. 3.36), whereas the mass of the medium is given by the ion mass m_i. The advantage of the one fluid model is a reduction of the number of unknowns and equations, balanced by a loss of information about the density and velocity distribution of the individual species. For $\rho = const$, $\rho_{el} = 0$ and $\partial_t\vec{D} = 0$[5] Eqs. 3.2, 3.3 and 3.37 reduce to the well known equations of classical magnetohydrodynamics (MHD). Providing large scales $l \gg \delta$ and $T \gg \omega_{pe}^{-1}$, Eq. 3.31 holds and Eqs. 3.37 reduce to the well known equations of *isentropic gas dynamics*:

[5] This reduction corresponds to the assumption of slowly varying fields $\omega \ll \omega_{pe}$.

$$\partial_t \rho + \nabla \cdot (\rho \vec{u}) = 0$$
$$\partial_t \vec{u} + (\vec{u} \cdot \nabla)\vec{u} + \frac{a_0^2}{\rho}\left(\frac{\rho}{\rho_0}\right)^{\varkappa - 1} \nabla \rho = 0 \tag{3.38}$$

For this case, the interaction with external forces (e.g. radiation pressure) is included due to boundary conditions, continuity conditions or contact discontinuities.

3.3.3 Asymptotic limit of ultra strong lasers: The Current Flag Model

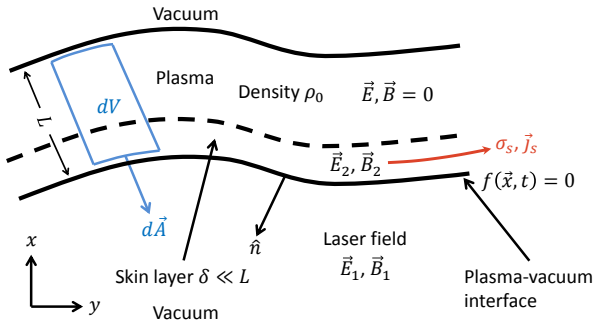

Figure 3.1.: Schematic of the CFM: The external field $\vec{E}_1, \vec{B}_1$ interacts with the plasma in a small skin-layer with dimension $\delta \ll L$. The plasma responds with an induced current density $\vec{j}_s$ and charge density σ_s and the inner of the plasma sheet is field free.

This section presents the derivation of the *current flag model* (CFM), which is used for the two dimensional investigation of the RPA. Given the radiation pressure of the laser $p_L = 2I/c$ and the hydrostatic pressure p, a strong laser is identified with $p_L > p$, whereas a weak laser satisfies $p_L < p$. Assuming small density variation

$$\rho \approx \rho_0 + \varepsilon \rho_0 + \mathcal{O}(\varepsilon^2), \quad \varepsilon \ll 1 \tag{3.39}$$

from Eq. 3.36 for a strong laser one obtains:

$$\frac{2I_0}{c} \gg a_0^2 \frac{\rho_0}{\varkappa}\left(\frac{\rho}{\rho_0}\right)^{\varkappa} \approx a_0^2 \frac{\rho_0}{\varkappa} + a_0^2 \rho_0 \varepsilon + \mathcal{O}(\varepsilon^2) \tag{3.40}$$

With the definition of the plasma rest energy density $\varpi_0 = \rho_0 c^2$, the Mach number $M_c = a_0/c$ and the laser energy density $\varpi_{EM} = \epsilon_0 E_0^2$, the final condition for a strong laser is:

$$\varepsilon M_c^2 \ll 1 \ll \frac{\varpi_{EM}}{\varpi_0} \tag{3.41}$$

Here, $E_0 = E_0(\vec{x}, t)$ denotes the slowly varying laser field amplitude. In case $a_0 \ll c$, it is appropriate to assume the plasma slab to be at constant density $\rho \approx \rho_0 + \mathcal{O}(\varepsilon)$. In accordance the target thickness also remains constant $L = const$. A schematic of the model is shown in fig. 3.1: The plasma is modeled as a slab of constant thickness and density, bounded by a vacuum-plasma interface.

The interface is a piecewise continuously differentiable and bounded surface function $f(\vec{x}, t) : \mathbb{R}^2 \times \mathbb{R}_0^+ \to \mathbb{R}$, to which Liouville's Theorem is applied.

Theorem 1 (Liouville's Theorem)**.** *[56] Given a bounded, holomorphic function $f : \mathbb{C} \to \mathbb{C}$, such that there exists a constant $c \in \mathbb{R}$ for which holds: $|f(z)| \leq c \ \forall z \in \mathbb{C}$. Then f is constant.*

Proof. See [56]. □

Given that $\mathbb{R} \subset \mathbb{C}$, theorem 1 holds for real functions in particular. Thus, Liouville's Theorem 1 states: $f(\vec{x}, t) = const$. and therefore:

$$\frac{df(x, y, t)}{dt} = 0 \tag{3.42}$$

Furthermore the trajectories $x = x(t), y = y(t) : \mathbb{R}_0^+ \to \mathbb{R}$ are analytic in order to preserve consistency with Liouville's Theorem 1. Then,

$$\frac{df(x, y, t)}{dt} = \frac{\partial f}{\partial t} + \frac{dx}{dt}\frac{\partial f}{\partial x} + \frac{dy}{dt}\frac{\partial f}{\partial y} = 0, \tag{3.43}$$

holds in particular. With the plasma velocities $d_t x = u$ and $d_t y = v$ and $\vec{u} = (u, v)^T$ Eq. 3.43 yields:

$$\frac{\partial f}{\partial t} + u\frac{\partial f}{\partial x} + v\frac{\partial f}{\partial y} = 0 \tag{3.44}$$

Equation 3.44 shows that $f(x, y, t)$ is a material surface of the plasma sheet. Without loss of generality, another representation of the plasma interface function

is: $f = x - h(y,t)$. The Galilei invariant (non-relativistic) kinematic boundary condition for the plasma-vacuum interface finally is:

$$\partial_t h + v\partial_y h - u = 0 \quad x = h(y,t) \tag{3.45}$$

Given that the skin-depth of the plasma is much smaller than the slab width $\delta \ll L$ and the plasma is collisionless $\nu_{ei}, \nu_{ee} \ll \nu_{pe}$, it is sufficient to model the plasma as a perfect electric conductor. Consistently, the charge and current density are located at an infinitesimal small layer on the surface $x = h(y,t)$ and the inner of the plasma slab remains neutral. The momentum balance, second of Eq. 3.37, in terms of integrals is:

$$\begin{aligned} \frac{d}{dt}\int_V \rho\vec{u}dV &= \int_V \rho_{el}\delta(x-h(y,t))\vec{E} + \vec{j}\delta(x-h(y,t)) \times \vec{B}dV \\ \Rightarrow \frac{d}{dt}\int_V \rho\vec{u}dV &= \int_S \left[\rho_{el}\vec{E} + \vec{j}\times\vec{B}\right]_{x=h(y,t)} dA \end{aligned} \tag{3.46}$$

Where $\delta(x)$ is the Dirac Delta Distribution. Introducing the surface currents $\vec{j}_s = \vec{j}(x = h(y,t), y, t)$ and surface charges $\sigma_s = \rho_{el}(x = h(y,t), y, t)$ as depicted in fig. 3.1, one obtains:

$$\frac{d}{dt}\int_V \rho\vec{u}dV = \int_S \sigma_s\vec{E} + \vec{j}_s \times \vec{B}dA \tag{3.47}$$

Given that the laser focal spot size[6] $w_0 > \lambda$ and $\lambda \gg L$, the transverse dimension of the laser plasma interaction is much larger than the longitudinal width:

$$L \ll \int \sqrt{1+\partial_y h^2}dy \tag{3.48}$$

Hence, the longitudinal variation of the velocity is small $\partial_x\vec{u} \approx \varepsilon\vec{u}/L$. Given $dV = dxdA$ it yields:

[6] For a Gaussian beam, that is the beam waist.

$$\begin{aligned}
\vec{u}(x,y,t) &\approx \vec{u}\Big|_{x=h(y,t)} + \frac{\partial \vec{u}}{\partial x}\Big|_{x=h(y,t)} (x-h(y,t)) + \ldots \\
\Rightarrow \int_h^{h+L} \vec{u}\,dx &\approx \left[\vec{u}\Big|_{x=h(y,t)}\, x + \frac{\partial \vec{u}}{\partial x}\Big|_{x=h(y,t)} (\frac{1}{2}x^2 - h(y,t)x) + \ldots\right]_h^{h+L} \\
&= \vec{u}(x=h,y,t)L + \frac{1}{2}\varepsilon\vec{u}(x=h,y,t)L + \mathcal{O}(\varepsilon^2)
\end{aligned} \tag{3.49}$$

With the above power series expansion, the localization of the integral 3.46 with a precision up to an order of $\mathcal{O}(\varepsilon)$, is:

$$\begin{aligned}
\mu\frac{d\vec{u}}{dt} - \sigma_s\vec{E} - \vec{j}_s \times \vec{B} = 0, \quad x = h(y,t) \\
\vec{E} = \vec{E}_1 + \vec{E}_2, \quad \vec{B} = \vec{B}_1 + \vec{B}_2,
\end{aligned} \tag{3.50}$$

where $\mu = \rho_0 L$ denotes the areal density of the plasma sheet/flag. For $|u|, |v| \ll c$, the electric and magnetic fields must satisfy the continuity conditions

$$\begin{aligned}
\hat{n} \times \left[\vec{E}\right] = 0, \quad \hat{n} \cdot \left[\vec{D}\right] = \sigma_s \\
\hat{n} \cdot \left[\vec{B}\right] = 0, \quad \hat{n} \times \left[\vec{B}\right] = \mu_0\vec{j}_s
\end{aligned} \tag{3.51}$$

across the surface $x = h(y,t)$. Here $\hat{n}$ is the normal vector of the interface (cf. fig. 3.1):

$$\hat{n} = \frac{\nabla f}{|\nabla f|} = \frac{1}{\sqrt{1+(\partial_y h)^2}} \begin{pmatrix} 1 \\ -\partial_y h \end{pmatrix} \tag{3.52}$$

For sufficiently small surface slopes $\partial_y h \ll 1$, the surface normal is approximated according to $\mathcal{O}((\partial_y h)^2)$:

$$\hat{n} \approx \begin{pmatrix} 1 \\ -\partial_y h \end{pmatrix} \tag{3.53}$$

The system is completed by the vacuum material laws $D_i = \epsilon_0 E_i$ and $B_i = \mu_0 H_i$ (see also section 3.2). Since the fields in the plasma center are supposed to vanish, conditions 3.51 split to:

$$\begin{aligned} \hat{n} \times \vec{E}_2 &= \hat{n} \times \vec{E}_1, \quad \hat{n} \cdot \vec{E}_2 = 0, \quad \epsilon_0 \hat{n} \cdot \vec{E}_1 = \sigma_s \\ \hat{n} \cdot \vec{B}_2 &= \hat{n} \cdot \vec{B}_1, \quad \hat{n} \times \vec{B}_2 = 0, \quad \mu_0^{-1} \hat{n} \times \vec{B}_1 = \vec{j}_s \end{aligned} \tag{3.54}$$

In the vacuum region (see fig. 3.1, region 1), the external laser field is given by $\vec{E}_1 = (0, E_{1y}, E_{1z})^T$ and $\vec{B}_1 = (0, B_{1y}, B_{1z})^T$. Solving Eqs. 3.54 together with 3.45 one obtains:

$$\begin{aligned} \vec{B}_2 &= (-\partial_y h B_{1y}, 0, 0)^T, \quad \vec{E}_2 = (\partial_y h E_{1y}, E_{1y}, E_{1z})^T \\ \sigma_s &= \epsilon_0 \partial_y h E_{1y}, \quad \vec{j}_s = \mu_0^{-1} (\partial_y h B_{1z}, B_{1z}, -B_{1y})^T \end{aligned} \tag{3.55}$$

Using $\vec{B}_1 = c^{-1} \hat{k} \times \vec{E}_1$, with the unit wave vector $\hat{k} = \vec{k}/|\vec{k}|$, the equations of motion with a precision up to $\mathcal{O}((\partial_y h)^2)$, are:

$$\begin{aligned} \mu \frac{du}{dt} &= \epsilon_0 (\partial_y h)^2 E_{1y}^2 + \epsilon_0 E_0^2 \\ \mu \frac{dv}{dt} &= \epsilon_0 \partial_y h E_0^2 \\ \mu \frac{dw}{dt} &= 0 \end{aligned} \tag{3.56}$$

Equations 3.45 and 3.56 are the final system of coupled equations of motion, referred to as *current flag model* (CFM, CF model), due to its similarity to a flag, moving in an air stream. Further reducing Eqs. 3.56 up to $\mathcal{O}(\partial_y h)$, one obtains:

$$\frac{d\vec{u}}{dt} = \frac{p_L}{\mu} \hat{n}, \tag{3.57}$$

where $p_L = 2I/c$ and $I = 1/2 \epsilon_0 c E_0^2$. Generally, the electrical field amplitude is a function of space and time $E_0 = E_0(y, t)$. Equation 3.57 permits another view of the model: The laser provides an external pressure p_L, which acts onto the surface, normal to the interface and by that pushes away the current carrying flag. Since $I = I(y, t)$, this also includes the deformation of the flag.

For the sake of completeness, the above model is extended to the next higher order $\mathcal{O}(u^2/c^2)$. In a co-moving reference frame as depicted in fig. 3.2, the boundary conditions 3.51 remain valid:

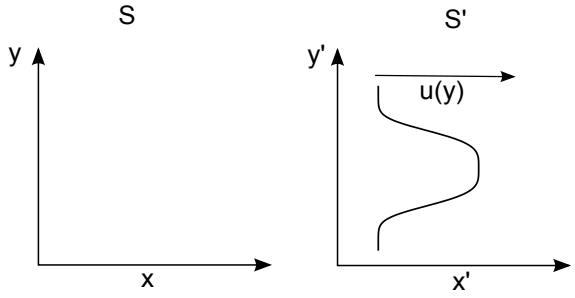

Figure 3.2.: Standard configuration of the laboratory frame S and the co-moving reference frame S'.

$$\begin{aligned} \hat{n} \times \left[\vec{E}'\right] = 0, \quad \hat{n} \cdot \left[\vec{D}'\right] = \sigma_s' \\ \hat{n} \cdot \left[\vec{B}'\right] = 0, \quad \hat{n} \times \left[\vec{B}'\right] = \mu_0 \vec{j}_s' \end{aligned} \tag{3.58}$$

Ultilizing the fields in the laboratory frame

$$\begin{aligned} \vec{E}' &\approx \vec{E} + \vec{v} \times \vec{B} + \mathcal{O}(u^2/c^2) \\ \vec{B}' &\approx \vec{B} - \vec{v}/c^2 \times \vec{E} + \mathcal{O}(u^2/c^2) \\ \sigma_s' &\approx \sigma_s + \mathcal{O}(u^2/c^2) \\ \vec{j}_s' &\approx \vec{j}_s - \sigma_s \vec{v} + \mathcal{O}(u^2/c^2) \end{aligned} \tag{3.59}$$

and solving Eqs. 3.58 results in:

$$\begin{aligned} \sigma_s &\approx \epsilon_0 \partial_y h E_{1y}(1 - u/c) \\ \vec{j}_s &\approx \epsilon_0 (1 - u/c) \begin{pmatrix} \partial_y h E_{1y}(c+u) \\ E_{1y}(c + u\partial_y h) \\ E_{1z}c + E_{1y} u \partial_y h \end{pmatrix} \end{aligned} \tag{3.60}$$

In zeroth order $\mathcal{O}((u/c)^0)$ these equations reduce to the non-relativistic Eqs. 3.55. The kinematic boundary condition 3.45 remains valid in the relativistic limit: using the 4-vector style $f = f(ct, x, y, z)$, $x^\alpha = (ct, x, y, z)$, $\partial_\alpha = (c^{-1}\partial_t, \partial_x, \partial_y, \partial_z)$ and $u^\alpha = (c, u_x, u_y, u_z)$, Eq. 3.45 may be written as:

$$\partial_\alpha f(x^\beta) u^\alpha = 0, \tag{3.61}$$

where the EINSTEIN NOTATION is used. Given that u^α is a co-variant vector, the 4-gradient $\partial_\alpha f$ is a contra-variant vector and thus the scalar product in Eq. 3.61 is a Lorentz scalar. From Eqs. 3.60 one obtains, that for $u \to c$, the surface current and charge vanishes and thus the Lorentz force onto the plasma vanishes. This effect is well known as relativistic Doppler effect. The reproduction of approved effects confirms the presented model.

4 The simulation software package VSim

This chapter introduces the simulation software VSim© [46], which was used for the present work. VSim© [46] is a commercial Particle in Cell (PIC) and electromagnetic (EM) simulation software package distributed by the Tech-X Corporation. The software is particularly optimized for plasma physics simulation purposes. Subsequently, an overview over the basic features of the software is given, as well as some basic properties of the Finite Difference Time Domain (FDTD) technique that is used for solving the Maxwell's equations. Thereby, the most important terms used in PIC simulations are explained. The main criteria for a stable simulation are presented, followed by a series of verification simulations to specify the simulation parameters, used across this work.

4.1 Features of VSim

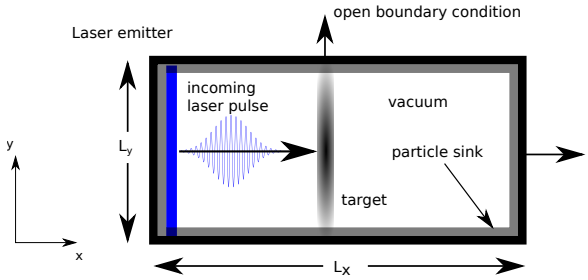

Figure 4.1.: Typical 2D full EM PIC simulation domain used for RPA simulation: A box with dimensions $L_x \times L_y$ is surrounded by particle sinks and open EM boundary conditions, whereas the laser is emitted from the left boundary.

The VSim© [46] software package splits into *VSim for Electromagnetics*, *VSim for Microwave Devices*, *VSim for Plasma Acceleration* and *VSim for Plasma Discharges*. Each package contains a certain list of features and solvers. For this work, the full VSim software package is available, thus the features used for this work are listed.

VSim covers a relativistic, full electromagnetic FDTD Particle in Cell solver for one to three dimensions. In one dimension VSim solves the relativistic equations of motion for each macro particle's position and velocity, $\left\{x^{\alpha j}, \gamma^{\alpha j} u_x^{\alpha j}, \gamma^{\alpha j} u_y^{\alpha j}, \gamma^{\alpha j} u_z^{\alpha j}\right\}$, where α denotes the species (e.g. electrons, ions, neutral gas etc.), α_j the j-th macro particle of a certain species and $\gamma^{\alpha j}$ the particles corresponding Lorentz factor.

In addition, the electric and magnetic fields $\left\{E_x, E_y, E_z, B_x, B_y, B_z\right\}$, as well as the field sources $\left\{\rho_{el}, j_x, j_y, j_z\right\}$ are calculated as a function of (x, t).

Accordingly, this is identified as 1D full EM PIC simulation. Similarly this scheme can be expanded to 2D or 3D simulation. The simulation domain is meshed with an equidistant cartesian or polar coordinate grid.

For this purpose VSim provides a flexible solver building system based on an XML-like script language. The user specifies the simulation domain, fields-, solvers and interpolation order, as well as the particle species and the corresponding initial- and boundary conditions. The basic schematic is shown in fig. 4.2. To enhance the computational performance, VSim offers the possibility of massive parallel computing up to several 10,000 cores, as well as GPU computing.

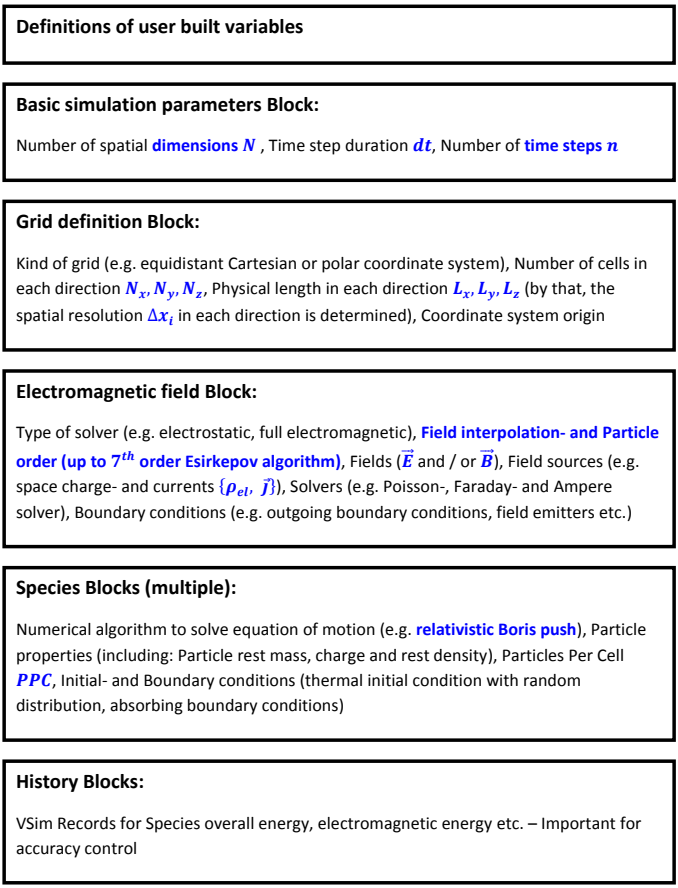

Figure 4.2.: Representation of a typical VSim©[46] simulation setup. All parameters and information are specified in certain blocks.

4.2 The Finite Difference Time Domain method

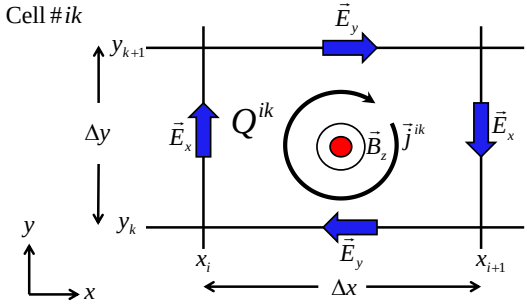

Figure 4.3.: Two dimensional scheme of the Yee lattice: The cell $\#ik$ contains a charge Q^{ik} and current density $\vec{j}^{ik}$ that are the sources of the electric and magnetic fields. For the TE mode, the electric field components (blue arrows) are evaluated on the cell edge centers, whereas the magnetic field component (Red dot & circle) is evaluated at the cell center.

The Finite Difference Time Domain (FDTD) method is a numerical algorithm to solve time dependent partial differential equations, also known as Yee's method named after its inventor Kane S. Yee. In particular, the FDTD method is used to solve Maxwell's equations. A detailed description of the FDTD method is beyond the scope of this thesis and this section is restricted to a presentation of the basic properties and requirements that are important for the simulations performed within this work. The interested reader is referred to the common literature, e.g. [57, 58]. Moreover, VSim is a commercial software, optimized for the inexperienced user and there is no direct access to the internal numerical pattern of the software. Figure 4.3 illustrates the basic concept of the Yee's method[57, 58]. Basically, time and space are subdivided into discrete steps of length Δt and Δx_i, respectively and the partial derivatives are re-written into finite difference equations. Subsequently, the finite difference equations are solved in an algebraic manner. The spatial discretization is also called a *grid* or a *mesh*, whereas the smallest volume of the grid is called a *cell*. Within all numerical solutions, the evaluation of the numerical error or precision is important. Especially for physics simulations, it has to be ensured that e.g. the behavior or motion of charged particles is not distorted by the numerical method used. Regarding the FDTD method, the most important numerical error is the so called *grid heating*: Grid heating is the artificial and unphysical energy gain of the particles in the simulation, caused by an inadequate

resolution ($\Delta t, \Delta x_i$) and an inaccurate field calculation. By that, energy conservation is violated within the simulation by numerical causes and thus, the calculated results may be falsified. Hence, the present chapter focuses on the prevention of numerical errors and the determination of appropriate conditions for the resolution and numerical algorithms used. Before progressing deeper into detail, the concept of *macro particles* is introduced. A typical physical system as it appears in plasma physics consists of an immense number of electrons and ions. To give an idea of these numbers, consider a small carbon target of dimensions $2\,\mu\text{m} \times 2\,\mu\text{m} \times 50\,\text{nm}$. Even this small target consists of $2.26 \cdot 10^{10}$ ions and $1.35 \cdot 10^{11}$ electrons. With state of the art computers, it is impossible to simulate such an amount of particles within a reasonable time. In a simulation, a large bunch of physical particles is represented by one artificial, numerical particle with the total mass and charge of the physical particles, called *macro particle*. Accompanied with the concept of macro particles is the number of (macro-) *Particles Per Cell* (PPC). This parameter has a severe impact on the precision of the numerical field calculation, since the macro particles are the charge- and current carriers in the simulation. An insufficient number of PPC causes an increase of the numerical field fluctuations, resulting in *numerical noise*. On the other hand, if the PPC is chosen too high, the computational performance is considerably reduced. The FDTD method is an explicit numerical solution algorithm and must satisfy the COURANT-FRIEDRICHS-LEWY CONDITION (CFL), that connects the spatial discretization Δx_i in each direction i with the time step duration Δt and the velocity component in each direction u_i:

$$\Delta t \sum_{i=1}^{N} \frac{u_i}{\Delta x_i} \leq C \tag{4.1}$$

Here $N \in \mathbb{N}$ is the number of physical dimensions and $\{C \in \mathbb{R} : 0 < C \leq 1\}$. The largest possible velocity is the speed of light in vacuum c and the CFL condition must be satisfied for this:

$$c\Delta t \sum_{i=1}^{N} \frac{1}{\Delta x_i} \leq C \tag{4.2}$$

This condition states, that an EM wave must not propagate a distance larger than one cell within one time step. An even more strict expression by requiring the CFL condition to be satisfied for the smallest appearing cell dimension $\Delta x_{min} = \min\left\{\Delta x_i^{k_i},\ i = 1...N,\ k_i = 1...M_i\right\}$, where M_i determines the number of cells in the i-th direction and $\Delta x_i^{k_i}$ the cell size of the k-th cell in i-th direction:

$$c\Delta t \leq C\Delta x_{min} \tag{4.3}$$

However, intrinsic spatial- and temporal scales appear in plasma physics, which yield additional restrictions to Δx_{min} and Δt. In collisionless plasmas, the most important are the Debye-length λ_{De} and the oscillation time which is determined by the electron plasma frequency $\tau \propto 1/\omega_{pe}$[1]. From that one obtains the secondary conditions $\Delta x_{min} \leq \lambda_{De}$ and $\Delta t \leq 1/\omega_{pe}$. Finally this gives the both constrains for the grid resolution and time discretization:

$$\Delta x_{min} \leq c_x \lambda_{De}, \quad \Delta t \leq c_t \min\left\{1/\omega_{pe}, \Delta x_{min}/c\right\} \tag{4.4}$$

Where the safety constants are: $\{c_x \in \mathbb{R} : 0 < c_x \leq 1\}$ and $\{c_t \in \mathbb{R} : 0 < c_t \leq 1\}$.

Because ω_{pe} and λ_{De} both depend on the electron density n_e and additional to that λ_{De} depends on the electron temperature T_e, these quantities may change over time. To avoid a violation of conditions 4.5, c_x and c_t are chosen small enough in advance. Given $\Delta x = c_x \lambda_{De}$ with $\{c_x \in \mathbb{R} : 0 < c_x \leq 1\}$ it holds: $\Delta x_{min}/c \leq 1/\omega_{pe}$. The final condition for the temporal- and spatial resolution in a PIC simulation for plasmas is:

$$\Delta x_{min} \leq c_x \lambda_{De}, \quad \Delta t \leq c_t \Delta x_{min}/c \tag{4.5}$$

Experience shows, that for electron densities typical in RPA plasmas the chose of $c_x \in [0.3, 0.5]$ and $c_t \in [0.8, 0.9]$ is sufficient. Except for the adiabatic expansion after the acceleration process, the electron temperature T_e increases while the acceleration and so does the Debye length $\lambda_{De} \propto \sqrt{T_e}$. Therefore, the initial spatial discretization Δx is usually sufficiently fine for the overall process. By using high order form factors[2] for the macro-particles (for details see [59]), as well as high order field interpolations grid heating can be drastically reduced and resolution issues can be further avoided. For this purpose VSim© [46] provides charge density calculations and field interpolations with the *Esirkepov algorithm* up to 7th order. By using high order interpolation algorithms, the conservation of energy can be achieved with a much higher precision compared to the low order (0th or 1st) case.

Even in high density regions, where conditions 4.5 may be violated, the high order Esirkepov algorithm suppresses grid heating and by that prevents un-physical particle behavior[3] and the destabilization of the simulation. According to the

[1] For details, see chapter 2.1.

[2] Hereafter also called *particle order*.

[3] E.g. energy gain out of the nonentity, or faster than speed of light particles.

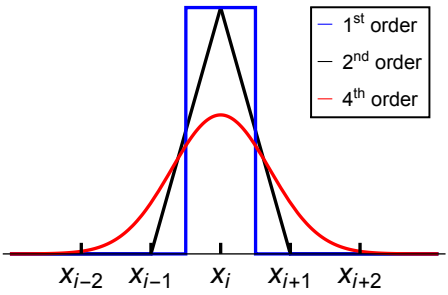

Figure 4.4.: Scheme of the particle order: The higher the particle order is chose, the more smooth the macro particle is represented in the simulation.

VSim© [46] manual, the particle order has always to be chosen greater or equal to the field interpolation order for stability reasons. Apparently, the order of a macro particle denotes its shape on the mesh, as exemplified in fig. 4.4.

The so called *relativistic Boris push algorithm*, invented by J. Boris, is used to solve the equation of motion for each particle. An abbreviated description of the major advantages of this method is given below. If the equation of motion of a charged particle under the influence of the Lorentz force is solved with an explicit numerical method, the particle trajectory is unstable, in a way that the particle artificially gains energy and by that increases its rotational radius, see fig. 4.5a. In principle, the Boris method explicitly solves the equation of motion, but in a three step system: First the particle performs a half rotation due to the magnetic field. Hereafter, the particle is pushed by the electric field in the second step and finally performs a second half rotation in the last step. By that, the trajectory is stabilized, as shown in fig. 4.5b.

4.3 Verification and specification of the simulation parameters

In order to determine sufficient simulation parameters, including PPC, spatial and temporal resolution (cf. condition 4.5), as well as the necessary interpolation order scheme, a series of verification simulations is performed. For the purpose of comparability, the simulation domain is the same in each case.

The simulation domain is a two dimensional box with the dimension $L_x \times L_y = 25\lambda_{De} \times 25\lambda_{De}$ discretized by an equidistant cartesian grid of $N_x \times N_y$ cells, surrounded by periodic boundary conditions for the particles and EM waves. The box is filled with a quasi neutral plasma consisting of fully charged titanium ions ($Z = 22$) with a density of $n_i = 10^{16}\,\mathrm{cm}^{-3}$ and the corresponding electrons with

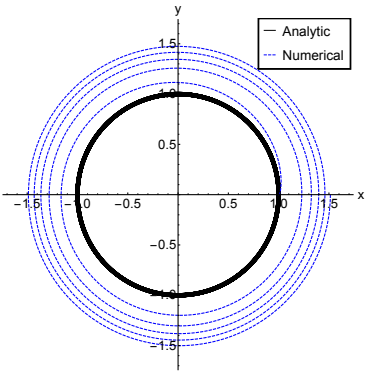

(a) Comparison of the analytical (black) and explicit Euler scheme (dashed blue): The particle artificially gains energy and thus the trajectory is unstable.

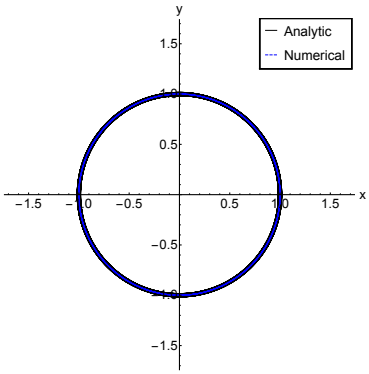

(b) Comparison of the analytical (black) and Boris method (dashed blue): By the use of the Boris push method, unstable trajectories are avoided.

Figure 4.5.: Comparison of a usual explicit numerical solution (left) of the equation of motion with the Boris method (right).

density $n_e = Zn_i$. Initially, the plasma is in thermal equilibrium with an electron initial temperature equivalent to $W_{th,e,0} = 10\,\mathrm{keV}$. With these specifications, the simulation represents an infinite plasma in thermal equilibrium.

This is the most simple setup possible, guaranteeing that there are no numerical errors or fluctuations by poor boundary conditions. In the absence of external energy sources, physically the overall energy $W_{tot} = W_{i,th} + W_{e,th} + W_{em} = const$ is conserved in such a system.

Two different branches of simulations are performed: The first set of simulations is performed with a spatial resolution of $\Delta x = \Delta y = 0.5\lambda_{De}$ (according to the condition 4.5) and the corresponding time step $\Delta t = 0.4\Delta x/c$ with different particle order schemes and field interpolation orders. This set of simulations is identified as „high resolution simulation“ (HR). As a rule of thump, 20 PPC is a well-built choice. Following this rule, the HR simulations are performed with $PPC = 30$.

The second set of simulations, identified as „low resolution simulation“ (LR) is performed with a spatial resolution of $\Delta x = 2\lambda_{De}$, violating condition 4.5.

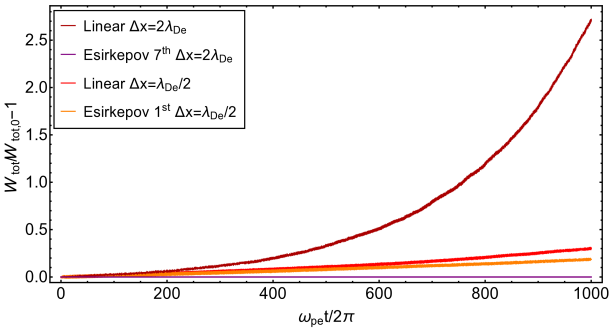

Figure 4.6.: Relative change of the particles thermal energy $W_{th}/W_{th,0}-1$ as a function of time for different resolutions and particle orders: Even for poor grid resolution, high order schemes efficiently suppress grid heating, while low order schemes show grid heating also for adequate grid resolution. From VSim simulation.

For the purpose of clean conditions[4], the time step duration Δt, the overall number of macro particles N_Σ and the size of the simulation domain $L_x \times L_y$, as well as the initial thermal energy $W_{i,th,0}, W_{e,th,0}$ are fixed. One obtains $\Delta t = 0.1\Delta x/c$ and $PPC = 120$ for the low resolution simulations. For a better overview, table 4.1 summarizes all parameters:

Table 4.1.: Simulation parameters used for verification.

Type	$\Delta x, \Delta y$	Δt	PPC	Algorithms
High Res.	$0.5\lambda_{De}$	$0.4\Delta x/c$	30	Lin., Esirk. $1^{st}, 3^{rd}, 5^{th}, 7^{th}$
Low Res.	$2\lambda_{De}$	$0.1\Delta x/c$	120	Lin., Esirk. 7^{th}

To analyze the effect of the grid resolution and the numerical algorithm used, we examine the validity of energy conservation over a simulation time of 1000 plasma oscillations, $T_{sim} = 1000 \cdot 2\pi/\omega_{pe}$.

Figure 4.6 shows the thermal energy fluctuation $W_{th}/W_{th,0} - 1$ for the simulations with poor grid resolution $\Delta x = 2\lambda_{De}$, as well as for the case of the lowest

[4] Clean conditions in this sense means to keep as many parameters constant, as possible.

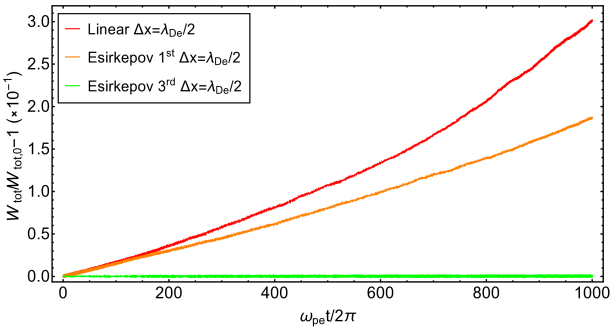

Figure 4.7.: Relative change of the particles thermal energy $W_{th}/W_{th,0}-1$ as a function of time for different particle orders with adequate resolution: Low order schemes show grid heating of 20%-30%, while the 3^{rd} order Esirkepov scheme (green) conserves energy with an error more than one order of magnitude lower.

particle order with an appropriate resolution $\Delta x = 0.5\lambda_{De}$. In case condition 4.5 is violated and low order macro particles are used, the thermal energy of the particles more than doubles due to the grid heating. From fig. 4.6 one obtains that the use of an adequate resolution reduces the numerical heating by more than an order of magnitude. A simulation with poor resolution and 7^{th} order Esirkepov algorithm shows the efficiency of high order algorithms: Grid heating is more efficiently suppressed by using high order algorithms compared to low order algorithms with a better resolution (compare purple and red, orange lines in fig. 4.6).

Figure 4.7 shows a comparison of HR simulations with different algorithm schemes: In case of linear- and first order Esirkepov algorithm the numerical heating increases the particles thermal energy by 20%-30% even for $\Delta x = 0.5\lambda_{De}$, whereas the third order Esirkepov algorithm reduces the grid heating by more than one order of magnitude with the same spatial resolution.

As in detail presented in chapter 2.1, the physical perception of a quasi neutral plasma assumes that the electrostatic potential decays within a Debye-sphere. Mathematically this is modeled such that the electrostatic potential decreases down to $1/e \approx 0.37$ of its original value within one Debye length. However, the remaining potential can cause fluctuations which heat up the particles in a PIC simulation. Thus, condition 4.5 only gives a rough estimate rather than an exact expression.

As a result, the choice of $c_x \leq 0.5$ and an interpolation better than or equal to third order Esirkepov is essential. To exploit all features provided by VSim© [46], the HR simulations are repeated with the highest interpolation orders Esirkepov

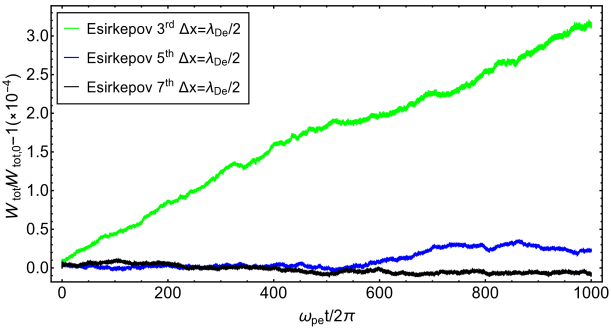

Figure 4.8.: Relative change of the particles thermal energy $W_{th}/W_{th,0}-1$ as a function of time the three highest particle orders with adequate grid resolution: The 3^{rd} order Esirkepov scheme (green) conserves energy up to an error in the range of 10^{-4}, while the error is more than one order of magnitude lower for the higher order schemes, $5^{th}, 7^{th}$ Esirkepov. This demonstrates the advantage of using high order interpolation schemes.

5^{th} and 7^{th}. The results are shown in fig. 4.8: For the Esirkepov 5^{th} and 7^{th} order algorithms and $\Delta x = 0.5\lambda_{De}$, energy conservation is realized up to a relative error better than $\Delta W_{th}/W_{th,0} \leq 10^{-4}$, which is an adequate precision. Below, the correlation of numerical field fluctuations, grid resolution and grid heating is investigated in more detail. Assuming a non-relativistic two fluid model as presented in chapter 3.3 in thermal equilibrium, the present system can be described by the following system of equations:

$$\begin{aligned} n_e e \nabla\phi &= k_B T_{e,0} \nabla n_e \\ \Delta\phi &= -\frac{e}{\epsilon_0}(Z n_i - n_e), \end{aligned} \tag{4.6}$$

where the ions' contribution to the thermal energy is assumed to be negligibly small. As there is no barycentric velocity $u_e = 0$, there are no currents and thus no magnetic fields, such that this system reduces to an electrostatic problem. As long as $u_e = 0$ holds and the thermal velocity $v_{e,th} \ll c$ holds, this system is described in a non-relativistic fashion. Given a quasi neutral plasma $n_e = Z n_i + \delta n_e$ and expanding the equations for small perturbations $\phi \to \delta\phi$ yields:

$$\begin{aligned} \delta\phi &= \frac{k_B T_{e,0}}{e} \ln\left(1 + \frac{\delta n_e}{n_{e,0}}\right) \\ \Delta\delta\phi &= \frac{e}{\epsilon_0}\delta n_e, \end{aligned} \tag{4.7}$$

where $n_{e,0} = Z n_i$ is used.

Given the equation of state for the electrons $p_e = n_e k_B T_e$, the electron pressure remains constant over the entire simulation $p_e = n_{e,0} T_{e,0}$. Permitting small perturbations for the temperature $T_e = T_{e,0} + \delta T_e$, Eq. 4.7 is approximately:

$$\frac{\delta n_e}{n_{e,0}} = -\frac{\delta T_e}{T_{e,0}} \tag{4.8}$$

Equation 4.7 together with Eq. 4.8 gives:

$$\begin{aligned} \delta\phi &= \frac{k_B T_{e,0}}{e} \ln\left(1 - \frac{\delta T_e}{T_{e,0}}\right) \\ \leftrightarrow \quad \frac{\delta T_e}{T_{e,0}} &= 1 - \exp\left(\frac{e\delta\phi}{k_B T_{e,0}}\right) \end{aligned} \tag{4.9}$$

Result 4.9 is very important: a small fluctuation in the electric potential is connected with an exponential growth of the temperature perturbation. Thus, to prevent unintended particle heating in the PIC simulation, one has to strongly suppress field fluctuations by the use of high interpolation order fields and high order particles. In case the Debye length is not resolved, the macro-particles have to heat up and by that increase the Debye length until condition 4.5 is met again. From $\Delta x = c_x \lambda_{De}$, together with $T_e = T_{e,0} + \delta T_e$ and $W_{th} = f/2 k_B T_e$ one derives the expression:

$$W_{th} = \frac{\Delta x^2}{c_x^2 \lambda_{De,0}^2} W_{th,0} \tag{4.10}$$

Here f denotes the degrees of freedom. Since $\Delta x > \lambda_{De,0}$ and $c_x < 1$, $W_{th} > W_{th,0}$, holds. The choice of c_x to sufficiently inhibit the grid heating depends on two major parameters: First, the number of macro particles per cell PPC plays an important role. As described in chapter 2.1, the number of particles in a Debye sphere has to be sufficiently large to cancel out charge fluctuations, which

according to Eq. 4.9 have a severe impact on the grid heating. Thus, the higher the number PPC is, the larger c_x may be chosen. Moreover, the particle- and interpolation order strongly influence the choice of c_x: As shown in fig. 4.7 and 4.8 in particular, higher order particles confine grid heating very efficiently, such that c_x may be chosen larger for high order particles. In general, for low order particles and fields, one may have to choose a very small c_x to avoid grid heating, as can be seen from fig. 4.6.

4.3.1 Specification of the simulation parameters

The sufficient simulation parameters are finally specified: Concerning the spatial and temporal resolution, the choice of $\Delta x_i \in \left[0.3\lambda_{De,0}, 0.5\lambda_{De,0}\right]$ and $\Delta t \in [0.4\Delta x_{min}/c, 0.9\Delta x_{min}/c]$ is sufficient. For the particle order and field interpolation, 5^{th} and 7^{th} order Esirkepov algorithm are used in all RPA simulations. For the number of macro particles per cell the choice of $PPC = 20 - 100$ is sufficient. The actual choice of parameters severely depends on the particular simulation, especially on the number of spatial dimensions and the physical effects which are investigated. Obviously, there may be cases where the chosen parameters are better than required, but the above parameters assure sufficiently small errors in any case.

5 Entropy production and laser polarization

A considerable reduction of the entropy production by using a CP laser rather than a LP laser was already discovered in previous work[53]. However, the underlying mechanism has not been understood, yet. Therefore, the relation between the plasma entropy and laser polarization is examined in this section. For a non-collisional $\nu_{ee}, \nu_{ei} \ll \nu_{pe}$, ideal plasma with isentropic pressure p_k the relativistic energy stress tensor is[54, 55] (cf. chapter 3.3)

$$T_k^{\alpha\beta} = \left(\rho_k + c^{-2} p_k\right) u_k^\alpha u_k^\beta - \eta^{\alpha\beta} p_k, \quad k = e, i \tag{5.1}$$

where $k = e, i$ denotes the species and

$$\rho_k = n_{0,k}\left(m_k + c^{-2} e_{0,k}\right), \quad \gamma_k = \frac{1}{\sqrt{1 - \vec{u}_k^2/c^2}}, \tag{5.2}$$

hold in particular for a plasma with no dissipation. It is furthermore assumed, that the plasma is free of reactions or that the reactions are in equilibrium. The assumption of a non-collisional plasma is accompanied with vanishing heat transfer, Ohm's conductivity and mass diffusion. Multiplying Eq. 3.12 by $u_\mu^k = \eta_{\mu\nu} u_k^\nu$ yields:

$$\partial_\nu T_k^{\mu\nu} u_\mu^k = F^{\mu\nu} j_\nu^k u_\mu^k \tag{5.3}$$

The thermodynamic relation[52, 60] $n_k m_k c^2 + n_k e_k = T_k s_k - p_k$ relates the fluid energy with the entropy s_k of each species. Applying the relativistic GIBBS-DUHEM-EQUATION[61] $s_k \partial_\mu T_k = \partial_\mu p_k$, one obtains from Eq. 5.3 the transport equation for the entropy s_k:

$$\partial_\mu\left(s_k u_k^\mu\right) = T_k^{-1} F^{\mu\nu} j_\nu^k u_\mu^k, \quad k = e, i, \tag{5.4}$$

where the left hand side of Eq. 5.4 denotes the transport of the entropy, whereas the right hand side contains the sources of entropy production. Given the field strength tensor in Eq. 3.6 and $j_\mu^k = \gamma_k(\rho_{k,el}, -\vec{j}_k)$, one obtains from Eq. 5.4:

$$T_k \partial_\mu \left(s_k u_k^\mu\right) = 2 Z_k e n_k \gamma_k^2 \left(\vec{E} \cdot \vec{u}_k\right), \quad Z_k = \begin{cases} -1 \text{ for electrons} \\ Z \text{ for ions} \end{cases} \tag{5.5}$$

In case of a quasi neutral plasma $Z n_i \approx n_e$ and assuming that the electrons and ions are co-moving in longitudinal direction $u_{e,\parallel} \approx u_{i,\parallel}$, as well as $\gamma_e \approx \gamma_i$, the total entropy is:

$$\sum_{k=i,e} T_k \partial_\mu \left(s_k u_k^\mu\right) \approx 2 e n_e \gamma_e^2 \left(\vec{u}_{i,\perp} \cdot \vec{E}_\perp - \vec{u}_{e,\perp} \cdot \vec{E}_\perp\right) \tag{5.6}$$

The ion's contribution to the azimuthal current is negligible compared to the one of the electrons, $|\vec{u}_{i,\perp}| \ll |\vec{u}_{e,\perp}|$ [1] and thus the total entropy is:

$$\sum_{k=i,e} T_k \partial_\mu \left(s_k u_k^\mu\right) \approx -2 e n_e \gamma_e^2 \vec{u}_{e,\perp} \cdot \vec{E}_\perp \tag{5.7}$$

Given that $T_i \ll T_e$, the entropy is:

$$\sum_{k=e,i} T_k \partial_\mu \left(s_k u_k^\mu\right) \approx T_e \partial_\mu \left(s_e u_e^\mu\right). \tag{5.8}$$

The laser model is: $\vec{E} = E_0 \left(\cos(kx - \omega t)\vec{e}_y + \cos(kx - \omega t + \varphi)\vec{e}_z\right)$, with E_0 being the field amplitude, only slowly varying in time: $|\partial_t E_0| \ll \omega |E_0|$. A CP laser is obtained for $\varphi = \pm\pi/2$, whereas $\varphi = 0$ is identified with a LP laser. From the electron momentum balance approximately follows:

$$\partial_t \vec{u}_{e,\perp} \approx -\frac{e}{m_e} \vec{E}_\perp \;\rightarrow\; \vec{u}_{e,\perp} \approx -\frac{e}{m_e} \int \vec{E}_\perp dt = -\frac{e}{m_e \omega^2} \partial_t \vec{E}_\perp \tag{5.9}$$

Combining Eqs. 5.7 and 5.9 the entropy production finally is:

$$\partial_\mu \left(s_e u_e^\mu\right) \approx \frac{2 e^2 n_e \gamma_e^2 E_0^2}{m_e \omega T_e} \cos(\varphi) \sin(2(kx - \omega t) + \varphi), \tag{5.10}$$

For a linearly polarized laser $\varphi = 0$ and the term on the right hand side of Eq. 5.10 is a source of entropy production, whereas for a circularly polarized laser $\varphi = \pm\pi/2$ the right hand side of Eq. 5.10 vanishes. Therefore it is advantageous to use a CP laser for the RPA in order to avoid entropy production. Here, the assumption

[1] See appendix B.2 for details.

a laser amplitude E_0 slowly varying in time is equivalent to the assumption of an adiabatic compression. In reality, the variation of the amplitude results in a small contribution to entropy production[2]. The entropy production is a result of the shock wave, generated by the laser plasma interaction; In case of linear polarization, the laser acts like an oscillating piston, producing two shock waves within one oscillation. On the other hand, a CP laser acts like an ascending piston: the slower the amplitude grows, the closer the piston motion gets to the adiabatic limit without entropy production.

Figure 5.1 shows the ion distribution obtained from 2D full EM simulations for a linearly and circularly polarized laser in comparison. As predicted by Eq. 5.10, the entropy production is much larger in case of a linearly polarized laser and the resulting heating dilutes the emerging plasma.

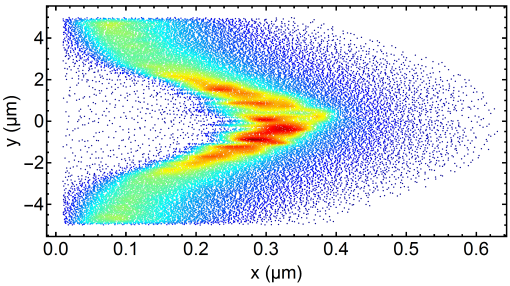

(a) Linear polarization.

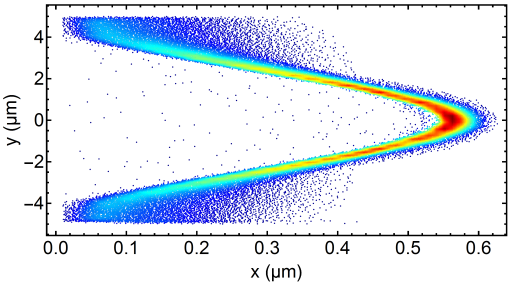

(b) Circular polarization.

Figure 5.1.: Comparison of the ion distribution for RPA driven by a LP and CP laser. The color illustrates the particle density.

[2] For details see appendix B.8.

6 Radiation pressure acceleration in one dimension

This chapter presents the one dimensional investigation of the RPA process. It is intuitive to treat the one dimensional case foremost, since it provides a number of useful simplifications: Due to the dependence on only one spatial coordinate, all effects concerning the transverse expansion of the plasma are dispensed. Furthermore, the application of the Lorentz transformation proves to be much simpler. Besides, typical composite instabilities such as the Rayleigh Taylor Instability*[62] do not appear in one dimension. According to the results of sections 3.3.1 and 3.3.2, the RPA is investigated in the asymptotic limits of short scales* $T \propto \omega_{pe}^{-1}, l \propto \delta$ *and large scales* $T \gg \omega_{pe}^{-1}, l \gg \delta$*, separately (cf. Eq. 3.28).*

6.1 RPA energy scaling and motivation

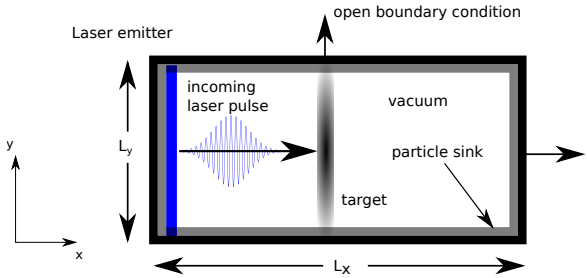

Figure 6.1.: Schematic of the standard simulation setup: The simulation domain (white) is a box of size $L_x \times L_y$ (in the 1D case, only the x-direction is treated) filled with vacuum and surrounded by absorbing boundary conditions for the particles (thick grey lines), as well as open boundaries (thick black lines) for the EM waves. The laser (blue curve) enters the domain from the left via a field emitting boundary condition (blue) and propagates to the right.

Initially the energy scaling of the plasma emerging during the RPA is examined. For this purpose a set of 1D full EM PIC simulations are performed, with the pa-

rameter summarized in tab. 6.1. The simulation setup is shown in fig. 6.1. If not stated otherwise, this is the standard simulation setup for all further investigation.

The formal solution of the flying mirror model Eq. 3.1[63, 64] (see also chapter 3.1), neglecting retardation, is:

$$\int_0^\beta \frac{1+\xi}{1-\xi}\frac{\xi}{\sqrt{1-\xi^2}}d\xi = \int_0^t \frac{2I(\tau)}{\rho c L}d\tau \tag{6.1}$$

A series expansion with respect to β yields:

$$W_{kin} = p^2c^2 \approx \left(\frac{2a\tau_L}{\rho_0 L}\right)^2 I_0^2 \propto \left(\frac{I_0}{\rho_0 L}\right)^2 \tag{6.2}$$

Thus, the flying mirror model predicts a light sail acceleration for all cases shown in table 6.1, scaling as shown in Eq. 6.2. For convenience, the laser has a Gaussian temporal profile with a pulse duration of $\tau_L = 100\,\mathrm{fs}$ in all cases.

Figure 6.2 shows a comparison of Eq. 6.2, $E_{kin} \propto \chi^2$[40] and the results obtained from the simulations. For simulations #1, #2 and #3, good agreement is achieved. However, fig. 6.2 reveals that simulations #4, #5 and #6 deviate from the analytical prediction of Eq. 6.2. Examples #4, #5 and #6 indicate, that for too thick or too thin targets, the validity of the light sail model fails. This motivates the derivation of conditions for a permissible upper and lower target thickness limit.

Table 6.1.: Simulation parameters used. The laser has a wavelength of $\lambda = 1\,\mu\mathrm{m}$ and a pulse duration of $\tau_L = 100\,\mathrm{fs}$.

No.	Ion	L(nm)	ρ(kg/m^3)	I_0(W/cm^2)	n_e	δ(nm)	A_0
1.	Au^{+15}	25	19320	33×10^{20}	$798n_c$	5.67	0.152
2.	Ti^{+22}	25	4500	10×10^{20}	$1106n_c$	4.79	0.198
3.	C^{+6}	50	2250	5×10^{20}	$603n_c$	6.48	0.099
4.	H^{+1}	112.5	1000	2.5×10^{20}	$536n_c$	6.87	0.049
5.	H^{+1}	300	1000	2.5×10^{20}	$536n_c$	6.87	0.019
6.	H^{+1}	14	1000	20×10^{20}	$536n_c$	6.87	3.175

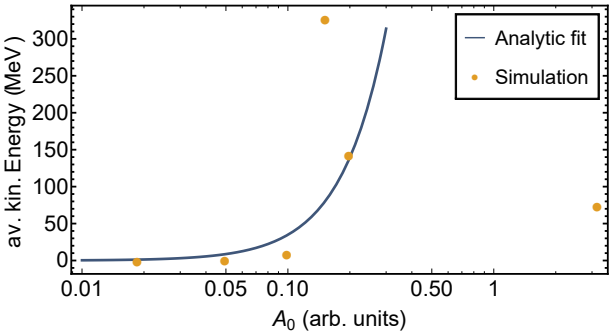

Figure 6.2.: Comparison of the average kinetic energy of the plasma as a function of the acceleration parameter $A_0^2 = 2I_0\tau_L/(\rho L_0 c^2)$ from the simulation (blue dots) and for comparison an analytic fit $W_{kin} \propto A_0^2$, according to Eq. 6.2.

6.2 RPA in the limit of short scales

In the following sections the interaction of the electrons with the electromagnetic wave is examined. Electromagnetic effects are related to the short intrinsic length and time scales, $l \propto \delta$ and $T \propto \omega_{pe}^{-1}$, respectively. Before proceeding with a detailed analysis, the next section introduces the dual layer concept of the RPA. The results presented in this section have been published by the author in [65] and [66].

6.2.1 Electron-ion dual layer

Since the laser plasma interaction occurs within a spatial dimension of a few nanometers, fig. 6.3 shows an enlarged view of the electron and ion distribution as well as the longitudinal electric field E_x. Figure 6.3 reveals a displacement of the ions and electrons that evolves a longitudinal polarization field and indicates the following mechanism for the RPA: The radiation pressure of the laser compresses the electrons, whereas the much more inert ions are unaffected. This configuration is identified with *Dual Layer* or *Dual Layer structure*. Subsequently, the polarization field exerts drag forces on the ions.

An adequate approximation of the dual layer width is derived, assuming step-like density profiles for electrons and ions.

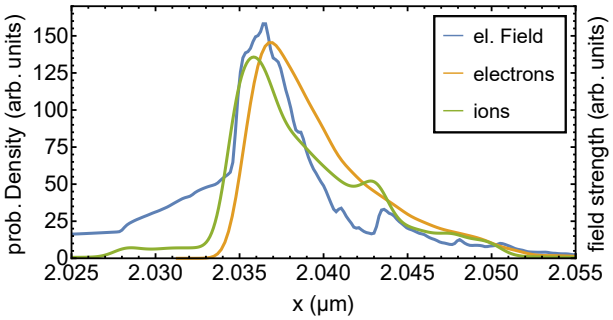

Figure 6.3.: Scaled up view of the electron (red), ion (green) probability density and the longitudinal electric field amplitude E_x (blue). Clearly visible is the shift between ions and electrons. Depicted from simulation #2, see table 6.1.

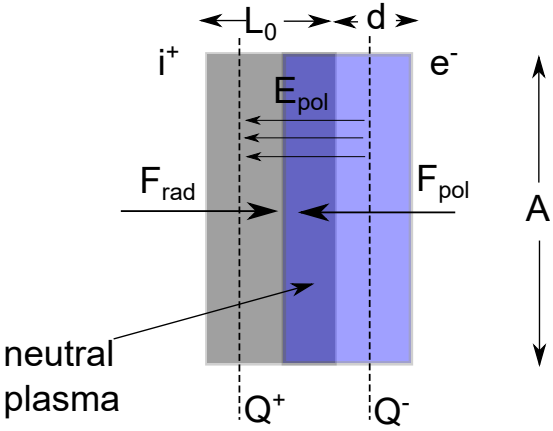

Figure 6.4.: Capacitor model of RPA: The laser compresses the electron gas (red). The resulting polarization field drags the ions (blue) (cf. [66]).

As depicted in fig. 6.4, a capacitor-like shape forms. For the charge $Q = en_e Ad$ in this layer, the electric field strength is

$$E_{pol} = \frac{Q}{\epsilon_0 A} = \frac{en_e d}{\epsilon_0}. \tag{6.3}$$

The displacement reaches its equilibrium when the force due to the laser radiation pressure $F_{rad} = 2I_0/cA$ and the counter-acting force due to the polarization field $F_{pol} = QE_{pol}$ are equal:

$$\frac{2I_0 A}{c} = \frac{e^2 n_e^2 d^2 A}{\epsilon_0} \tag{6.4}$$

Solving this equation for the separation layer thickness d, one obtains:

$$d = \sqrt{\frac{2I_0\epsilon_0}{e^2 n_e^2 c}} \tag{6.5}$$

For typical RPA parameters Eq. 6.5 gives a separation layer width of $d \approx 1-3\,\mathrm{nm}$, which is in good agreement with the simulation results in fig. 6.3. Moreover, one notes that the layer width is much smaller than the slab width, $L_0 \gg d$.

6.2.2 Extended linear theory

The analysis starts with the investigation of the non-relativistic, two fluid model (cf. chapter 3.3). Given the intrinsic scales $l \propto \delta$, $T \propto \omega_{pe}^{-1}$ from Eq. 3.28 one obtains:

$$\partial_{tt}\vec{E} - c^2\Delta\vec{E} + c^2(1 - M_c^2)\nabla\left(\nabla\cdot\vec{E}\right) + \omega_{pe}^2\left(\vec{E} + \vec{u}_e \times \vec{B}\right) = 0 \tag{6.6}$$

Assuming small perturbations $n_e \approx n_{e,0} + \delta n_e$, $\vec{u}_e \approx \delta\vec{u}_e$, $n_i \approx n_{i,0}$, $\vec{u}_i \approx \delta\vec{u}_i$ with $|\delta X| \ll X_0$, as well as $|\delta\vec{u}_e|, |\delta\vec{u}_i| \ll c$, Eq. 6.6 simplifies to:

$$\partial_{tt}\vec{E} - c^2\Delta\vec{E} + c^2(1 - M_{c,0}^2)\nabla\left(\nabla\cdot\vec{E}\right) + \omega_{pe,0}^2\vec{E} = 0 \tag{6.7}$$

For the transverse part of Eq. 6.7 in one dimension one obtains the famous KLEIN-GORDON-EQUATION[67]:

$$\partial_{tt}\vec{E}_\perp - c^2\partial_{xx}\vec{E}_\perp + \omega_{pe,0}^2\vec{E}_\perp = 0, \tag{6.8}$$

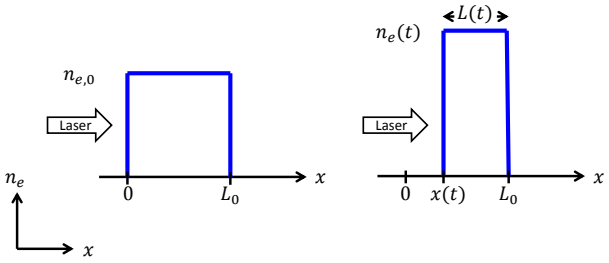

Figure 6.5.: Illustration of the extended linear model: The electrons are assumed to have a step-like distribution of variable dimension $L(t)$ and density $n_e(t)$ at any time and $n_e(t)L(t) = const$, holds.

and the related dispersion relation[68]:

$$\omega^2 = k^2c^2 + \omega_{pe,0}^2 \leftrightarrow k = \pm\frac{\omega}{c}\sqrt{1 - \frac{\omega_{pe,0}^2}{\omega^2}} \tag{6.9}$$

The assumption of a nearly constant electron density n_e contradicts the RPA concept presented in the previous section. Thus, the linear theory is extended by slightly changing the related geometry.

Considering a step density profile of width L for the electrons at any time,

$$n_e = \begin{cases} n_e, & \text{for } x_p(t) \leq x \leq L_0 \\ 0, & \text{otherwise} \end{cases}, \tag{6.10}$$

as depicted in fig. 6.5, the continuity equation reads: $n_e(t)L(t) = n_{e,0}L_0$, where the zero denotes the initial values. Given the compression factor $\kappa_e = n_e(t)/n_{e0}$, the width of the electron distribution is $L(t) = L_0/\kappa_e$ and therefore $\omega_{pe}^2 = \kappa_e\omega_{pe,0}^2$. For over-dense plasmas, $\omega \ll \omega_{pe}$ is essential and thus k from Eq. 6.7 is strictly imaginary and the penetration depth of the electromagnetic wave is $\delta = 1/\Im(k)$, with k from Eq. 6.9. The RPA requires that the slab thickness L is much larger than the penetration depth, $L \gg \delta$, at any time:

Table 6.2.: Example parameters for the verification of the lower target L_{min}, with $I_0 = 2 \cdot 10^{21}\,\mathrm{Wcm^{-2}}$, $\tau_L = 100\,\mathrm{fs}$ and $\lambda = 1\,\mu\mathrm{m}$.

Material	$\rho(\mathrm{kg/m^3})$	Z	n_e	κ_e	$L_{min}(\mathrm{nm})$	$L_0(\mathrm{nm})$
C #1, #2	2250	6	$603 n_c$	$3-4$	$11-13$	8, 16
Ti	4500	22	$1100 n_c$	$3-4$	$8-10$	–

$$\frac{L_0}{\kappa_e} > \frac{c}{\omega}\left(\sqrt{\frac{\omega_{pe,0}^2 \kappa_e}{\omega^2} - 1}\right)^{-1} \tag{6.11}$$

Re-arranging Eq. 6.11, using $c = \omega\lambda/2\pi$ and $\omega_{pe}^2 \gg \omega^2$, finally gives:

$$L_0 > \frac{\sqrt{\kappa_e}}{2\pi}\frac{\omega}{\omega_{pe,0}}\lambda \tag{6.12}$$

Equation 6.12 is an important result: In contradiction to the flying mirror model, which predicts higher acceleration for a more narrow target, Eq. 6.12 provides a lower threshold for the target thickness. An initially too narrow target will be penetrated by the laser and the RPA will collapse. To quantify this, consider the parameters given in tab. 6.2 and a laser wavelength of $\lambda = 1\,\mu\mathrm{m}$. Since the compression κ_e is not accessible by this model, it is anticipated from the results in chapter 6.3. For these conditions, Eq. 6.12 yields $L_0 \geq 11-13\,\mathrm{nm}$ for carbon and $L_0 \geq 8-10\,\mathrm{nm}$ for titanium.

The theoretical predictions are validated against 1D full EM PIC simulations with the parameters listed in tab. 6.2. To emphazise the significance of Eq. 6.12, the initial thickness of target #1 is noticeably lower than the threshold $L_{0,1} < L_{min}$, whereas for target #2 the opposite holds true $L_{0,2} > L_{min}$.

Figure 6.6 shows results of simulation # 1 for different times. As predicted by Eq. 6.12, the target turns transparent to the laser and the RPA collapses after the laser penetrates the entire target. In contrast to that, a stabile acceleration is achieved for the reference case # 2, depicted in fig. 6.7. Summarizing the above results: The final kinetic energy of the plasma will not necessarily benefit from going to even higher laser intensities or thinner targets.

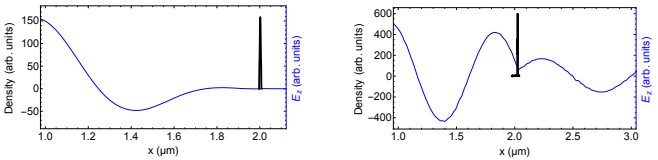

(a) $t = 7.2\,\mathrm{fs}$ **(b)** $t = 30.6\,\mathrm{fs}$

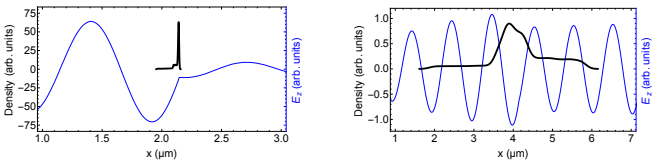

(c) 45.6 fs **(d)** 135.6 fs

Figure 6.6.: Plasma (full black line) at different times for leaky RPA: After compression (middle), the laser wave (blue line) penetrates the entire target and the plasma is rarefied.

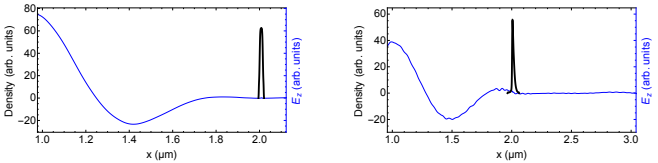

(a) $t = 7.2\,\mathrm{fs}$ **(b)** $t = 30.6\,\mathrm{fs}$

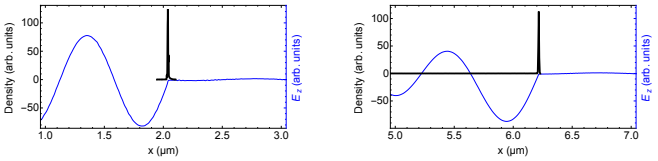

(c) 45.6 fs **(d)** 135.6 fs

Figure 6.7.: Plasma (full black line) at different times for light sail acceleration: The target remains reflective to the laser over the entire time.

6.2.3 Relativistic two fluid model

This section extends the investigation to the relativistic two fluid picture, introduced in chapter 3.3, Eqs. 3.16 together with the 4-tensor Maxwell's Equations 3.7. The derivation carried out here is very similar to the procedure for the linear theory, but the resulting equations have a higher accuracy in terms of $\mathcal{O}(u_e/c)$.

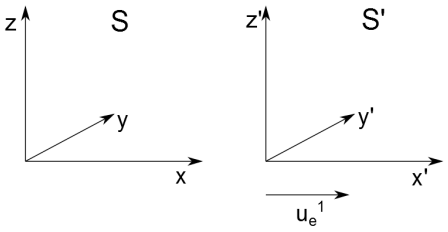

Figure 6.8.: Standard configuration of a laboratory system S and a moving frame S', which propagates in positive x-direction.

Consider a system S', perfectly co-moving with the electrons with velocity u_e^1 in positive x-direction (see Fig. 6.8). Consistently with fig. 6.8, all quantities, evaluated the moving reference frame are labeled with a prime. All derivations are carried out for a linear Lorentz-transformation [54, 55], which in certain circumstances is valid only locally[1]. The sum of the angular momentum is zero $\sum_k L^k = L^e + L^i = 0$ (see appendix B.2 for more detail) and hence, the ratio of the azimuthal velocities is: $\vec{u}'_{i\perp}/\vec{u}'_{e\perp} = m_e/m_i \ll 1$. Therefore the contribution of the ions to the azimuthal current is negligible. This decouples the ions from the perpendicular part of the Maxwell equations and the relativistic equations of motion for the electrons are:

$$\begin{aligned} \partial_{t'} n'_e &= 0 \\ \partial_{t'} u_e^{2,3'} &= \frac{-e}{m_e} E'_{y,z} \\ \partial_{t't'} E'_{y,z} - c^2 \partial_{x'x'} E'_{y,z} &= \frac{e n'_e}{\epsilon_0} \partial_{t'} u_e^{2,3'} \end{aligned} \tag{6.13}$$

Here, t' is the time variable evaluated in S'. In the co-moving system S' the particle concentration $n'_e = n'_e(x')$ is a function of x' only[2].

[1] Locally in this sense means, local in $\mathbb{M}^4$ space-time.

[2] And thus $n_e = \gamma_e n'_e(\gamma_e(x - u_e^1 t))$. The curves $x'(x,t) = \gamma_e(x - v(x,t)t)$ are the characteristic curves of the electron fluid in the x-t-plane.

Similar to the results of the perturbation theory, one obtains a KLEIN-GORDON EQUATION[67]

$$\partial_{t't'}E'_{y,z} - c^2\partial_{x'x'}E'_{y,z} = -\frac{e^2 n'_e}{\epsilon_0 m_e}E'_{y,z}, \tag{6.14}$$

from rearranging Eqs. 6.13, but with higher accuracy. The corresponding dispersion relation is:

$$\omega'^2 = k'^2c^2 + \omega_{pe}^2 \tag{6.15}$$

A Lorentz Transformation with respect to $v = -u_e^1$ re-transforms Eq. 6.15 into the laboratory frame S (see Fig. 6.8):

$$\omega^2 = k^2c^2 + \frac{1+u_e^1/c}{1-u_e^1/c}\omega_{pe}^2 \leftrightarrow k = \pm\frac{\omega}{c}\sqrt{1-\frac{1+\beta_e}{1-\beta_e}\frac{\omega_{pe}^2}{\omega^2}} \tag{6.16}$$

6.2.4 Reflection transmission problem

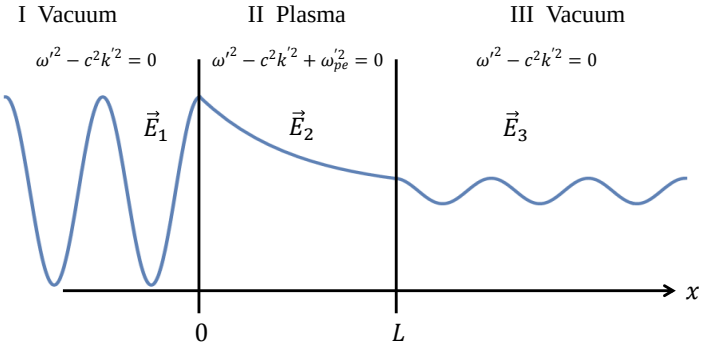

Figure 6.9.: Configuration of the model: The incident laser wave propagates from left to the right through the vacuum region I. Region II is the plasma slab, with the dispersion relation from Eq. 6.14. After the penetration of the plasma, the electromagnetic wave enters vacuum again (region III)

Given that the electron distribution $n_e' = const$ is independent of x' and t' in S', the configuration shown in fig. 6.9 is examined. The EM wave satisfies D'ALEMBERT'S EQUATION in the vacuum region and the KLEIN-GORDON EQUATION (see Eq. 6.14) in the plasma, together with the continuity conditions:

$$\begin{aligned} E_\perp'^{I}(0,t') &= E_\perp'^{II}(0,t') \\ \partial_{x'} E_\perp'^{I}(0,t') &= \partial_{x'} E_\perp'^{II}(0,t') \\ E_\perp'^{II}(L',t') &= E_\perp'^{III}(L',t') \\ \partial_{x'} E_\perp'^{II}(L',t') &= \partial_{x'} E_\perp'^{III}(L',t'), \end{aligned} \tag{6.17}$$

where the absence of surface currents and charges is assumed. It is beneficial to apply Fourier-transform[68] to Eqs. 6.14 and 6.17 and provide the solution in frequency domain. The wave numbers in the regions $I - III$ are: $ck_I' = \omega'$, $c^2 k_{II}'^2 = (\omega^{2\prime} - \omega_{pe}^{2\prime})$ and $ck_{III}' = \omega'$. The amplitude of the incident laser wave in frequency domain is denoted by $\hat{F}_i'$, whereas $\hat{F}_r'$ is the amplitude of the reflected wave. From the solution of the problem shown in fig. 6.9, one obtains for the reflection index $R'(\omega', L')$[3]:

$$\begin{aligned} R'\left(\omega'\right) &= \left| \frac{\hat{F}_r'(\omega')}{\hat{F}_i'(\omega')} \right|^2 \\ &= \left| \frac{\left(k_I' - k_{II}'\right)\left(k_I' + k_{II}'\right)\sin\left(k_{II}' L'\right)}{2ik_I' k_{II}' \cos\left(k_{II}' L'\right) + \left(k_I^{2\prime} + k_{II}^{2\prime}\right)\sin\left(k_{II}' L'\right)} \right|^2 \end{aligned} \tag{6.18}$$

Figure 6.10 shows the reflection index as a function of the frequency $R'(\omega')$ for different target thicknesses L'. For frequencies $|\omega'| < \omega_{pe}'$, $R \approx 1$, but for $|\omega'| > \omega_{pe}'$ the plasma slab acts as a nonlinear[4] FABRI-PERÒT-ETALON[69]: The vacuum-plasma interfaces on the front and rear surface of the plasma act as partially reflective mirrors, whilst the plasma in between the interfaces serves as an optical medium. Contrary to the classical Fabri-Peròt-Etalon, the EM wave is evanescent in the plasma slab, with a frequency dependent refraction index $N = N(\omega') \in \mathbb{C}$. In addition, the reflection coefficient of the plasma slab is a function of the frequency and the slab width, $R = R(\omega', L')$, whereas it is a constant for the traditional Fabri-Peròt-Etalon. Therefore, if the plasma width tends to zero, $L' \to 0$, the reflective index will shrink to zero, too.

[3] A full solution in the frequency domain is given in the Appendix B.4.

[4] Nonlinear means nonlinear with respect to ω'.

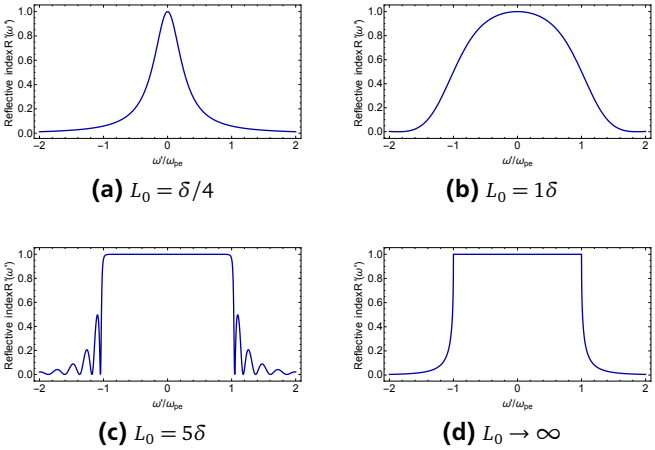

(a) $L_0 = \delta/4$ **(b)** $L_0 = 1\delta$

(c) $L_0 = 5\delta$ **(d)** $L_0 \to \infty$

Figure 6.10.: Reflection index $R = R(\omega', L')$ from Eq. 6.18 for different target thicknesses.

Given that $\hat{F}_t'^2 = (1 - R(\omega'))\hat{F}_i'^2$, the high frequency parts of the incident laser pulse are transmitted through the plasma. Here, $\hat{F}_t'$ denotes the amplitude of the transmitted electric field. This is qualitatively shown in Fig. 6.11 for a Gaussian intensity profile. From Eq. 6.5 follows:

$$u_e'^j\left(\omega', x'\right) = \frac{ie}{m_e\omega'} F_j'\left(x', \omega'\right), \quad j = 2, 3 \tag{6.19}$$

According to Eq. 6.19 each transmitted frequency ω' results in a particular azimuthal electron velocity $u_e'^{2,3}(\omega')$. Using the relation $\vec{B}_\perp' = c^{-1}\hat{k} \times \vec{E}_\perp'$ and the CONVOLUTION THEOREM for Fourier Transformation, the longitudinal electron velocity $u_e'^1$ is:

$$\begin{aligned} \partial_{t'} u_e'^1 &= -\frac{e}{m_e c}\vec{u}_{e,\perp}' \cdot \vec{E}_\perp' = -\frac{e}{m_e c}\sum_i u_e'^i E_i', \quad i = 2, 3 \\ \Rightarrow u_e'^1(\omega') &= -\frac{ie}{m_e\omega' c}\sum_i \int_{-\infty}^{\infty} F_i'(\Omega') u_e'^i(\omega' - \Omega') d\Omega' \end{aligned} \tag{6.20}$$

Inserting Eq. 6.19 into Eq. 6.20 one obtains:

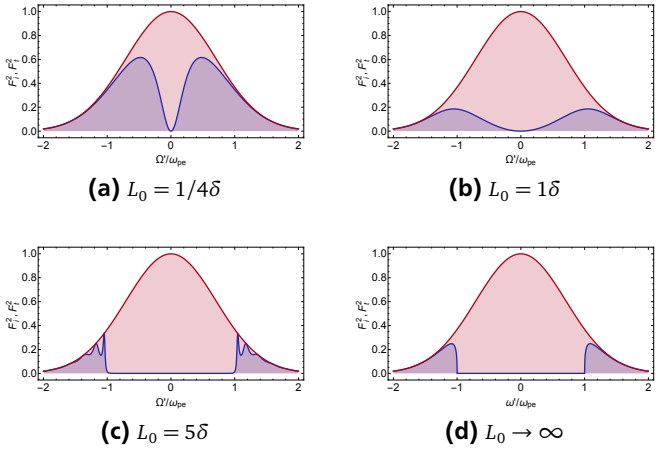

(a) $L_0 = 1/4\delta$ **(b)** $L_0 = 1\delta$

(c) $L_0 = 5\delta$ **(d)** $L_0 \to \infty$

Figure 6.11.: Incident wave energy band $\hat{F}_i^2(\omega')$ (red) and transmitted wave energy $\hat{F}_t^2(\omega')$ (blue) in frequency domain for different target thicknesses.

$$u_e'^1(\omega') = -\frac{ie^2}{m_e^2\omega' c}\sum_i \int_{-\infty}^{\infty} \frac{F_i'(\Omega')F_i'(\omega'-\Omega')}{\omega'-\Omega'}d\Omega', \quad i = 2,3 \tag{6.21}$$

Equation 6.21 reveals an important result: Each laser frequency ω' transmitted into the plasma results in a different longitudinal velocity. Thus, a laser with a finite pulse length results a broad velocity band rather than a single velocity. This effect leads to the velocity spread in the RPA mechanism. To minimize the velocity spread it is therefore necessary to minimize the amount of transmitted laser energy. This goal is achieved by choosing an incident laser signal, with a frequency band in the range $-\omega_{pe} < \omega' < \omega_{pe}$.

From the properties of the Fourier Transformation follows that a signal short in time domain has a broad signal in frequency domain and a signal slowly varying in time has a narrow frequency band.

Given a set of laser pulses with varying intensity and pulse duration and fixed energy density

$$\varepsilon_L = \int_0^\infty I(t)dt \propto I_0\tau = const, \tag{6.22}$$

the lowest velocity spread is realized for the signal with the longest pulse duration, whereas the average kinetic energy $\bar{W}_{kin} \propto (I_0\tau_L)^2$ (see Eq. 6.2) remains constant.

A set of 1D full EM PIC simulations with the parameters given in tab. 6.3 and 6.4 validates the analytical predictions and quantifies the optimization.

Table 6.3.: Laser parameters, with $I_0\tau_L = const$.

I_0 ($\times 10^{21}$ W/cm^2) :	20	10	7.5	5	3.3	2.5	1.25	0.625
τ_L (fs) :	16.25	32.5	43.33	65	97.5	130	260	520

Table 6.4.: Target parameters, with $A_0 = const$.

Target :	ρ_0(kg/m^3)	L_0(nm)	Z	a_0(arb.units)
Au :	19320	25	+15	0.075
C :	2250	25	+6	0.64
H :	1000	25	+1	1.44

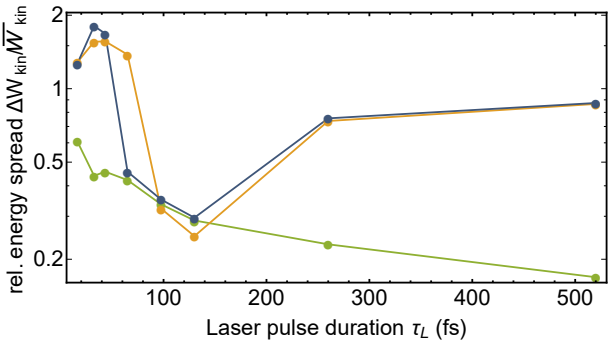

Figure 6.12.: Relative energy spread $\Delta W_{kin}/\bar{W}_{kin}$ as a function of the laser pulse duration for carbon (blue), gold (green) and hydrogen (orange).

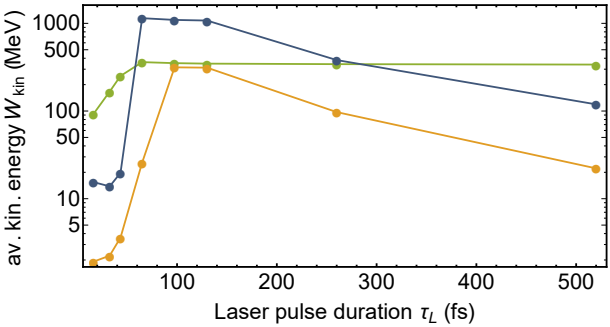

Figure 6.13.: Average kinetic energy $\bar{W}_{kin}$ as a function of the laser pulse duration for carbon (blue), gold (green) and hydrogen (orange).

Figure 6.12 shows the relative energy spread ΔW_{kin} relative to the mean energy $\bar{W}_{kin}$ as a function of the laser pulse duration. As predicted by Eq. 6.21, the velocity spread decreases with increasing pulse length. The average kinetic energy is depicted in fig. 6.13. Combining the results from fig. 6.12 and fig. 6.13, the optimum pulse duration is located at the minimum of the relative energy spread, where the average kinetic has its maximum. Below a certain pulse duration (cf. fig. 6.13, $\tau \approx 50 - 60\,\mathrm{fs}$) the average kinetic energy decreases rapidly, since the target is transparent to the laser and the RPA is terminated. Moreover one obtains from fig. 6.13 a reduction of $\bar{W}_{kin}$ for longer laser pulses. This indicates the existence of a minimum intensity, below which the RPA does not occur, even for infinite

laser pulses. A tasks of the subsequent chapter is the determination of an intensity threshold.

Subsequently, the numerical indications are supported by analytical scaling laws. Consider a plasma half-space $L \to \infty$ and the laser profile:

$$I_L(t) = I_0 \frac{4t^2}{\tau_L^2} \exp\left(-4t^2/\tau_L^2 + 1\right) \tag{6.23}$$

This laser model is useful for analytic calculations, since it is nearly Gaussian shape, with a full width half maximum (FWHM) width of τ_L and additional to that, fulfills the initial conditions $I(0) = 0$, $d_t I(0) = 0$ and is thus consistent with the initial conditions of the plasma. The total energy of the incident laser pulse is:

$$W_{EM,i} = \int_0^\infty \epsilon_0 c \hat{E}_i^2(t) dt \Big|_{x=0} \tag{6.24}$$

According to PLANCHEREL'S THEOREM for the energy transmitted into the plasma one obtains:

$$\begin{aligned} W_{EM,t} = \int_0^\infty \epsilon_0 c \hat{E}_t^2(t) dt \Big|_{x=0} &= \int_{-\infty}^\infty \epsilon_0 c \hat{F}_t^2(\omega) d\omega \Big|_{x=0} \\ \Rightarrow W_{EM,t} &= \int_{-\infty}^\infty \epsilon_0 c T(\omega) \hat{F}_i^2(\omega) d\omega \Big|_{x=0} \\ \Rightarrow W_{EM,t} &= \int_{-\infty}^\infty \epsilon_0 c \left(1 - R(\omega)\right) \hat{F}_i^2(\omega) d\omega \Big|_{x=0}, \end{aligned} \tag{6.25}$$

where $\hat{F}_i^2(\omega) = \hat{F}_{i,x}^2(\omega) + \hat{F}_{i,y}^2(\omega)$. From Eq. 6.25 one obtains the scaling laws for the plasma energy spread:

$$\begin{aligned} W_{EM,t} &\approx \frac{\sqrt{\pi}}{8} \frac{\omega^4 \tau_L^3}{\omega_{pe}^2} I_0 \exp\left(-1/4\omega^2\tau_L^2 + 1\right) + \mathcal{O}\left(\frac{\omega^2 \tau_L}{\omega_{pe}^2}\right) \\ \frac{W_{EM,t}}{W_{EM,i}} &\approx \frac{1}{2} \frac{\omega^4 \tau_L^2}{\omega_{pe}^2} \exp\left(-1/4\omega^2\tau_L^2\right) + \mathcal{O}\left(\frac{\omega^2 \tau_L}{\omega_{pe}^2}\right) \end{aligned} \tag{6.26}$$

In order to connect Eq. 6.26 with the initial thermal distribution of the plasma, one applies statistics and obtains:

$$\begin{aligned} \Delta W_{kin} &\propto \sqrt{W_{trans}^2 + \Delta W_{th}^2} \\ \frac{\Delta W_{kin}}{\bar{W}} &\propto \frac{\sqrt{W_{trans}^2 + \Delta W_{th}^2}}{W_{laser} + W_{th}}, \end{aligned} \tag{6.27}$$

where W_{th} is the average thermal energy and ΔW_{th} is the related standard deviation. Thermal effects are not included in the analytical derivation and are therefore fitted. A comparison of the results from Eqs. 6.27 with simulations is shown in fig. 6.14 and 6.15. Within the parameter range where $\bar{W}_{kin} \propto (I_0 \tau_L)^2 = const$ is valid, good agreement is achieved, whereas the analytical results deviate from the simulation in case of collapsing RPA (short pulse duration).

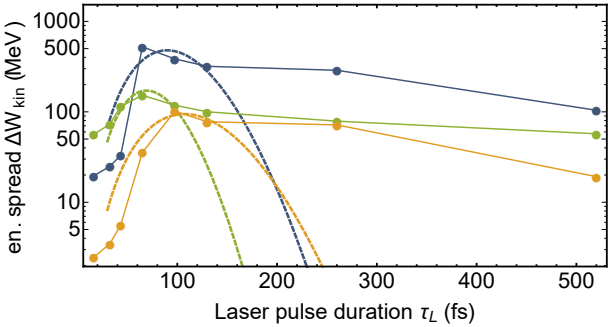

Figure 6.14.: Plasma energy spread as a function of τ_L for carbon (blue), gold (green) and hydrogen (orange). The dashed lines are from an analytical fit of Eq. 6.26.

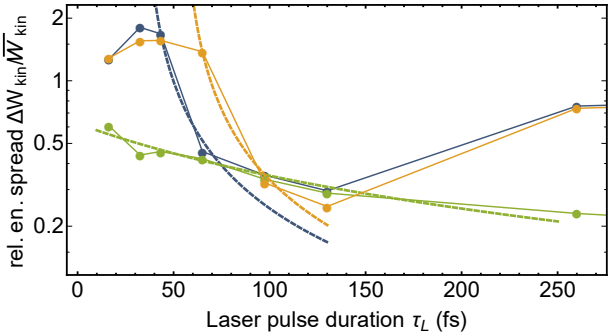

Figure 6.15.: Relative energy spread as a function of τ_L for carbon (blue), gold (green) and hydrogen (orange). The dashed lines are from an analytical fit of Eq. 6.27.

6.3 RPA in the limit of large scales

This section presents the RPA dynamics related to large scales $l \gg \delta$, $T \gg \omega_{pe}^{-1}$. For this case, l, T are of the order of the target width $l \propto L$ and the laser pulse duration $T \propto \tau_L$ and the equations of motions reduce to the equations of classical gas-dynamics (cf. section 3.3.2) and electron dynamics are negligible on this scale. The author published the results presented in this section in [66].

6.3.1 The gas-dynamics laser piston model

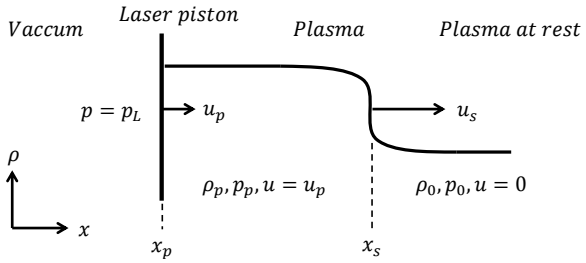

Figure 6.16.: Schematic of the piston model for RPA; The laser drives an artificial piston that compresses the plasma and creates a shock wave.

The plasma is modeled as a quasi neutral $Zn_i \approx n_e$, non-relativistic single fluid slab of width L with an initially uniform mass density $\rho_0 \approx n_{i,0} m_i$. In addition, the plasma is assumed to be highly over-dense to the laser $n_e \gg n_c$, the reflective index $R \approx 1$ and the electron temperature is assumed to be much larger than the ion temperature $T_e \gg T_i$.

Figure 6.16 illustrates the piston model: a circularly polarized laser with a given radiation pressure p_L acts as a piston (coordinate $x = x_p$, velocity $d_t x_p = u_p$). Downstream of the piston a shock wave (coordinate $x = x_s$) with velocity u_s forms, so that between the piston and the shock wave there is a region with parameters p_1, ρ_1 and u_1. In front of the shock wave the plasma remains unperturbed with its initial state p_0, ρ_0, $u_0 = 0$. Here, $p_0 = n_{e0} k_B T_{e0}$ is the initial electron pressure. The conservation of mass as well as the conservation of momentum then state (cf. chapter 3.3):

$$\begin{aligned} \partial_t \rho + u \partial_x \rho + \rho \partial_x u &= 0 \\ \partial_t u + \rho^{-1} \partial_x p + u \partial_x u &= 0 \end{aligned} \tag{6.28}$$

This system is completed by an isentropic equation of state:

$$p = p_0\left(\frac{\rho}{\rho_0}\right)^{\varkappa} \quad \Longleftrightarrow \quad \rho = \rho_0\left(\frac{p}{p_0}\right)^{1/\varkappa} \tag{6.29}$$

The system is rewritten in the dimensionless variables $\xi = a_0 t$, $u \to a_0 u$, $p \to p_0 p$, where

$$a_0^2 = \left.\frac{\partial p}{\partial \rho}\right|_{\rho=\rho_0} = \frac{\varkappa p_0}{\rho_0} \tag{6.30}$$

is the square of the isentropic sound speed in the unperturbed plasma. Rearranging Eqs. 6.28 one obtains:

$$\begin{aligned} &\partial_\xi p + u\partial_x p + \varkappa p \partial_x u = 0 \\ &\partial_\xi u + \varkappa^{-1} p^{-1/\varkappa}\partial_x p + u\partial_x u = 0 \end{aligned} \tag{6.31}$$

By introducing the state vector $Z = (p,u)^T$, the state form of Eqs. 6.31 is[70, 67]:

$$\partial_\xi Z + A\partial_x Z = \frac{\partial}{\partial \xi}\begin{pmatrix} p \\ u \end{pmatrix} + \begin{pmatrix} u & \varkappa p \\ \varkappa^{-1} p^{-1/\varkappa} & u \end{pmatrix}\frac{\partial}{\partial x}\begin{pmatrix} p \\ u \end{pmatrix} = \begin{pmatrix} 0 \\ 0 \end{pmatrix} \tag{6.32}$$

Applying the RIEMANN CHARACTERISTICS METHOD[71] for simple waves, one calculates the eigenvalues and eigenvectors of matrix A^T:

$$\lambda_{1,2} = u \mp p^{\frac{\varkappa-1}{2\varkappa}}, \quad L_{1,2} = \begin{pmatrix} \mp\varkappa^{-1} p^{-\frac{\varkappa+1}{2\varkappa}} \\ 1 \end{pmatrix} \tag{6.33}$$

Next, the system is rearranged into a system of ordinary differential equations[52, 67, 70]:

$$C_\mp: \quad \frac{dx_\mp}{d\xi} = u \mp p^{\frac{\varkappa-1}{2\varkappa}}, \quad \varkappa^{-1}\frac{dp}{d\xi}p^{-\frac{\varkappa+1}{2\varkappa}} \mp \frac{du}{d\xi} = 0 \tag{6.34}$$

Integrating over ξ as well as using the initial condition $u(x,0) = 0$, $p(x,0) = 1\ \forall x \geq 0$ results in

$$C_-: \quad \frac{dx_-}{d\xi} = u - p^{\frac{\varkappa-1}{2\varkappa}}, \quad \frac{2}{\varkappa-1}p^{\frac{\varkappa-1}{2\varkappa}} - u = \frac{2}{\varkappa-1} \tag{6.35}$$

for the C_- characteristics. From this RIEMANN INVARIANT one obtains a relation for the velocity and pressure[67]:

$$p^{\frac{\varkappa-1}{2\varkappa}} = 1 + \frac{\varkappa-1}{2}u \tag{6.36}$$

Combining Eqs. 6.34 and 6.36 one obtains:

$$C_+ : \quad \frac{dx}{d\xi} = 1 + \frac{\varkappa+1}{2}u \tag{6.37}$$

For those of the C_+ characteristics, which start on the x-axis with $x \geq 0$, $u = 0$ holds within Eq. 6.37. C_+ characteristics, which leave the piston at the time $\xi = \tau$, fulfill the boundary conditions $u = u_p(\tau)$ and $x(\tau) = x_p(\tau)$. Thus it is[52, 67, 71, 70]:

$$x(\xi) = x_K(\tau) + \left(1 + \frac{\varkappa+1}{2}u_K(\tau)\right)(\xi - \tau) \tag{6.38}$$

Since the momentum flux is steady at the piston, the laser is related to the piston motion[72]. The momentum flux of the laser is given by the Poynting vector $\vec{S}$:

$$\frac{2|\vec{S}|}{c} = \rho_p u_p u_p + p_p, \quad x = x_p \tag{6.39}$$

Here, perfect reflectivity of the plasma interface is assumed. From the thermodynamic relation Eq. 6.29, ρ_p and p_p are interchanged:

$$p_L = \varkappa p_p^{1/\varkappa} u_p u_p + p_p, \quad x = x_p \tag{6.40}$$

By using the relation between POYNTING VECTOR and radiation pressure: $p_L = 2S/c$. From Eq. 6.36 one calculates the pressure at the piston and relates p_p with u_p:

$$\begin{aligned} p_p^{1/\varkappa} &= \left(1 + \frac{\varkappa-1}{2}u_p\right)^{\frac{2}{\varkappa-1}} \\ p_p &= \left(1 + \frac{\varkappa-1}{2}u_p\right)^{\frac{2\varkappa}{\varkappa-1}} \end{aligned} \tag{6.41}$$

Equations 6.41 shows crucial difference to existing calculations (see e.g. [72]): Due to the assumption of a finite plasma temperature, additional correction terms

$p_p^{1/\varkappa}$ and p_p appear on the right hand side of Eq. 6.40. These terms represent the extra work the piston must provide for the compression of the plasma.

The isentropic exponent is $\varkappa = (f+2)/f$ in the non-relativistic limit and $\varkappa = (f+1)/f$ for the relativistic limit, where f is the electron degree of freedom, as shown in [49].

Using BERNOULLI'S INEQUALITY, an approximate expression for Eqs. 6.41 is:

$$\begin{aligned} p_p^{1/\varkappa} &= \left(1+\frac{\varkappa-1}{2}u_p\right)^{\frac{2}{\varkappa-1}} \approx 1+u_p \\ p_p &= \left(1+\frac{\varkappa-1}{2}u_p\right)^{\frac{2\varkappa}{\varkappa-1}} \approx 1+\varkappa u_p \end{aligned} \tag{6.42}$$

Combining Eqs. 6.40 and 6.42 one obtains:

$$p_L \approx 1+\varkappa(1+u_p+u_p^2)u_p, \quad x = x_p \tag{6.43}$$

For $\varkappa = 5/3$, Eq. 6.40 together with Eqs. 6.41 give a fifth order polynomial with purely positive, real coefficients. Then, the FUNDAMENTAL THEOREM OF ALGEBRA together with the ABEL-RUFFINI THEOREM (see e.g. [56]) imply that there exists only one isolated real root and by that ensure the uniqueness of the solution.

6.3.2 Derivation of the minimum laser intensity

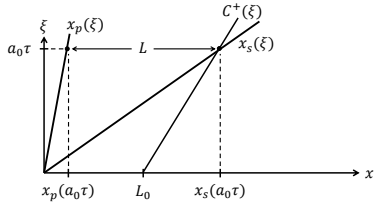

(a) Case $u_p < 1$: Since $L > L_0$ holds for $\xi = a_0\tau$, no net compression is achieved.

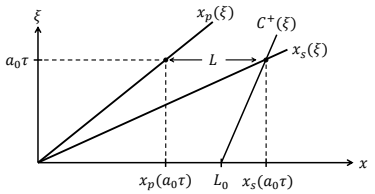

(b) Case $u_p > 1$: Since $L < L_0$ holds for $\xi = a_0\tau$, compression is achieved.

Figure 6.17.: Piston $x_p(\xi)$, shock wave $x_s(\xi)$ and wave front C^+, for $u_p < 1$ and $u_p > 1$, respectively.

From gas-dynamics for piston driven simple waves, a piston motion with $u_p > 0$ results in a shock wave, independent of how small u_p is. However, contrary to this, a minimum intensity is necessary to start the RPA process.

It is well known from simulation experience[33], that below a certain intensity limit, this acceleration mechanism will not occur, even for long pulse lengths. This contradiction can be resolved by realizing that a strong compression process like the RPA requires a strong shock, an envelope wave, rather than a weak shock. To produce a strong shock, the piston must move into the plasma with a supersonic Mach number[67, 71] $u_p > 1$.

To illustrate this, fig. 6.17a shows the piston trajectory $x_p(\xi)$, shock wave $x_s(\xi)$ and the wave front C^+ characteristic $C^+(\xi)$ for a piston with constant velocity $u_p < 1$, whereas fig. 6.17b shows the same for $u_p > 1$. The simple wave model analysis is only valid until the shock wave intersects the wave front C^+ characteristic, denoted by $\xi = a_0\tau$. The width of the plasma slab at this point in time is given by $L(a_0\tau) = x_s(a_0\tau) - x_p(a_0\tau) = C^+(a_0\tau) - x_p(a_0\tau)$. Obviously, in case $u_p < 1$ (cf. fig. 6.17a), the slab width L is larger than the initial target thickness L_0, such that no net compression is achieved. On the other hand, for $u_p > 1$ as in fig. 6.17b, the slab width L is shorter than L_0. A net compression is achieved only if $u_p > 1$.

Inserting the threshold limit $u_p = 1$ into Eq. 6.43, one obtains the desired threshold for the laser pressure:

$$p_L > 1 + 3\varkappa \tag{6.44}$$

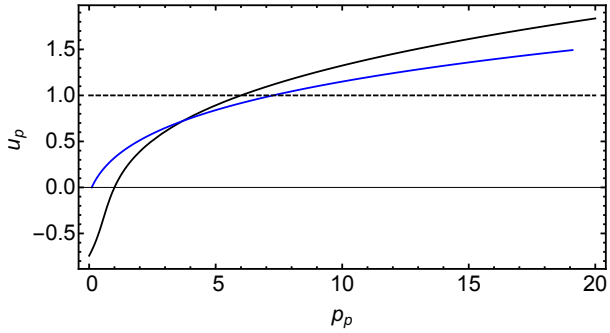

Figure 6.18.: Comparison of the solution of Eq. 6.43 (black) with the solution of Eqs. 6.40, 6.41 (blue) for $\varkappa = 5/3$: The approximate solution overestimates the piston velocity u_p, where it reaches the threshold value $u_p = 1$ at a laser pressure of $p_L = 6$, while the exact solution reaches this value at $p_L \approx 8.2$.

Table 6.5.: Example parameters for validation of the lower intensity limit I_L.

$n_{e,0}(\mathrm{m}^{-3})$	$W_{th,e,0}(\mathrm{keV})$	$T_e(\mathrm{K})$	u_p	$I_{L,min}(\times 10^{19}\,\mathrm{W/cm^2})$
10^{30}	1.3	$\approx 10^7$	1, 5	1.7, 190

A more accurate result is obtained by employing the exact Eqs. 6.41 instead of Bernoulli's inequality. Figure 6.18 shows the solution of Eqs. 6.41, 6.40 and the approximate solution of Eq. 6.43, respectively. As shown, the threshold velocity $u_p = 1$ is reached at $p_L = 6$ for the approximate solution and at $p_L \approx 8.2$ for the exact solution. Moreover, note that below $p_L < 1$ the piston recedes since the hydrostatic pressure in the plasma is higher than the radiation pressure of the laser. Since the curves are flattening, that is $d_{pp}u_p(p) < 0$, the required intensity for reaching high Mach numbers drastically increases.

To quantify this, consider the examples given in tab. 6.5: The computed thresholds for $I_{L,min}$ are in good agreement with the known thresholds.

6.3.3 Derivation of a maximum target thickness

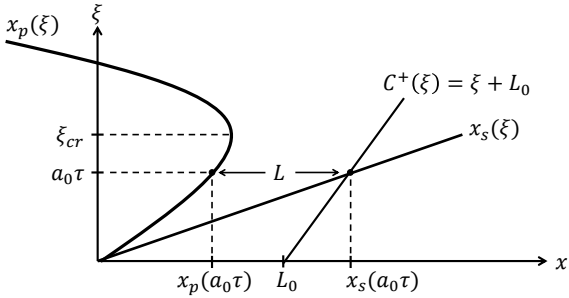

Figure 6.19.: Schematic of the piston characteristic $x_p(\xi)$, the shock $x_s(\xi)$ and the wave front C^+ for a laser with finite pulse duration. The turning point of the laser is denoted with $\xi_{cr} = a_0\tau_{cr}$ and $a_0\tau \leq \xi_{cr}$ is required at the shock-C^+ intersection.

This section presents the derivation of an upper threshold for the target width L_0. After the laser piston starts to move a shock wave runs into the plasma slab (cf. fig. 6.17b). The plasma between the shock front x_s and the piston x_p has the velocity $u = u_p$. When this shock wave reaches the wave front C^+ of the slab, it is reflected and after some time intersects the piston path again, creating a new shock wave. The simple wave analysis is restricted to $\xi \leq a_0\tau$ (cf. fig. 6.17b, 6.19). For a piston moving with a constant velocity $u_p = const$, the velocity of the shock wave is[71]:

$$u_s = \frac{1}{2}\frac{u_p}{1-\mu^2} + \sqrt{1 + \frac{1}{4}\left(\frac{u_p}{1-\mu^2}\right)^2}, \quad \mu^2 = \frac{\varkappa - 1}{\varkappa + 1} \tag{6.45}$$

For simplicity, in the case of an ultra-fast piston, that is $u_p \gg 1$, the shock wave can be approximated by[71] (see fig. 6.20):

$$u_s \approx \frac{u_p}{1-\mu^2}, \quad u_p \gg 1 \tag{6.46}$$

From Eq. 6.46 one obtains $u_s > u_p$. Given a laser with a finite pulse duration τ_L, at some point the radiation pressure of the laser p_L falls below the plasma pressure p_p and the laser piston is decelerated (cf. fig. 6.19). The piston path x_p will have a turning point at $\xi_{cr} = a_0\tau_{cr}$, where $u_p = 0$, after which the piston turns into a

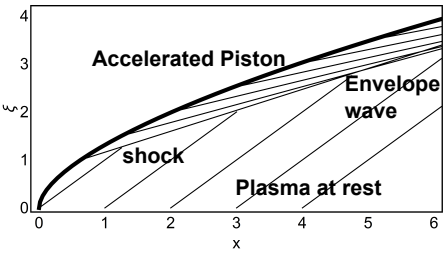

Figure 6.20.: An example of a strong shock compression $u_p \gg 1$: The piston (thick line) is closely attached to the envelope wave (thin lines).

receding piston (cf. fig. 6.19). Hence, for significant acceleration, the shock wave $x_s(\xi)$ must intersect the wave front C^+ characteristic for some $\tau \leq \tau_{cr}$.

In case the laser piston starts receding before the shock intersects the wave front C^+ characteristic, the acceleration process remains incomplete. The C_+ characteristic which starts at $x = L_0$ is: $C_+ : \; x = L_0 + \xi$. The piston path $x_p(\xi)$ can be derived by integrating Eq. 6.40 or 6.41 and 6.43, respectively. Assuming the simplest case of a shock wave with constant velocity $u_s = const$, one obtains:

$$\begin{aligned} L_0 + a_0\tau = u_s\tau, \quad \tau \leq \tau_{cr} \\ \Longrightarrow L_0 \leq \tau_{cr}\,(u_s - a_0) \end{aligned} \tag{6.47}$$

From fig. 6.19 one obtains, that the intersection point occurs at:

$$L_0 + a_0\tau = x_p(a_0\tau) + L(a_0\tau), \tag{6.48}$$

where the slab width is given by $L(a_0\tau) = x_s(a_0\tau) - x_p(a_0\tau)$. In the case that the rarefaction wave at the back interface of the plasma slab expands much slower than the shock wave, $u_s \gg a_0$, mass conservation implies that: $\rho_0 L_0 \approx \rho_p L$, where ρ_p is the plasma density at the piston in the region $x_p \leq x \leq x_s$. Fortunately, ρ_p can be determined by Eqs. 6.29, 6.40 and 6.41 and hence $L \approx \rho_0 L_0/\rho_p$. Moreover assuming $u_p = const$, from Eqs. 6.47 and 6.48, the shock velocity u_s is:

$$u_s - a_0 = \frac{u_p - a_0}{1 - \rho_0/\rho_p} \tag{6.49}$$

With the result from Eq. 6.47 the condition for the thickness threshold is:

Table 6.6.: Example parameters for upper target thickness limit. The laser has a Gaussian temporal profile.

Mat.	$\rho_0(\mathrm{kg/m^3})$	$W_{th,e,0}(\mathrm{keV})$	$I_0(\mathrm{W/cm^2})$	$\tau_L(\mathrm{fs})$
Ti^{+22}	4500	6.5	$1 \cdot 10^{21}$	100

$$L_0 \leq \frac{x_p(a_0\tau) - a_0\tau}{1 - \rho_0/\rho_p}, \quad \tau \leq \tau_{cr} \tag{6.50}$$

Note, that $\rho_0/\rho_p < 1$ and the inequality in Eq. 6.50 results from the requirement $\tau \leq \tau_{cr}$. To quantify this, consider the parameters given in tab. 6.6:

Eq. 6.50 together with 6.41 and 6.40 gives $L_0 < 368\,\mathrm{nm}$ and $u_{p,max} \approx 1.7$. For a twice as high intensity $2I_0$, the target may be extended to $L_0 < 525\,\mathrm{nm}$. When the piston is subsonic $u_p < 1\ \forall \xi \in [0, a_0\tau]$, Eq. 6.50 yields $L_0 < 0$, which means the acceleration process is always incomplete.

6.3.4 Validation of the intensity limit

Table 6.7.: Simulation parameters for validation of intensity threshold. The CP laser has a wavelength $\lambda = 1\,\mu\mathrm{m}$ and infinite pulse duration.

Sim. #	$n_{e,0}$	$W_{th,e,0}(\mathrm{keV})$	$p_{e,0}(\times 10^{13}\,\mathrm{Pa})$	$a_0(\mathrm{m/s})$	I_L in I_{th}
1, 2, 3	$25n_c$	13	3.85	$2.7 \cdot 10^6$	1, 0.2, 5

The theoretical predictions are validated by a set of 1D full EM PIC simulations, with the parameters listed in tab. 6.7 and $f = 1$ degrees of freedom, as well as $\varkappa = 3/2$. The target plasma is neutral and consists of ions and the corresponding electrons and has a width of $L_0 = 5\,\mu\mathrm{m}$. For the parameters listes in tab. 6.7, Eqs. 6.40 and 6.41 yield a minimum laser intensity of $I_{L,thr} \geq 9.4 \cdot 10^{18}\,\mathrm{W/cm^2}$.

To illustrate the significance of the intensity threshold, simulation # 1 is performed with the exact threshold intensity $I_L = I_{L,thr}$ (see fig. 6.21), simulation # 2 is performed with an intensity well below the threshold $I_L = 0.2I_{L,thr}$ (see

fig. 6.22) and simulation # 3 is performed with an intensity well above the limit $I_L = 5I_{L,thr}$ (see fig. 6.23). The choice of an infinite pulse length corresponds to the most simple case of a piston moving with constant velocity and decouples the acceleration process from its dependence on the target thickness, which is addressed later. The results from simulation # 1 are shown in fig. 6.21 for different times: as illustrated in fig. 6.17b, a strong shock is achieved, which separates the compressed region $x_p < x < x_s$ from the unperturbed plasma $x > x_s$. Figure 6.22 shows the results of simulation # 2: As indicated in fig. 6.17a, for $u_p < 1$, no compression wave is produced (see also Eq. 6.44). The front interface of the plasma is slightly compressed, but the rear interface rarefies, such that the overall width of the slab $L(\xi) = C^+(\xi) - x_p(\xi)$ increases. In case three (cf. fig. 6.23) in contrast to case one, the piston, as well as the shock wave move faster, but the larger energy transfer the laser leads to a considerably stronger smoothing and rarefaction of the plasma. Figure 6.24 shows a comparison of the piston motion from Eq. 6.43 and the shock wave motion from Eq. 6.45 with the results of simulation # 1. Good agreement is achieved and thus confirms the analytical model.

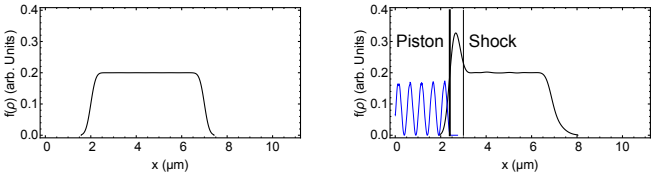

(a) $t = 0\,\mathrm{fs}$. **(b)** $t = 167\,\mathrm{fs}$.

(c) $t = 333\,\mathrm{fs}$. **(d)** $t = 500\,\mathrm{fs}$.

Figure 6.21.: Plasma distribution (black), laser wave (blue), piston position (thick vertical) and shock wave (thin vertical), for $I_L = I_{L,thr}$.

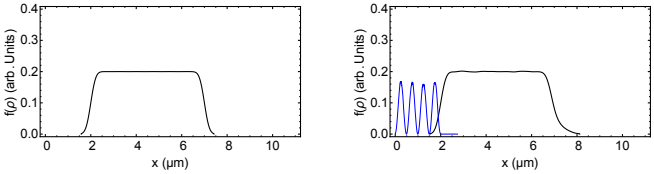

(a) $t = 0\,\mathrm{fs}$. **(b)** $t = 167\,\mathrm{fs}$.

(c) $t = 333\,\mathrm{fs}$. **(d)** $t = 500\,\mathrm{fs}$.

Figure 6.22.: Plasma distribution (black) and the laser wave (blue), for $I_L = 0.2 I_{L,thr}$.

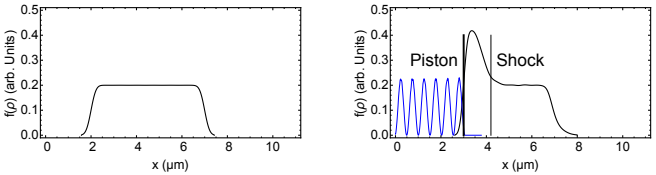

(a) $t = 0\,\mathrm{fs}$. **(b)** $t = 167\,\mathrm{fs}$.

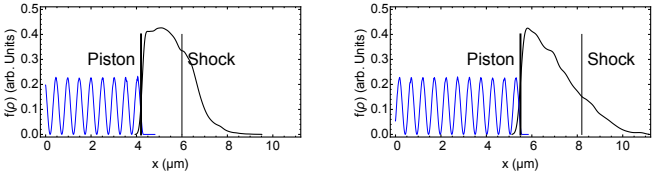

(c) $t = 333\,\mathrm{fs}$. **(d)** $t = 500\,\mathrm{fs}$.

Figure 6.23.: Plasma distribution (black), laser wave (blue), piston position (thick vertical) and shock wave (thin vertical), for $I_L = 5I_{L,thr}$.

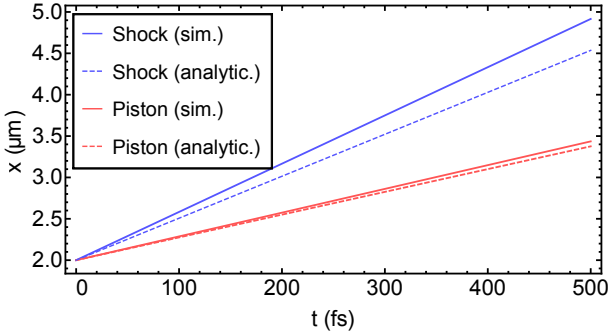

Figure 6.24.: Comparison of the piston motion and shock wave from the 1D PIC simulation with the analytical results from Eq. 6.43 and Eq. 6.45 for $I_L \approx I_{L,thr}$.

6.3.5 Validation of the target thickness threshold

Table 6.8.: Simulation parameters for validation of intensity threshold. The CP laser has a wavelength of $\lambda = 1\,\mu$m and a Gaussian temporal profile.

Sim. #	$n_{e,0}$	$W_{th,e,0}$(keV)	L_0(nm)	I_L(W/cm^2)	τ_L
1, 2	$1100n_c$	13	75, 375	10^{21}	100

The maximum permissible target thickness (cf. Eqs. 6.48 and 6.50) is also validated by a set of 1D PIC simulations, given the parameters in tab. 6.8. From Eq. 6.50 one obtains a thickness limit of $L \approx 368\,$nm. For thicker targets, Eq. 6.50 predicts an imperfect acceleration.

Similar to the previous section two simulations are compared: simulation # 1 is performed with a $L_0 = 75\,$nm target, which is well below the limit $L_{max} \approx 368\,$nm, whereas simulation # 2 is performed with a $L_0 = 375\,$nm target, which is slightly thicker than the limit.

Figure 6.25 shows the simulation results for a $L = 75\,$nm target. Significant acceleration occurs since the shock wave intersects the wave front C^+ characteristic (cf. fig. 6.19) of the slab within the laser pulse duration.

In contrast, fig. 6.26 shows the results for a $L = 375\,$nm target for identical laser parameters. Here the condition given in Eq. 6.50 is violated and thus the compression stops before the shock intersects the back end of the slab. Thus, as shown in fig. 6.26 the acceleration process is incomplete, but an expansion wave leaves the back end while the center of the target remains stationary.

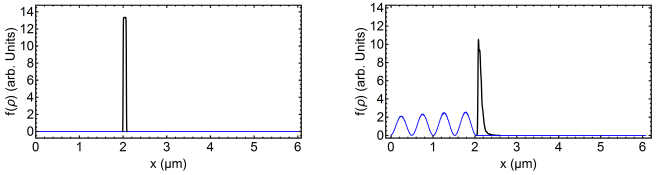

(a) $t = 0\,\mathrm{fs}$. **(b)** $t = 62.5\,\mathrm{fs}$.

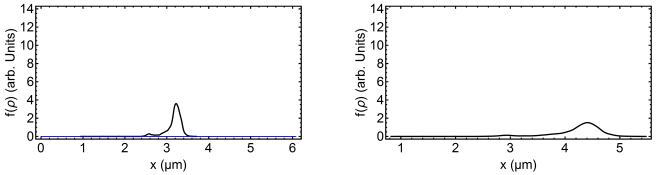

(c) $t = 125\,\mathrm{fs}$. **(d)** $t = 187.5\,\mathrm{fs}$.

Figure 6.25.: Plasma (black) and laser (blue) for $I_L \approx 10^{21}\,\mathrm{W/cm^2}$ and $L_0 = 75\,\mathrm{nm}$. As predicted by Eq. 6.50, a bulk acceleration is achieved.

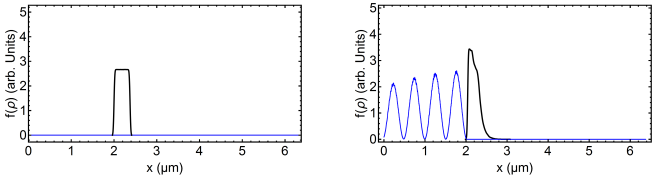

(a) $t = 0\,\mathrm{fs}$. **(b)** $t = 62.5\,\mathrm{fs}$.

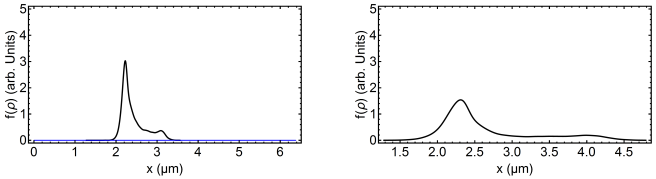

(c) $t = 125\,\mathrm{fs}$. **(d)** $t = 187.5\,\mathrm{fs}$.

Figure 6.26.: Plasma (black) and laser (blue) for $I_L \approx 10^{21}\,\mathrm{W/cm^2}$ and $L_0 = 375\,\mathrm{nm}$ target. As predicted by Eq. 6.50, a rarefaction wave leaves the slab.

6.3.6 Compression and heating at RPA

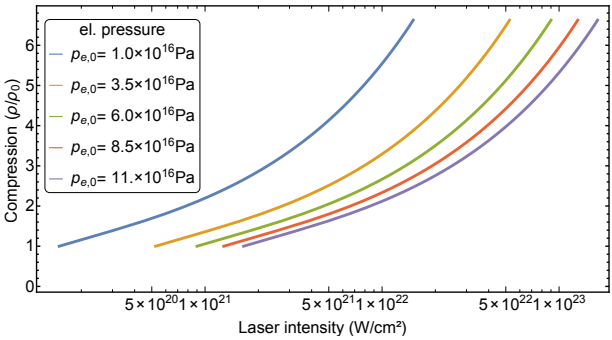

Figure 6.27.: Compression at RPA as a function of the laser intensity for different initial plasma states.

In section 6.2 it is shown that the compression of the plasma is an important parameter for the stability of the radiation pressure acceleration. It is referred to this section to derive an expression for the compression. The plasma between the piston and the shock $x_p \leq x \leq x_s$ attends the piston velocity and from Eq. 6.41 one obtains:

$$p_p = \left(1 + \frac{\varkappa - 1}{2} u_p\right)^{\frac{2\varkappa}{\varkappa - 1}} \tag{6.51}$$

Combining Eqs. 6.29 and 6.51 yields an expression for the compression:

$$\kappa = \frac{\rho}{\rho_0} = \left(1 + \frac{\varkappa - 1}{2} u_p\right)^{\frac{2}{\varkappa - 1}}, \tag{6.52}$$

where the piston velocity u_p is determined by the continuity condition 6.40 and $u_p \gg 1$ is required. Figure 6.27 shows exemplary solutions of Eq. 6.52 for different initial electron pressures.

Given the initial state of the plasma and the laser intensity, from fig. 6.27 one obtains the compression C graphically and determines the lower target width limit L_0 from Eq. 6.12 (cf. section 6.2.2).

7 Radiation pressure acceleration in two dimensions

This chapter presents the two dimensional investigation of the RPA mechanism in the xy-plane. Particular interest is applied to the investigation of the beam transverse divergence and the derivation of a short scaling law for the divergence angle, applying the current flag model (CFM, see chapter 3.3.3). The analysis of the divergence serves as a motivation for the development of an advanced beam transport method for super critical plasma beams. Prior to that the applicability of the one dimensional models (1D models) to the two dimensional (2D) RPA is reviewed.

7.1 Verification of the 1D conditions for 2D RPA

The following sections demonstrate the validity of the previously derived conditions for the two dimensional case. For this purpose, each condition is exemplarily verified with a set of 2D full EM PIC simulations.

7.1.1 Validity of the minimum target thickness in 2D

In this section the validity of the minimum target width obtained in chapter 6.2 is reviewed. According to Eq. 6.7, the lower limit for the target thickness is:

$$L_0 \geq \frac{\sqrt{\kappa_e}}{2\pi} \frac{\omega}{\omega_{pe,0}} \lambda, \tag{7.1}$$

where $\kappa_e = n_e/n_{e,0}$ denotes the compression factor of the electrons, that is obtained graphically from fig. 6.27. Equation 7.1 is confirmed by two exemplary 2D PIC simulations. The simulations are performed with the parameters shown in table 7.1. From fig. 6.27 one obtains a compression of $\kappa_e \approx 2$. Given a wavelength of $\lambda = 1\,\mu$m, one obtains from Eq. 7.1 a critical minimum thickness of $L_{cr,min} \approx 6.8\,$nm. To emphasize the significance of Eq. 7.1, target # 1 has a width $L_0 = 2L_{cr,min}$ noticeably larger than the threshold and target # 2 has a width $L_0 = 0.5L_{cr,min}$ well below the threshold.

Figure 7.1 shows the simulation results for the case of $L_0 = 2L_{cr,min}$, satisfying condition 7.1. As predicted by the 1D model, a stable RPA is achieved. In contrast to that, fig. 7.2 shows the case where L_0 is chosen too low and the 1D model predicts

a perforation of the target. After a phase of compression, the laser penetrates the plasma and the entire acceleration process is terminated. Obviously, the highest compression is achieved in the center of the plasma, where the laser intensity has its maximum.

Table 7.1.: Simulation parameters used for validation of minimum target thickness.

Type	Z	$\rho_0(\mathrm{kg/m^3})$	$W_{th,e,0}(\mathrm{keV})$	$I_0(\mathrm{W/cm^2})$	$\tau_L(\mathrm{fs})$	$L_0(\mathrm{nm})$
Ti	22	4500	6.4	$5 \cdot 10^{20}$	100	13.5, 3.4

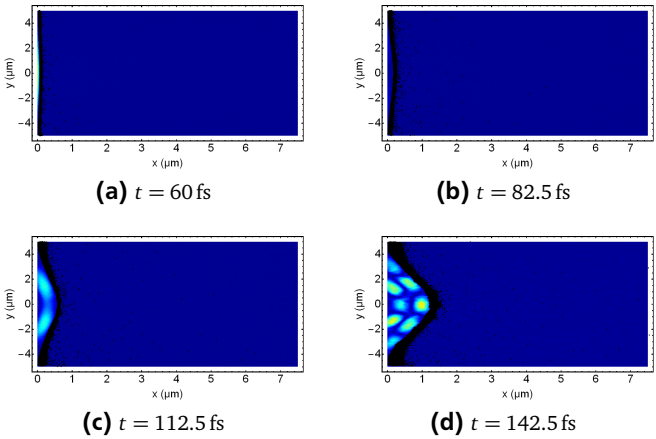

(a) $t = 60\,\mathrm{fs}$ **(b)** $t = 82.5\,\mathrm{fs}$

(c) $t = 112.5\,\mathrm{fs}$ **(d)** $t = 142.5\,\mathrm{fs}$

Figure 7.1.: Electron distribution (black dots) and electric field (color) as function of x and y for different times in case $L_0 = 2L_{min}$. The laser has a Gaussian envelope with a beam waist of $w_0 = 4\,\mu\mathrm{m}$.

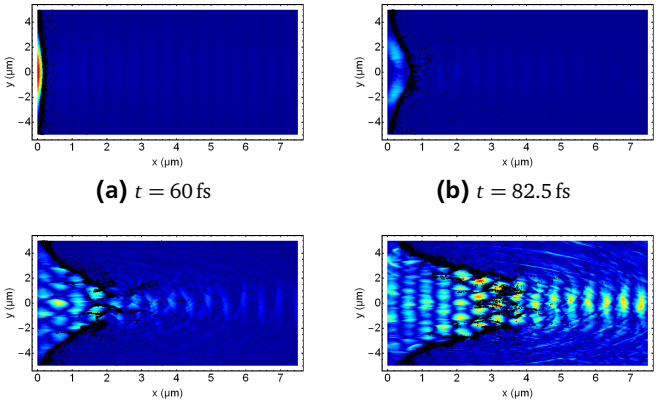

(a) $t = 60\,\mathrm{fs}$ **(b)** $t = 82.5\,\mathrm{fs}$

(c) $t = 112.5\,\mathrm{fs}$ **(d)** $t = 142.5\,\mathrm{fs}$

Figure 7.2.: Electron distribution (black dots) and electric field (color) as function of x and y for different times in case $L_0 = 0.5L_{min}$. The laser has a Gaussian envelope with a beam waist of $w_0 = 4\,\mu\mathrm{m}$.

7.1.2 Validity of the intensity threshold

Table 7.2.: Simulation parameters used for validation of minimum laser intensity.

Type	Z	ρ_0(kg/m^3)	$W_{th,e,0}$(keV)	I_0($\times 10^{20}$ W/cm^2)	τ_L(fs)	L_0(nm)
Ti	22	4500	6.4	1, 5	100	25

This section demonstrates the validity of the lower intensity limit (cf. chapter 6.3) for the 2D RPA. From Eqs. 6.40 and 6.41 one obtains:

$$\begin{aligned} I &\geq \frac{1}{2} c n_{e,0} k_B T_{e,0} \left(\varkappa p_p^{1/\varkappa} u_p u_p + p_p \right), \quad u_{p,cr} = 1 \\ p_p &= \left(1 + \frac{\varkappa - 1}{2} u_p \right)^{\frac{2\varkappa}{\varkappa - 1}} \end{aligned} \quad , \tag{7.2}$$

where $p_{e,0} = n_{e,0} k_B T_{e,0}$ and $\varkappa = 5/3$, holds. Equation 7.2 is reviewed with a series of 2D full EM PIC simulations. The corresponding parameters are listed in table 7.2[1]. From Eq. 7.2 one calculates a lower intensity limit of $I_{cr} \approx 1.33 \cdot 10^{20}\,\mathrm{W/cm^2}$, hence the first simulation is below this limit.

Figure 7.3a shows the ion distribution for a laser peak intensity of $I_{L,1} < I_{cr}$: Since Eq. 7.2 is violated, no shock acceleration is achieved. Instead, a rarefaction wave forms and causes an expansion of the plasma. From fig. 7.3b one obtains the ion distribution for a typical 2D RPA, with a laser peak intensity is $I_{L,2} > I_{cr}$. In the plasma center Eq. 7.2 is met and an ideal light sail is achieved.

Figures 7.4a-7.4b show the corresponding energy distribution, along a straight line at $y = 0$: For $I < I_{cr}$, an exponentially decaying spectrum is realized (see fig. 7.4a). The present experimental results quoted in the introduction strongly deviate from the predicted peak spectra, visible in fig. 1.3. The similarity of fig. 7.4 and 1.3 indicates that required laser intensity is not yet met, justified by the fact that both spectra 7.4 and 1.3 are located in the same energy range of a few MeV.

A major advantage of the light sail regime is the energy scaling $W_{kin} \propto I^2$, compared to TNSA which scales with $W_{kin} \propto I^{1/2}$, with W_{kin} being the average kinetic energy of the ions. However, this energy scaling requires a light sail to be realized and thus $I > I_{cr}$.

[1] For details on the evaluation of the electron temperature, see appendix C.3.

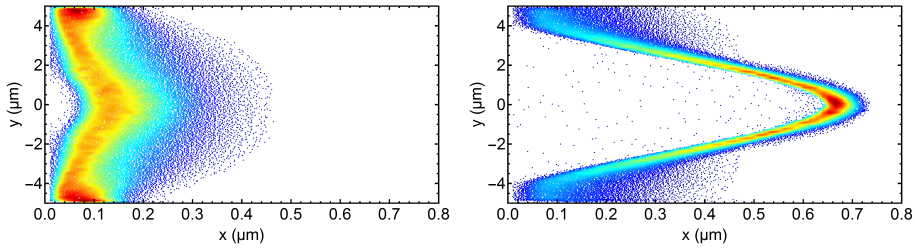

(a) $I = 1 \cdot 10^{20}\,\mathrm{W/cm^2}$ **(b)** $I = 5 \cdot 10^{20}\,\mathrm{W/cm^2}$

Figure 7.3.: Ion density (colored dots) as function of x and y after the acceleration process for different laser intensities.

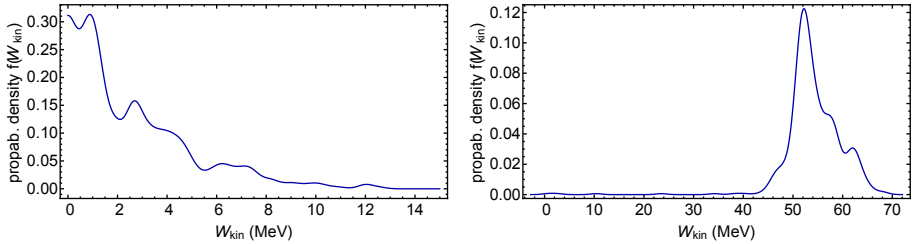

(a) Energy distribution for $I = 1 \cdot 10^{20}\,\mathrm{W/cm^2}$. **(b)** Energy distribution for $I = 5 \cdot 10^{20}\,\mathrm{W/cm^2}$.

Figure 7.4.: Spatial and energy distribution after the acceleration process for the cases $I < I_{cr}$ (left side) and $I > I_{cr}$ (right side).

Comparing fig. 7.4a and 7.4b one obtains: If the critical intensity I_{cr} is exceeded, the energy scaling switches from $W_{kin} \propto I^{1/2}$ to $W_{kin} \propto I^2$ and thus energies more than one order of magnitude higher are achieved. From fig. 7.3b it is evident, that a light sail is only realized at the plasma center, whereas the outer wings form a rarefaction wave. The explanation is represented in fig. 7.5: Due to the Gaussian envelope of the laser $I(y) = I_0 \exp(-y^2/\sigma^2)$, the intensity transversely decreases below the threshold value $I_{cr} \approx 1.33 \cdot 10^{20}\,\mathrm{W/cm^2}$ (see fig. 7.5) after an offset of $y \approx 3.3\,\mu\mathrm{m}$ and thus a light sail acceleration is only possible in the center part $|y| < 3.3\,\mu\mathrm{m}$.

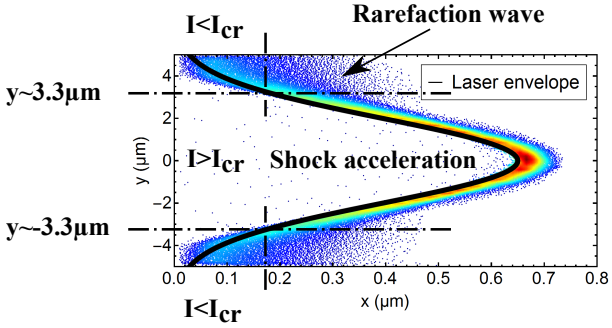

Figure 7.5.: Ion density (colored dots) and laser intensity (black line): In the center region $|y| < 3.3\,\mu$m (dotted lines), $I > I_{cr}$ holds and thus a light sail is realized. For $|y| > 3.3\,\mu$m the intensity drops below the critical limit, $I < I_{cr}$ and thus no RPA is achieved. Instead a rarefaction wave expands.

7.1.3 Validity of the target thickness threshold for 2D

The validity of the upper limit for the target width remains to be demonstrated. Similar to the previous section, two example simulations are compared with the analytic results. Table 7.3 contains the simulation parameters.

Given the parameters in tab. 7.3, from Eq. 6.50 one obtains a permissible target thickness of $L \approx 25\,$nm.

Figure 7.6 shows the results of the simulation. In agreement with the analytic theory, a strong compression wave is realized for the narrow target with $L = 0.5 L_{max}$, whereas a rarefaction wave is achieved for the thick target $L = 2 L_{max}$.

Table 7.3.: Simulation parameters for validation of upper limit of target width.

Type	Z	ρ_0(kg/m^3)	$W_{th,e,0}$(keV)	I_0(W/cm^2)	τ_L(fs)	L_0/L_{max}
Ti	22	4500	6.4	$1 \cdot 10^{22}$	100	0.5, 2

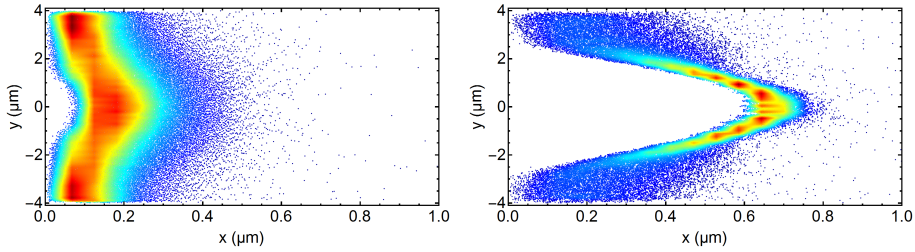

(a) $L = 2L_{max}$. **(b)** $L = 0.5L_{max}$.

Figure 7.6.: Density distribution (color) for different initial target widths.

7.1.4 Conclusion on the applicability of the 1D models to 2D RPA

The applicability conditions $\sqrt{\kappa_e}\omega\lambda/(2\pi\omega_{pe,0}) \leq L \leq (x_p - a_0\tau)/(1-\rho_0/\rho_p)$ (cf. sections 6.2 and 6.3) and $I > I_{cr}$ (cf. section 6.3) derived in 1D has been validated against 2D full EM PIC simulations.

Due to the intensity decrease caused by the spatial profile of the laser a light sail is only realized at the plasma center, whereas the outer wings of the plasma form a rarefaction wave.

A comparison of the plasma's exponentially decaying energy spectrum for $I < I_{cr}$ shows substantial similarity to the energy spectra obtained experimentally and indicates, that the critical laser intensity is not yet achieved in experiment and thus no pure light sail is realized.

7.2 Divergence of the RPA plasma beam

The analysis of the RPA in two dimensions is continued with an investigation of the transverse beam divergence[33] of the emerging plasma.

7.2.1 Derivation of the model and divergence for Gaussian laser

To investigate the transverse divergence of the RPA plasma, the CURRENT FLAG MODEL (see section 3.3.3) is used.

In order to obtain a quasi linear PDE system, Eqs. 3.45 and 3.56 are series expanded up to $\mathcal{O}((\partial_y h)^2)$. Switching to the dimensionless variables $h \to c\tau_L \xi$, $y \to c\tau_L \eta$, $t \to \tau_L \tau$, $u_i \to c\beta_i$ and introduce the dimensionless acceleration parameter $A_0^2 = (1+R) I_0 \tau_L / \rho L c^2$, the kinematic boundary condition and the equations of motions are:

$$\begin{aligned} &\partial_\tau \xi + \beta_y \partial_\eta \xi - \beta_x = 0 \\ &\partial_\tau \beta_x + \beta_y \partial_\eta \beta_x - A_0^2 g(\eta,\tau) = 0 \\ &\partial_\tau \beta_y + \beta_y \partial_\eta \beta_y - A_0^2 g(\eta,\tau) \partial_\eta \xi = 0 \end{aligned} \quad , \tag{7.3}$$

where $g = g(\eta,\tau)$ is a laser profil at the vacuum plasma interface $\xi = \xi(\eta,\tau)$. Given the state vector $Z = (\xi, \beta_x, \beta_y)^T$, the state form of Eqs. 7.3 yields:

$$\begin{aligned} &\partial_\tau Z + S \partial_\eta Z + b = \\ &\frac{\partial}{\partial \tau} \begin{pmatrix} \xi \\ \beta_x \\ \beta_y \end{pmatrix} + \begin{pmatrix} \beta_y & 0 & 0 \\ 0 & \beta_y & 0 \\ -A^2 g & 0 & \beta_y \end{pmatrix} \frac{\partial}{\partial \eta} \begin{pmatrix} \xi \\ \beta_x \\ \beta_y \end{pmatrix} + \begin{pmatrix} -\beta_x \\ -A^2 g \\ 0 \end{pmatrix} = \begin{pmatrix} 0 \\ 0 \\ 0 \end{pmatrix}, \end{aligned} \tag{7.4}$$

with S being the system matrix. The solution of Eqs. 7.4 is obtained by applying RIEMANN'S INTEGRATION TECHNIQUE, similar to the procedure presented in chapter 6.3. The eigenvalues of the system matrix are $\lambda_{1,2,3} = \beta_y$ and the corresponding left hand side eigenvectors are $L_1 = (1,0,0)^T$, $L_2 = (0,1,0)^T$ and $L_3 = (0,0,0)^T$. Unfortunately, this system is not strictly hyperbolic. However, since the first and second equation in 7.4 are already in conservation form with their characteristics $C : d_\tau \eta = \beta_y$, this system can regardless be solved. Rewriting Eqs. 7.4 as a system of ordinary differential equations one obtains:

$$\begin{aligned} &d_\tau \xi - \beta_x = 0, \qquad C : \; d_\tau \eta = \beta_y \\ &d_\tau \beta_x - A_0^2 g(\eta,\tau) = 0, \quad C : \; d_\tau \eta = \beta_y \\ &d_\tau \beta_y - A_0^2 g(\eta,\tau) \partial_\eta \xi = 0, \quad C : \; d_\tau \eta = \beta_y \end{aligned} \tag{7.5}$$

The first and second equation are coupled and independent from the third. Therefore one successively solves the second equation, the first one and with those results finally the third. Although this system is not strictly hyperbolic, fortunately all equations are transported on the same characteristic curve $C : \partial_\tau \eta = {\beta_y}^2$. The laser function reads: $g(\eta,\tau) = 4\tau^2 \exp(-a^2\eta^2)\exp(-4\tau^2+1)^3$, with $a^2 = c^2\tau_L^2/2\sigma^2$ and σ being the standard deviation of the laser envelope. Then the solution of the first and second equation is:

$$\begin{aligned} \xi &= \frac{A_0^2}{8} \mathrm{e}^{-a^2\eta^2+1}(\mathrm{e}^{-4\tau^2} + \sqrt{\pi}\tau \mathrm{Erf}(2\tau) - 1), \quad C: \ d_\tau \eta = \beta_y \\ \beta_x &= \frac{A_0^2}{8} \mathrm{e}^{-a^2\eta^2+1}(-4\tau \mathrm{e}^{-4\tau^2} + \sqrt{\pi}\mathrm{Erf}(2\tau)), \quad C: \ d_\tau \eta = \beta_y \end{aligned} \tag{7.6}$$

See Appendix for full derivation. Integrating the last of Eqs. 7.5 one obtains:

$$\beta_y = \int A_0^2 g(\eta,\tau)\partial_\eta \xi d\tau \tag{7.7}$$

The divergence angle of the RPA plasma severely depends on time τ and on the transverse coordinate η. To define a particular divergence angle it is thus acceptable to consider the final divergence angle at the inflection point:

$$\begin{aligned} \vartheta\big|_{\eta=\pm 1/\sqrt{2}a} &= \lim_{\tau\to\infty} \arctan\left(\frac{\beta_y}{\beta_x}\right) = \arctan\left(\frac{(4\sqrt{2}-7)\sqrt{\mathrm{e}}A_0^2 a}{32}\right) \\ \Rightarrow \vartheta &\approx \arctan\left(0.07 a A_0^2\right) \end{aligned} \tag{7.8}$$

With the above definitions, the average divergence angle is:

$$\vartheta \approx \arctan\left(\frac{0.1 I_0 \tau_L^2}{\rho L c \sigma}\right) \tag{7.9}$$

From Eq. 7.9 one notes that larger laser spot sizes σ result in less divergent plasma beams, while a stronger acceleration $I_0/\rho L$ is connected with a larger divergence. Additionally, longer laser pulses cause larger divergence. According to [65] (see also chapter 6), longer laser pulses result in less energy spread compared

[2] This is one of the rare cases, where Riemann's integration can be applied to a non-strictly-hyperbolic system.

[3] For details see section 6.2.

to shorter ones. Concerning the 2D/3D RPA, one therefore has to balance between energy spread and divergence via adjusting the laser pulse duration. Given that the average thermal velocity in terms of c is $\bar{\beta}_{th} = \sqrt{2W_{th}/m_i c^2}$, the divergence angle, as well as the kinetic energy including thermal corrections yield:

$$\begin{aligned} \vartheta &= \arctan\left(\frac{\beta_y + \bar{\beta}_{th}}{\beta_x - \bar{\beta}_{th}}\right) \\ \frac{W_{kin}}{m_i c^2} &= \frac{1}{\sqrt{1-(\beta_x - \bar{\beta}_{th})^2 - (\beta_y + \bar{\beta}_{th})^2}} - 1 \end{aligned} \tag{7.10}$$

Consistently with the general modus of operandi, Eqs. 7.9 and 7.10 are reviewed with a set of 2D full EM PIC simulations, given the parameters listed in tab. 7.4.

Table 7.4.: Simulation parameters for evaluation of the divergence angle.

I_L ($\times 10^{20}$ W/cm^2)	1	5	10	20	w_0 (μm)	4	6	8
A_0	0.14	0.31	0.44	0.63	a	10.6	7.1	5.3

In all cases, the laser pulse duration is $\tau_L = 100$ fs and the target is a standard $L_0 = 25$ nm titanium target. Figure 7.7 shows the divergence angle distribution as a function of the kinetic energy $\vartheta = \vartheta(W_{kin})$ obtained from the simulations with $w_0 = 4\,\mu$m in comparison with the results from Eqs. 7.8 and Eqs. 7.10. An approximate estimation of the expected divergence angle is obtained from Eq. 7.8, whereas Eq. 7.10 represents the envelope of the angle distribution. The plasma temperature is not accessible by the CFM and thus fitted.

Figure 7.8 shows a comparison of Eq. 7.8 with the results of the simulations[4]. Good agreement is achieved for $A_0 \approx 0.25-0.45$, while the results severely deviate from each other for lower A_0 and slightly differ for higher A_0. For lower acceleration parameters A_0, no light sail is achieved (cf. fig. 7.3) and the requirements for the CF model are not met.

Despite from the fact, that the current flag model is only valid when an ideal light sail is achieved, Eq. 7.8 yields a good approximation for the expected divergence angle of the RPA plasma. For typical laser and target parameters the predicted divergence angle $\vartheta \approx 5-20°$ is comparable with the divergence achieved in TNSA experiments.

[4] For details on the evaluation of the simulation results, see appendix B.5.

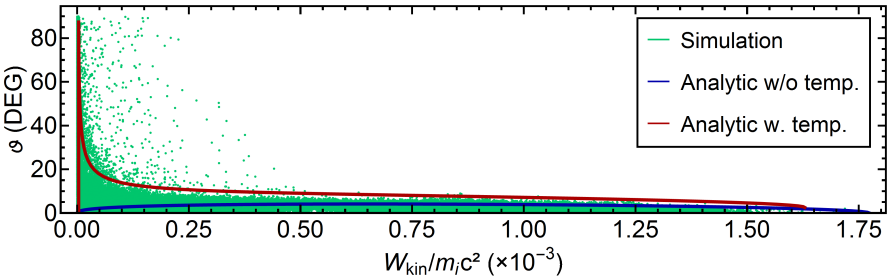

(a) $I = 5 \cdot 10^{20}\,\mathrm{W/cm^2}$

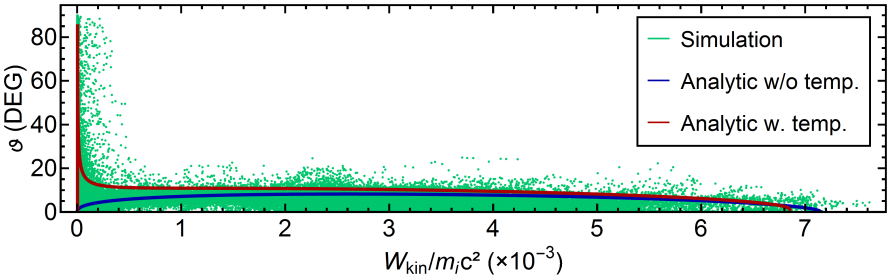

(b) $I = 1 \cdot 10^{21}\,\mathrm{W/cm^2}$

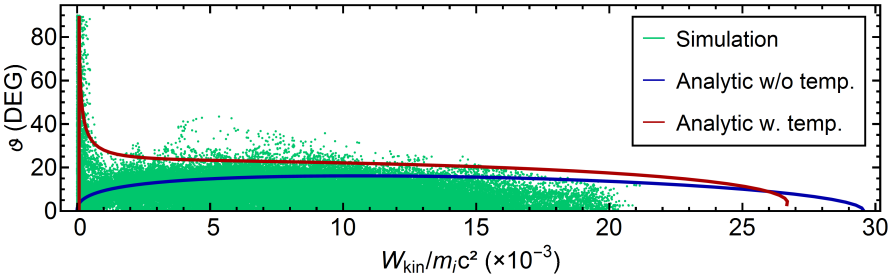

(c) $I = 2 \cdot 10^{21}\,\mathrm{W/cm^2}$

Figure 7.7.: Divergence angle as a function of the kinetic energy $\vartheta = \vartheta(W_{kin})$ from simulation (blue dots), from Eq. 7.8 (black line) and from Eq. 7.10 (red line).

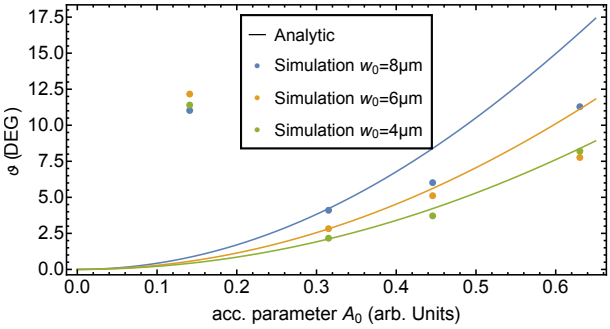

Figure 7.8.: Divergence angle ϑ_{max} as a function of the acceleration parameter A_0, derived from Eq. 7.8 (colored lines) and from simulation (colored dots), for different beam waists w_0.

7.2.2 Divergence for different laser profiles

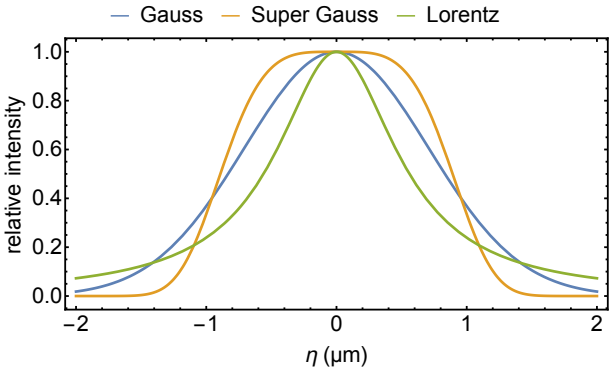

Figure 7.9.: Laser focus shapes: Compared are a Gaussian, 4^{th} order Gaussian and a Lorentz function.

Given that the divergence angle severely depends on the intensity profile, the analysis is extended to arbitrary intensity profiles. A derivation similar to the previous section is performed for an arbitrary[5], analytic[6] function $f(\eta, \tau)$ with

[5] For details on the derivation and the requirements, see appendix B.5

[6] Thus $f(\eta, \tau)$ has to be continuously differentiable.

$f : \mathbb{R} \times \mathbb{R}_0^+ \rightarrow \Omega \subset \mathbb{R}$ and $\Omega = [0,1]$. Furthermore, $f(\eta,\tau)$ satisfies the initial conditions $f(\eta,0) = 0$ and $\partial_\tau f(\eta,0) = 0$ for a consistent solution.

Exemplarily, the Gaussian laser profile is compared with a more narrow 4^{th} order Super Gaussian profile $f(\eta) = \exp(-b^4\eta^4)$ and a spacious Lorentz function $h(\eta) = 1/(1+\eta^2/c^2)$. Carrying out the same derivation as in the previous section, one obtains:

$$\begin{aligned} \vartheta &\approx \arctan(0.046 a A_0^2) \quad \text{for fourth order Gaussian} \\ \vartheta &\approx \arctan(0.072 a A_0^2) \quad \text{for Lorentz function} \end{aligned} \tag{7.11}$$

The corresponding parameters are given in the table 7.5 below.

While the general composition of the divergence scaling is the same for different focal spots, the geometrical pre-factor decreases for a flat top laser spot, resulting in a smaller divergence angle of the plasma beam. Given a temporal profile $k(\tau) = 4\tau^2\exp(-4\tau^2+1)$ and a continuously differentiable spatial profile $q(\eta)$, a general expression for the divergence angle is:

$$\vartheta = \arctan\left(\frac{(7\sqrt{2}-8)e}{64} A_0^2 \frac{dq(\eta)}{d\eta}\bigg|_{\eta=\pm\eta_{ip}/2} \right), \tag{7.12}$$

where η_{ip} is the position of the inflection point of the function $q(\eta)$. For the full derivation, see appendix B.5. The particular function $q(\eta)$ to approximate the laser spot e.g. depends on the optics used in an experiment.

Figure 7.10 shows the divergence angle distribution as a function of the ion kinetic energy $\vartheta = \vartheta(W_{kin})$ for the forth order Gaussian and the Lorentz function, respectively. The analytical model shows good agreement with the simulation results.

Table 7.5.: Parameters for different laser envelopes.

Spot Function	Spot Parameter	$\eta_{inf\,Point}$
Gaussian	a	$0.69/a$
4^{th}-order Gaussian	$b \approx 1.023a$	$0.89/a$
Lorentz	$c \approx 0.56/a$	$0.56/a$

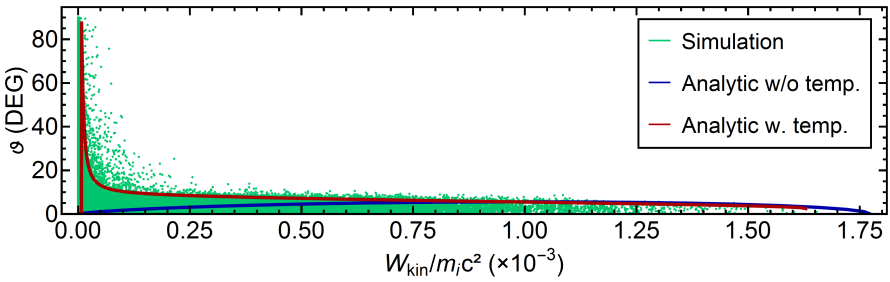

(a) Lorentz profile.

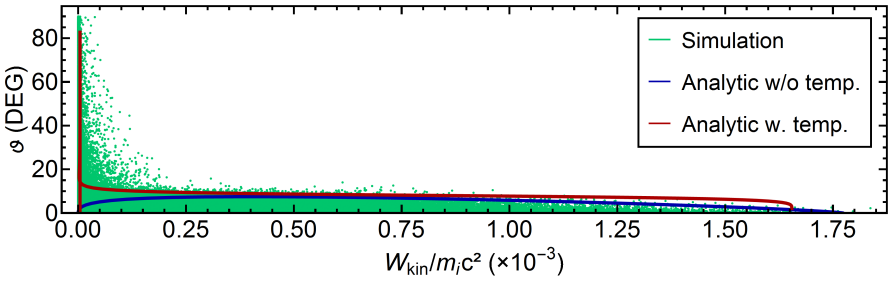

(b) 4^{th} order Gauss profile.

Figure 7.10.: $\vartheta = \vartheta(W_{kin})$ from simulation and from analytic models for a Lorentz and 4^{th} order Gaussian laser focus.

7.2.3 Discussion of the model and applicability

The chapter is finalized by a brief evaluation of the applicability of the CFM.

The CFM is a surface model similar to water surface waves and provides a rough estimate for the transverse divergence of a RPA plasma in form of simple scaling laws. A comparison with 2D full EM PIC simulations proofs the validity of the CF model. In particular, the CF model reproduces the expected kinetic energy and angle distribution confirming the model. However, the CFM requires $\mu = \rho L = const.$ and $\Delta W_{kin} \ll \bar{W}_{kin}$ to be satisfied and has thus a limited range of validity. For the derivation of the divergence angle, the CFM is power series expanded up to $\mathcal{O}((\partial_y h)^2)$ to create a quasi-linear system and facilitate the mathematical treatment. However, the non-linear terms of type $(1+(\partial_y h)^2)^{-1/2}$ limit the slope of the surface in case of large $\partial_y h$:

$$\text{For } \partial_y h \gg 1: \quad \frac{1}{\sqrt{1+(\partial_y h)^2}} \approx \frac{1}{\left|\partial_y h\right|}, \quad \frac{\partial_y h}{\sqrt{1+(\partial_y h)^2}} \approx 1 \tag{7.13}$$

In that case, the linearized model overestimates the divergence angle. Additional information to the CFM are presented in appendix B.5. Most importantly, the predicted divergence is $\vartheta \approx 5^\circ - 20^\circ$ and was previously underestimated. Therefore an application based beam line would need transport elements to cure the divergence and prevent too high particle loss. This motivates the development of a new, non-traditional transport method for super critical plasma beams and is subject to the next chapter.

8 Advanced transport

This chapter presents a concept study for a new transport method[73] for highly over-dense plasma beams: The laser induced focusing[73]. The results obtained in chapter 7 indicate that the divergence angle of the emerging RPA plasma was underestimated formerly. Depending on the laser focal shape, intensity and pulse duration, the divergence angle of the plasma can raise up to $5° - 25°$*. Generally, an experimental setup has dimensions of meters, with a beam pipe diameter of usually a few centimeters, whereas the RPA occurs at distances of a few micro meters. Therefore an experimental setup requires elements to transport and manipulate the emerging plasma beam within a few micrometers from the initial target. However, traditional focusing devices such as magnetic solenoids are not sufficient for high intense plasma beams, as they are generated by the RPA: An inhomogeneous magnetic field will mirror the plasma electrons and the remaining ions would be expelled by the Coulomb explosion. On the other hand, traditional transport devices have dimensions of centimeters and are thus too bulky to be placed immediately after the target. Therefore a non-traditional transport method is presented, which uses a laser beam, rather than solid parts. All results presented in this chapter have been published by the author in [73].*

8.1 Laser induced focusing with a plane laser

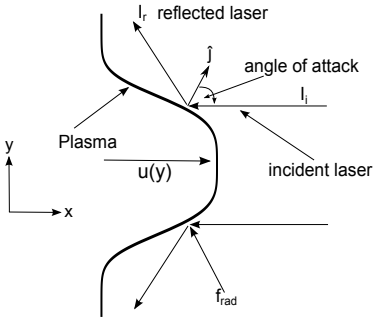

Figure 8.1.: Mechanism of the laser induced focusing: A counter propagating, plane laser pulse hits an over-dense plasma and is reflected. The resulting radiation pressure acts normal to the plasma surface.

In this chapter, an idealized representation of an RPA plasma (compare to [31]) with preset ab initio conditions is applied. In accordance with the results from chapter 7, the plasma is assumed to be a layered, quasi neutral, ion electron mix of thickness L with a given drift velocity $\vec{u} = \vec{u}(\vec{x}, t = 0)$. In addition, the plasma is over-dense to the laser and satisfies the condition $\sqrt{\kappa_e}/2\pi\omega/\omega_{pe}\lambda < L < (x_p - a_0\tau)/(1-\rho_0/\rho_p)$ (cf. chapters 6.2 and 6.3). In order to prevent the plasma from being thermally rarefied, $f k_B T_e/2 \ll (\gamma_e - 1)m_e c^2$ or $T_e \ll 2(\gamma_e - 1)m_e c^2/(f k_B) \propto 10^9\,\mathrm{K}$ is assumed. According to the results obtained in chapter 6.2, the reflective index can be assumed to equal one under these conditions: $R \approx 1$.

Figure 8.1 shows the basic setup for the laser induced focusing: The plasma slice drifts from the left to the right, while a counter propagating, plane laser wave propagates from right to left. The laser is circularly polarized (CP) plane wave with infinite pulse duration $\tau_L \in [0, \infty)$. Since the plasma is over-dense, the laser wave cannot enter the plasma and is reflected at the vacuum plasma interface, see fig. 8.1. Then the radiation pressure of the laser acts normal to the plasma surface, as depicted in fig. 8.1. Therefore one might also call this mechanism RADIATION PRESSURE INDUCED FOCUSING. With reference to the coordinate system in fig. 8.1, the laser pressure force can be subdivided into two parts:

A fraction of the pressure force counteracts the propagation of the plasma and is identified as stopping power. The other fraction of the radiation pressure force compresses the plasma film towards the center axis, decreasing the average film diameter and is thus identified as focusing power.

Table 8.1.: Parameters for the laser focusing 2D simulations.

Material	Z	$\rho(\mathrm{kg/m^3})$	n_e	$L(\mathrm{nm})$
Titanium	22	4500	$1100 n_c$	25

The investigation of the advanced focusing is initiated with the review of a set of 2D full EM Particle In Cell (PIC) simulations with the parameters listed in table 8.1. The plasma slab has a drift velocity with a fourth order Gaussian distribution (in accordance with the results in [31]):

$$\vec{u}(y, t = 0) = u_0 e^{-y^4/\sigma_y^4} \left(\vec{e}_x + 1/2(y/\sigma_y)^3 \vec{e}_y\right) \tag{8.1}$$

Where $u_0 = 0.5c$ and $\sigma_y \approx 2\,\mu\mathrm{m}$. A circularly polarized laser with a wavelength of $\lambda = 1\,\mu\mathrm{m}$ and an intensity of $I_0 \approx 1.9 \cdot 10^{20}\,\mathrm{W/cm^2}$ is used for the focusing.

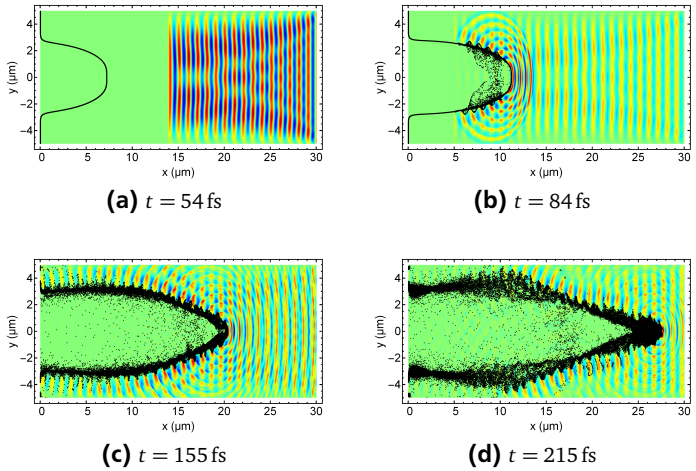

Figure 8.2.: Electrons (black dots) and electric field (colored) from the 2D PIC simulation at different times.

With these parameters, $\sigma_y > \lambda$ holds in particular. The focusing mechanism also works for much lower laser intensities, resulting in longer focal lengths. However, computational resources are saved by examining the case of a strong laser with a short focal length, to keep the simulation domain small.

Figure 8.2 shows the electron distribution, as well as the electrical field E_z for different times: Clearly visible is the reflection of the laser at the vacuum plasma interface and the resulting focusing of the plasma film, visible as a particle concentration at the front center and the cone shape of the distribution. Besides of the focusing, the laser excites electron waves on the plasma surface. These electron waves in turn lead to local charge separation and the subsequent Coulomb explosion expels a fraction of the ions.

The electron and ion distribution is depicted in fig. 8.3 for different stages of the laser induced focusing. Clearly visible is the Coulomb explosion the resulting ejection of a part of the ions. For the implementation of the laser induced focusing (LIF) it is important to define a focal length, as for any traditional focusing method. However, in contrast to conventional focusing devices (e.g. solenoids, thin lenses), it is difficult to define an exclusive focal length, since the LIF method is only slightly energy selective, rather then severely dependent on the particular shape of the plasma film. Moreover, the plasma emerging during the RPA is neither a spatially

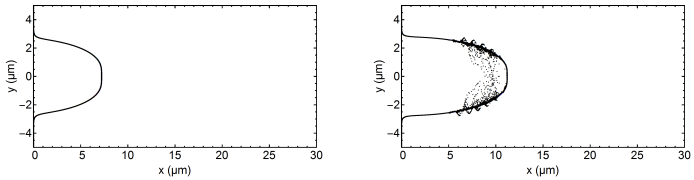

(a) $t = 54\,\mathrm{fs}$ **(b)** $t = 84\,\mathrm{fs}$

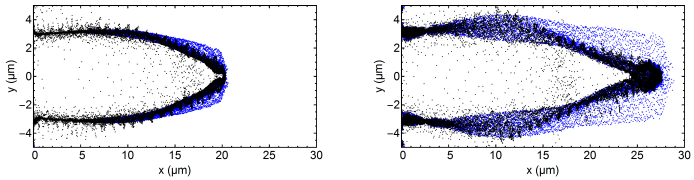

(c) $t = 155\,\mathrm{fs}$ **(d)** $t = 215\,\mathrm{fs}$

Figure 8.3.: Electrons (black dots) ions (blue dots) at different times. Clearly visible is the Coulomb explosion and resulting expelling of the ions.

localized nor a bounded bunch, rather than a spatially extended distribution, as visible in fig. 8.2 or 8.3. It is more constructive to evaluate certain quality factors of the focused beam. Subsequent, the propagation distance of the fastest ions x_f is identified with flight distance or front of the plasma.

The average beam radius as a function of the flight distance $\bar{r} = \bar{r}(x_f)$ is shown in fig. 8.4: After $x_f \approx 17\,\mu\mathrm{m}$, the laser induced pressure forces have completely compensated the transverse drift. Compared to the free drift case, the final beam radius of the laser focused plasma is ≈ 1.5 times smaller after a flight distances of $x_f \approx 30\,\mu\mathrm{m}$ and the average beam radius saturates, as evident from the vanishing slope in fig. 8.4.

A fundamental idea of any focusing is the spatial concentration of energy. The kinetic energy density distribution function is $f_k = f_k(\varpi_{kin,k}, y)$ with $f_k : \mathbb{R}_0^+ \times \mathbb{R} \to [0,1]$, for the electrons ($k = e$) and ions ($k = i$). Figure 8.5 shows the electron and ion density distribution for different times: After an expansion stage (fig. 8.5a and 8.5b) the ion energy is concentrated at the center (see fig. 8.5c, $y = 0$) with a slightly lower kinetic energy (from $W_{kin}/m_i c^2 \approx 0.12$ to $W_{kin}/m_i c^2 \approx 0.09$). The electron waves, excited on the plasma surface, cause an increase of the electron thermal energy, visible in fig. 8.5e to 8.5h. as an increase of the phase space volume of the electrons accompanied with a stretching of the abscissae. This reveals

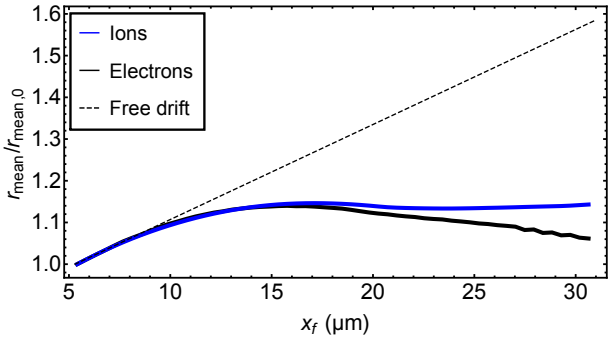

Figure 8.4.: Average beam radius as a function of the flight distance x_f for focusing with a plane laser. For $x_f < 10\,\mu$m, the beam drifts. After a flight distance $x_f \approx 27\,\mu$m the minimum beam radius $r \approx 0.4 r_0$ is achieved.

another important difference to traditional, magnetic focusing: Magnetic focusing devices rotate and reshape the phase space volume, but its quantity remains unchanged, whereas the LIF performs work on the plasma and the particles energy is not necessarily conserved.

To quantify the magnitude of the energy concentration, the amount of energy inclosed in a certain region $\Omega := [0, \infty) \cup [-\varepsilon, \varepsilon]$ of the phase space is evaluated:

$$W_{kin,k}(\Omega) = \iint_{\Omega} f_k(\varpi_{kin,k}, y) d\Omega = \int_0^{\infty} \int_{-\varepsilon}^{\varepsilon} f_k(\varpi_{kin,k}, y) dy\, de_{kin,k} \tag{8.2}$$

The kinetic energy of the electrons and ions in the transverse plane $|y| < 0.25\,\mu$m as a function of the flight distance x_f, is depicted in fig. 8.6: Due to the initial divergent drift of the plasma, the amount of energy in the center region attenuates ($0 \leq x_f \leq 12\,\mu$m); The laser induced focusing then counteracts the drift and by that increases the amount of energy in the plasma center ($x_f > 12\,\mu$m).

The examination of the LIF is expanded to an analytic description of the mechanism by applying the CFM. As the details concerning the validity and derivation of the CF model are presented in chapter 3.3.3, the derivation is abbreviated. The plasma is modeled as a slab of constant thickness L, with constant mass density ρ and a given initial drift velocity $\vec{u} = \vec{u}(y, t = 0)$. The plasma vacuum interface is described by an analytic, bounded function $f(x, y, t) = const$, for which LIOUVILLE'S THEOREM 1 gives the kinematic boundary condition:

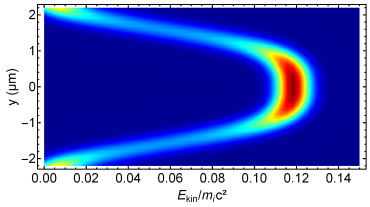

(a) Ion kinetic energy at $t = 54\,\text{fs}$.

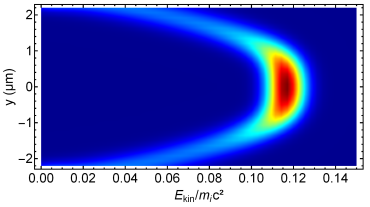

(b) Ion kinetic energy at $t = 84\,\text{fs}$.

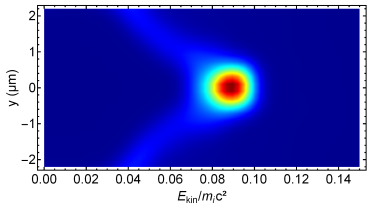

(c) Ion kinetic energy at $t = 155\,\text{fs}$.

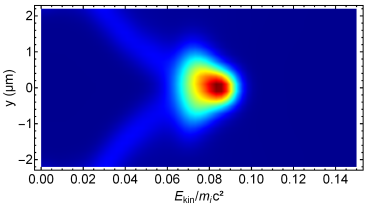

(d) Ion kinetic energy at $t = 215\,\text{fs}$.

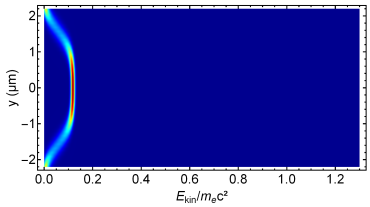

(e) Electron kinetic energy at $t = 54\,\text{fs}$.

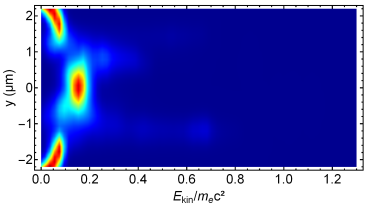

(f) Electron kinetic energy at $t = 84\,\text{fs}$.

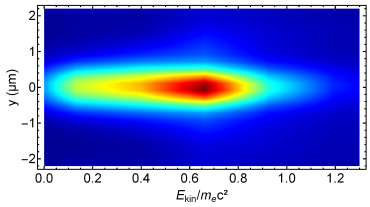

(g) Electron kinetic energy at $t = 155\,\text{fs}$.

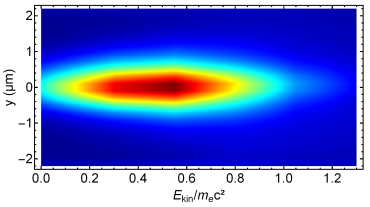

(h) Electron kinetic energy at $t = 215\,\text{fs}$.

Figure 8.5.: Kinetic energy distribution $f_k(\varpi_{kin}, y)$ as a function of the transverse coordinate y, for electrons and ions for different times.

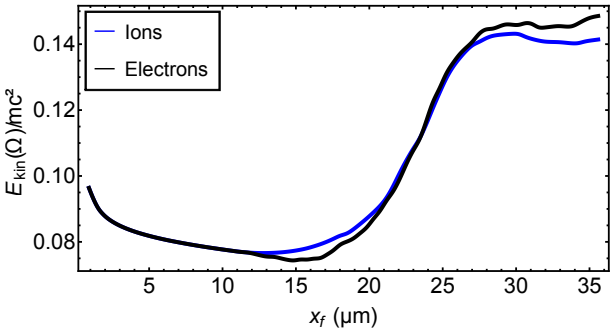

Figure 8.6.: Integrated kinetic energy included in $|y| < 0.25\,\mu\mathrm{m}$ for ions and electrons as a function of the flight distance x_f.

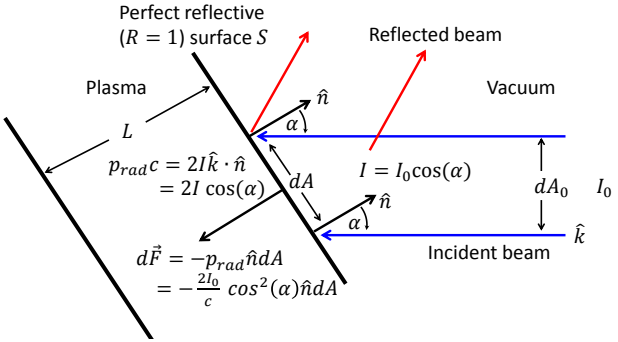

Figure 8.7.: Illustration of the interaction of a laser with an oblique surface: The laser intensity is allocated to the area dA and acts normal to the surface, where the incident and the reflected beam contribute in equal parts.

$$\frac{\partial f}{\partial t} + u\frac{\partial f}{\partial x} + v\frac{\partial f}{\partial y} = 0, \tag{8.3}$$

where $d_t x = u$ and $d_t y = v$ are used. Under the condition of perfect reflectivity $R = 1$, the plasma interacts with the laser only due to the radiation pressure of the laser, creating a force on the interface $f = const$. The corresponding situation is depicted in scheme 8.7: In case of a surface oblique to the incident laser, the energy $I_0 dA_0$ is allocated to the area $\cos(\alpha)dA = dA_0$, where α is the enclosed angle of the interface normal vector $\hat{n}$ and the laser propagation direction $\hat{k}$. By that, the

operative laser intensity yields $I = I_0 \cos(\alpha)$. Consistently with the assumption of perfect reflectivity, the angle between the surface normal and the reflected wave is also α. The incident and the reflected wave both contribute a momentum transfer of $I\cos(\alpha)/c$ normal to surface. The integral momentum balance, as well as the kinematic boundary condition for the interface then yield:

$$\begin{aligned} &\frac{d}{dt}\iint_{\partial V} \rho L \vec{u} dA = -\iint_{\partial V} \frac{2I_0}{c}\cos^2(\alpha)\hat{n} dA \\ &d_t f(x,y,t) = 0, \quad \hat{n} = \nabla f / |\nabla f| \end{aligned} \tag{8.4}$$

With the equivalent representation $f = x - h(y,t) = 0$, the normal vector of the surface is given as $\hat{n} = (1+(\partial_y h)^2)^{-1/2}(1, -\partial_y h)^T$ and the localization of the Eqs. 8.4 reads:

$$\begin{aligned} \rho L \frac{du}{dt} &= -\frac{2I_0}{c}\frac{1}{\sqrt{1+(\partial_y h)^2}}\cos^2(\alpha) \\ \rho L \frac{dv}{dt} &= \frac{2I_0}{c}\frac{\partial_y h}{\sqrt{1+(\partial_y h)^2}}\cos^2(\alpha) \\ \partial_t h + v\partial_y h &= u, \end{aligned} \tag{8.5}$$

where $d_t u_i = \partial_t u_i + v\partial_y u_i$ is the total time derivative of the velocity field (see also chapter 3.3.3). The incident laser wave is plane and propagates into negative x-direction $\hat{k}_i = -\vec{e}_x$. Switching to the dimensionless variables $x = \lambda\xi$, $y = \lambda\eta$, $t = \tau\lambda/c$, $u_0(y) \to c\beta_{x0}(\eta)$, $V_{y0}(y) \to c\beta_{y0}(\eta)$, $u_x = c\beta_\parallel$, $u_y = c\beta_\perp$ and $h(y,t) \to \tilde{h}(\eta,\tau)\lambda$, the angle of incidence is:

$$\cos(\alpha) = -\hat{n}\cdot\vec{e}_x \quad \Longleftrightarrow \quad \cos^2(\alpha) = \frac{1}{1+(\partial_\eta \tilde{h})^2}, \tag{8.6}$$

where λ is the laser wavelength. With the relation 8.6, Eqs. 8.5 in the new variables read:

$$\begin{aligned} \frac{d\beta_\parallel}{d\tau} &= -A_0^2 \frac{1}{\left(1+(\partial_\eta\tilde{h})^2\right)^{3/2}} g(\xi = \tilde{h}, \eta, \tau) \\ \frac{d\beta_\perp}{d\tau} &= A_0^2 \frac{\partial_\eta \tilde{h}}{\left(1+(\partial_\eta\tilde{h})^2\right)^{3/2}} g(\xi = \tilde{h}, \eta, \tau) \\ \partial_\tau \tilde{h} + \beta_\perp \partial_\eta \tilde{h} &= \beta_\parallel, \end{aligned} \tag{8.7}$$

where $A_0^2 = 2\epsilon_0 E_0^2 \lambda / 2\rho_0 c^2 L$ is the dimensionless acceleration parameter. Then $g = g(\xi, \eta, \tau)$ is the profile of the laser intensity. In particular, g is $g = H(\tau - \tau_0)$, where $H(\tau)$ is the Heaviside theta function and τ_0 is the free drift time, before the laser interacts with the plasma. Equations 8.7 reveal an optimum angle of incidence between the surface normal and the wave vector of $\alpha_{opt} = \pi/4$. For smaller angles, the stopping power dominates over the focusing effect ($\alpha \to 0$), for larger angles ($\alpha \to \pi/2$), $\hat{k} \cdot \hat{n} = 0$ and the effect of the laser vanishes. The terms in the denominator of Eqs. 8.7 limit the impact of the laser on the plasmas surface for large slopes $\partial_\eta \tilde{h}$:

$$\begin{aligned} \lim_{\partial_\eta \tilde{h} \to \pm\infty} \frac{1}{\left(1 + (\partial_\eta \tilde{h})^2\right)^{3/2}} &\to 0 \\ \lim_{\partial_\eta \tilde{h} \to \pm\infty} \frac{\partial_\eta \tilde{h}}{\left(1 + (\partial_\eta \tilde{h})^2\right)^{3/2}} &\to 0 \end{aligned} \tag{8.8}$$

Unfortunately, this prohibits a linearization of Eqs. 8.7, since in the linearized case the focusing strength of the method is over-estimated. Therefore equations 8.7 are expanded in ascending powers of $\partial_\eta \tilde{h}$ up to $\mathcal{O}((\partial_\eta \tilde{h})^4)$

$$\begin{aligned} \frac{d\beta_\parallel}{d\tau} &\approx -A_0^2 g \left[1 - \frac{3}{2}\left(\partial_\eta \tilde{h}\right)^2\right] + \mathcal{O}\left(\left(\partial_\eta \tilde{h}\right)^4\right) \\ \frac{d\beta_\perp}{d\tau} &\approx A_0^2 g \left[\partial_\eta \tilde{h} - \frac{3}{2}\left(\partial_\eta \tilde{h}\right)^3\right] + \mathcal{O}\left(\left(\partial_\eta \tilde{h}\right)^4\right) \\ \partial_\tau \tilde{h} + \beta_\perp \partial_\eta \tilde{h} &= \beta_\parallel, \end{aligned} \tag{8.9}$$

and subsequently solved numerically. From Eqs. 8.9 one obtains, that the laser focusing is a strongly non-linear feature which severely depends on the plasma slope $\partial_\eta \tilde{h}$.

Figure 8.8 shows a numerical solution of Eq. 8.7 in comparison with the simulation results. While the analytic result gives a rough estimate of the achievable beam diameter, it over-estimates the overall focusing strength. This deviation of the analytical model and the numerical results may be traced back to the fact that the CFM is too simplistic and the requirements to be satisfied for its application are not met anymore while the laser focusing.

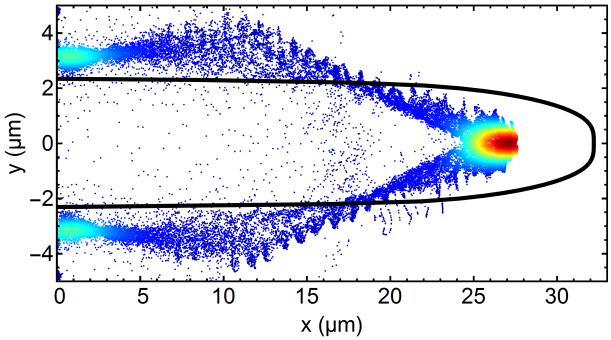

Figure 8.8.: Comparison of the numerical solution of Eq. 8.7 (black line) with the result of a 2D PIC simulation (color).

8.2 Laser induced focusing with an oblique laser

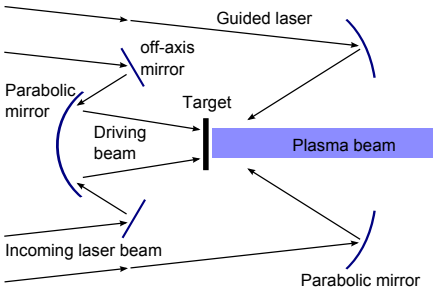

Figure 8.9.: Possible setup for the focusing with an oblique laser: The outer part of the RPA driving laser is guided to parabolic mirrors, focusing the laser onto the plasma film surface. The center part of the laser drives the RPA.

To optimize the efficiency of the laser focusing, one may consider the setup shown in fig. 8.9: The focusing structure gets closer to its optimum working angle of $\alpha_{opt} = \pi/4$ if the laser is emitted at an angle ϑ. With the setup suggested in fig. 8.9, part of the driving laser pulse is used for focusing. The upper and lower wave vectors are then $\hat{k}_u = (-\cos(\vartheta), -\sin(\vartheta))^T$ and $\hat{k}_l = (-\cos(\vartheta), \sin(\vartheta))^T$, respectively.

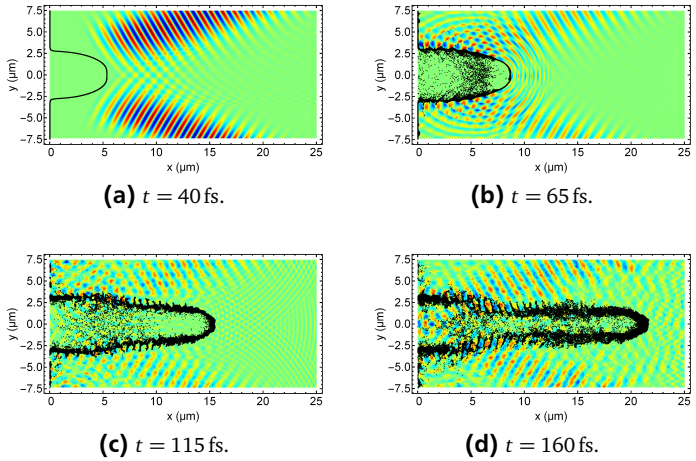

(a) $t = 40\,\mathrm{fs}$. **(b)** $t = 65\,\mathrm{fs}$.

(c) $t = 115\,\mathrm{fs}$. **(d)** $t = 160\,\mathrm{fs}$.

Figure 8.10.: Electron distribution (black dots) and electric field (color) for different time instants. After focusing, a quasi straight beam is achieved.

The analysis of the laser induced focusing with an oblique laser starts with the evaluation of 2D full EM PIC simulation results.

Figure 8.10 shows the electron distribution and the laser wave for several time instants. After the focusing process, the plasma has transformed into a (nearly) perfectly directed beam with almost no divergence. Similar to the case of a plane laser wave, electron waves are excited on the plasma surface.

In order to provide an insight into the effect of local space charge, caused by the electron waves, fig. 8.11a shows the ion and electron distributions for different times. Similar to the plane wave scenario, a part of the ions is expelled due to the Coulomb explosion caused by local space charge.

To assess the focusing efficiency, fig. 8.12 shows the average beam radius $\bar{r}/r_0$ as a function of the flight distance x_f for the electrons and ions, respectively. After a free drift stage ($5\,\mu\mathrm{m} \leq x_f \leq 10\,\mu\mathrm{m}$), the laser focusing compensates the divergence of plasma ($10\,\mu\mathrm{m} \leq x_f \leq 20\,\mu\mathrm{m}$). For even larger propagation distances, the slope of the average beam radius $d\bar{r}/dx_f$ indicates a further focusing. Compared to a free drift, a reduction of the average beam radius of a factor of ≈ 1.8 is achieved within a distance of only $x_f \approx 27\,\mu\mathrm{m}$.

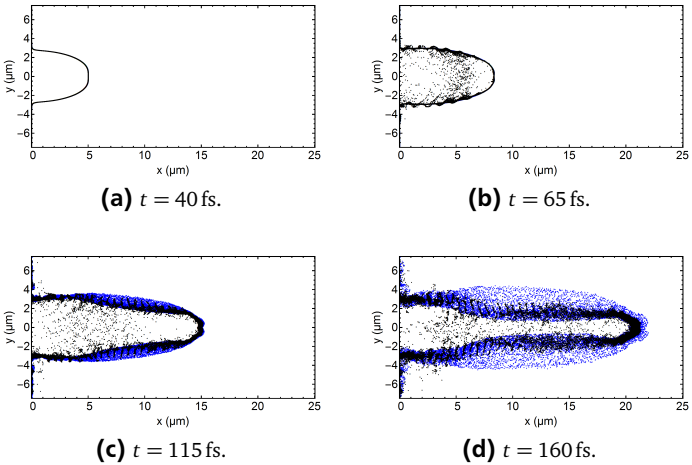

(a) $t = 40\,\mathrm{fs}$. **(b)** $t = 65\,\mathrm{fs}$.

(c) $t = 115\,\mathrm{fs}$. **(d)** $t = 160\,\mathrm{fs}$.

Figure 8.11.: Electrons (black dots) and ions (blue dots) at different times. Clearly visible is the expelling of a part of the ions due to local Coulomb explosion.

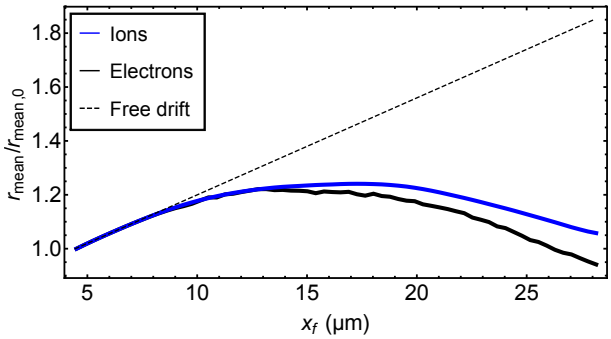

Figure 8.12.: Average beam radius $\bar{r}/r_0$ as a function of the flight distance x_f for the electrons and ions in comparison with the free drift.

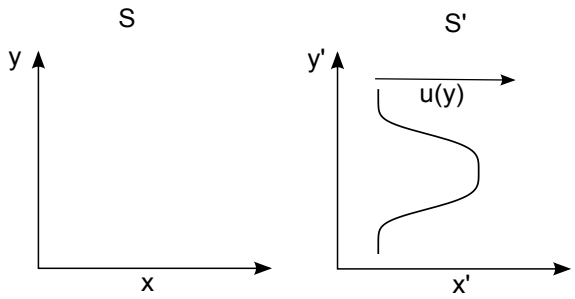

Figure 8.13.: Schematic of the reference frames: S is the fixed laboratory frame, while S' is a frame, co-moving with the plasma. Since the initial plasma has a velocity distribution $u(y)$, a simple Lorentz transformation cannot be applied.

It remains to examine the excitation of electron surface waves by the LIF. For this purpose a reference frame is considered that propagates with the electron longitudinal velocity, as shown in fig. 8.13. Since the longitudinal electron velocity is a function of the transverse coordinate, $u_e^1 = u_e^1(x^2)$[1], the underlying system is rotational: $\nabla \times \vec{u} \neq 0$. A rotational reference frame is accelerated and gyroscopic forces and gyroscopic currents arise.

The dependence of the longitudinal velocity on the transverse space coordinate also leads to a stronger Doppler-shifting of the laser wave in the plasma center compared with the outer wings. Thereby a wave that is plane in the laboratory frame S is warped in S'. In order to describe these physics, a general coordinate-transformation into a local inertial system is performed (cf. chapter 3.2 and appendix A). Given the coordinates $x^\alpha = (ct, \vec{x})$ in the laboratory frame and the Lorentz coordinates x'^α in the local rest frame S', for the transformation between both systems one obtains:

[1] Here, the co-variant notation x^α is used, with $x^1 = x$ and $x^2 = y$. For more detail see chapter 3.2.

$$x'^{\alpha} = \frac{\partial x'^{\alpha}}{\partial x^{\beta}} x^{\beta} = \alpha^{\alpha}_{\beta} x^{\beta} \quad g_{\mu\nu} = \eta_{\alpha\beta} \frac{\partial x'^{\alpha}}{\partial x^{\mu}} \frac{\partial x'^{\beta}}{\partial x^{\nu}}, \tag{8.10}$$

where $x^{\alpha} = (ct, \vec{x})$ are the coordinates in the laboratory frame and x'^{α} are the Lorentz coordinates in the local rest frame S'. Here, $\alpha^{\alpha}_{\beta} = \alpha^{\alpha}_{\beta}(x'^{\gamma})$ denotes the transformation tensor from S to S' and $g_{\mu\nu}$ is the metric tensor with its determinant g. Moreover, $\eta_{\mu\nu} = diag(1,-1,-1,-1)$ is the MINKOWSKI-TENSOR[2]. The co-variant, inhomogeneous MAXWELL EQUATIONS in four vector notation read (cf. chapter 3.2):

$$\frac{1}{\sqrt{|g|}} \partial_{\mu} \sqrt{|g|} F^{\nu\mu} = \mu_0 \sum_k j^{\nu}_k, \tag{8.11}$$

where $F^{\alpha\mu}$ is the MAXWELLIAN FIELD STRENGTH TENSOR and j^{β}_k is the 4-current density vector. Subsequent, all species dependent quantities are labeled with a $k = i, e$ for ions or electrons, respectively. Equations 8.11 are the most general form of Maxwell's Equations, particularly valid in rotational reference systems.

Furthermore, Eqs. 8.11 simplify to the well known Lorentz invariant equations for the case of irrotational plasmas. All gyroscopic forces and currents resulting from the acceleration of the reference frame are included in $g_{\mu\beta}$ and g, respectively. Assuming small perturbations from the linear Lorentz-transformation $g_{\mu\nu} \approx \eta_{\mu\nu} + h_{\mu\nu}$, with $\left|h_{\mu\nu}\right| = \left|g_{\mu\nu} - \eta_{\mu\nu}\right| \ll 1$ and $\alpha^{\alpha}_{\beta} \approx \Lambda^{\alpha}_{\beta} + \lambda^{\alpha}_{\beta}$, one obtains:

$$\sqrt{|g|} \approx 1 + \frac{1}{2} \mathrm{tr}\left(\eta^{\alpha\nu} h_{\alpha\beta}\right), \tag{8.12}$$

where $\mathrm{tr}(\eta^{\alpha\nu} h_{\alpha\beta})$ represents the trace of a tensor. Equations 8.11 simplify to:

$$\partial_{\mu} F^{\nu\mu} - \mu_0 \sum_k j^{\nu}_k = -\frac{1}{2} \partial_{\mu} \mathrm{tr}\left(\eta^{\alpha\nu} h_{\alpha\beta}\right) F^{\nu\mu} \tag{8.13}$$

The left hand side of each equation corresponds to the common Lorentz-invariant description, typically used in (plasma-) physics. The right hand site of each equation corresponds to the gyroscopic sources, caused by the curved shape (= rotational flow) of the plasma. The 00-component of Eqs. 8.13 (GAUSS LAW) gives information about the relation of the electric field and the space charge:

$$\nabla \cdot \vec{E} - \mu_0 c^2 \gamma_0 \sum_k q_k n_k = -\frac{1}{2} \nabla \cdot (\mathrm{tr}(\eta^{\alpha\nu} h_{\alpha\beta}) \vec{E}), \tag{8.14}$$

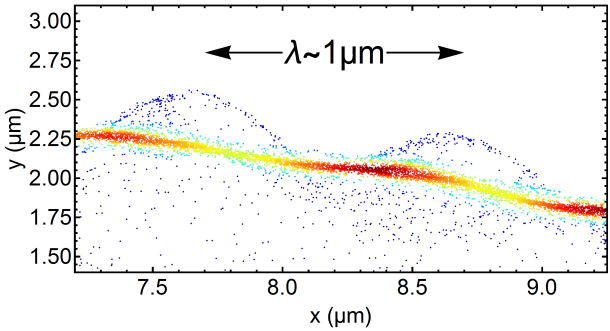

Figure 8.14.: Cutting of the electron surface wave (color denotes density). As predicted by Eq. 8.16, the surface wave follows the laser phase and results from the image currents caused by the rotation of the flow.

where γ_0 is the average Lorentz-factor.

In addition to the space charge $q_k n_k$, fictitious charges appear on the right hand side of Eq. 8.14, caused by the acceleration of the plasma. Assuming purely solenoidal fields $\nabla \cdot \vec{E} = 0$, Eq. 8.14 yields:

$$\nabla \mathrm{tr}(\eta^{\alpha\nu} h_{\alpha\beta}) \cdot \vec{E} = 2\mu_0 c^2 \gamma_0 \sum_k q_k n_k \tag{8.15}$$

Contrary to the common Maxwell's Equations, which state $\sum q_k n_k = 0$ for $\nabla \cdot \vec{E} = 0$, Eq. 8.15 shows that even in case of purely solenoidal fields, there is space charge in a rotational plasma. The space charge wave will strongly depend on the slope of the plasma vacuum interface, but the phase of the wave will be equal to the one of the external electromagnetic field.

Furthermore assuming $E_x = 0$ and $\partial_y \mathrm{tr}(\eta h) = \partial_z \mathrm{tr}(\eta h)$, for symmetry reasons, as well as monochromatic external fields $\vec{E} = E_{0\perp}(\cos(\vec{k}\vec{x} + \omega t)\vec{e}_y + \sin(\vec{k}\vec{x} + \omega t)\vec{e}_z)$, Eq. 8.15 reads:

$$\delta n_e = -\frac{E_{0\perp}}{2\mu_0 c^2 \gamma_0 e} \frac{\partial \mathrm{tr}(\eta h)}{\partial x_\perp} \left(\cos(\vec{k} \cdot \vec{x} + \omega t) + \sin(\vec{k} \cdot \vec{x} + \omega t)\right), \tag{8.16}$$

where $Zen_i - en_e \approx -\delta n_e e$, with $|\delta n_e| \ll n_{e0}$ is used and $E_{0\perp} = E_{0\perp}(\vec{x}, t)$ and $\mathrm{tr}(\eta h) = \mathrm{tr}(\eta h)(\vec{x}, t)$ are permitted to be space and time dependent functions.

[2] Additional to that, the EINSTEIN NOTATION (cf. appendix A) is used.

A detailed view of the electron surface wave is shown in fig. 8.14: As predicted by Eq. 8.16, the wavelengths of the surface wave and the external field are equal. From fig. 8.2 one obtains the equality of the phases of the laser- and the surface wave, confirming Eq. 8.16.

It should be noted that Eq. 8.16 is not a complete solution, rather than a special case, which provides useful information about the phase of the exited electron waves.

8.4 Discussion and applicability of the method

This chapter is finalized with a brief discussion of the applicability of the LIF. Both scenarios, plane and oblique laser focusing achieved a reduction of the average beam radius within a propagation distance of some 10^{th} of micro meters, without the application of solid parts. Coincidentally, the spatial energy density in the beam center increases. However, the laser induced focusing requires a bow shaped, super critical plasma film in order to be applicable. Another downside of the method is the excitation of electron waves on the plasma surface, causing electron heating and local space charge. However, since no solid parts are involved, the laser induced focusing can be applied for an arbitrarily small geometry. Finally, the method is suitable in cases, where space is limited but a certain loss of beam intensity is admissible.

9 Conclusions and outlook

This work addresses the investigation of the RPA with analytic models and PIC simulations, in order to close analytical gaps that are not covered by the insufficient prevalent models. The RPA is identified as a promising method to generate high intense plasma beams [34]. Theoretical models predict kinetic energies, scaling quadratic in laser intensity for the light sail regime [32]. However, the transition from one laser acceleration mechanism to another one is transient and it is essential to determine analytical conditions for the laser and target parameters that are required to obtain a light sail. Plasmas exist with a wide variation of physical properties. For this reason, a characterization of the laser generated plasma is carried out in advance. An estimation of the electron temperature of the laser plasma supplies the approximation of the average charge state and collision frequency in the plasma, justifying the model of a non-collisional and non-dissipative ideal plasma.

The analytical work is initiated by introducing the most general representation of a co-variant two fluid plasma. By successively reducing this model to a more manageable size, the laser plasma interaction separates into three asymptotic limits: On the scales of the electron relaxation time $T \propto \omega_{pe}^{-1}$ and the plasma skin-depth $l \propto \delta$, the RPA is dominated by the interaction of the plasma electrons with the laser and the gas-dynamic properties of the electron gas are negligible. In particular, the electron's response to the laser prevents the latter from penetrating the plasma sheet. On large scales, $T \gg \omega_{pe}^{-1}, l \gg \delta$, electromagnetic effects are negligible and the RPA is characterized by the plasma's gas-dynamic properties and the plasma is modeled as a neutral gas. For an ultra strong laser, the ablation pressure of the plasma is negligible compared to the radiation pressure of the laser and the plasma acts as a deformable mirror.

Previous simulation work[53] shows that a reduction of the electron heating during the RPA is achieved by utilizing a CP rather than a LP laser. However, an adequate analytic explanation remained unsettled. This work closes the gap by deriving a transport equation for the entropy from a relativistic two fluid picture, showing that the entropy production is significantly reduced by using a CP instead of a LP laser.

Based on the assumption of perfect reflectivity for over-dense plasmas, prevalent analytic models[38, 39] predict a light sail acceleration for a wide range of target and laser parameters. However, simulations performed in the course of this work show that initially too narrow targets get transparent to the laser and the acceleration process is terminated. By investigating the short scale dynamics of the

RPA process with an extended linear two fluid model, a condition for a lower limit of the target width is derived. Targets narrower than the derived limit will cause the acceleration to collapse. Using a relativistic two fluid model, the reflection-transmission problem is solved and an optimization in terms of a minimization of the velocity spread is achieved. Contrary to previous arguments [33], longer laser pulses cause lower energy spread than short pulses.

The order of magnitude for the required laser intensity and target parameters to start the RPA were previously estimated by empirical values[35, 31], obtained from simulations. In the present work, an analytic condition for the required laser intensity is provided by applying simple waves to the large scale dynamics of the RPA. For this purpose an artificial piston is introduced by a continuity condition for the laser and plasma momentum flux and subsequently the characteristics method from classical gas-dynamics is applied. From the requirement of strong shocks, the desired condition is finally derived. As verified by simulations, the RPA does not start for laser intensities below this threshold, even for infinite pulse duration. It turns out that the required intensity is related to the electron temperature and that its significance has formerly been under-rated. From the same model an expression for the admissible upper limit of the target width for finite laser pulse duration is derived. All analytic results are validated against simulation results and agree well in their range of validity. In particular, the verification of the 1D models with 2D simulations shows the validity of the derived condition also in higher dimension.

Recent work [33] showes that the divergence of the emerging plasma was underestimated formerly. In the limit of strong acceleration, an analytic model for the divergence is derived. Depending on the laser and target parameters, the expected divergence is in the range of $\vartheta \approx 5^\circ - 25^\circ$. This perception motivates the last part of the thesis that covers the development of a new transport mechanism for super-critical plasma sheets. For high intense plasma beams, as generated by RPA, traditional focusing with magnetic fields is inappropriate. Hence, the new method developed in the present work uses the radiation pressure of a counter-propagating laser beam, rather than solid parts for focusing.

Recent research focuses the mechanisms of laser plasma acceleration itself. However, the creation of the plasma in the first atto to femto seconds of the laser impact is not fully understood yet. Therefore, future research could investigate the phase transition from a solid or liquid body to a plasma, e.g. by extending the Stefan-problem. By that, the significant, but elusive parameter of the initial electron temperature could be achieved. As a plasma is a mix of two or more different gas species with different mass densities driven by a laser, it is prone to composite instabilities, e.g. the RTI. Future studies could investigate the stability of the RPA and its sensitivity to manufacturing errors. In addition, a further extension of the

presented model could be achieved by including radiative transport effects that occur at high electron temperatures. Radiative transport effects cause a smoothing of the evolving shock wave in the plasma.

Acknowledgements

First, I want to thank Prof. Dr. Oliver Boine-Frankenheim, who offered me the position at TEMF and by that made this work possible. Through him, I entered the highly interesting field of laser plasma physics. Our discussions helped me to strongly improve my scientific skills and often advanced in my work. He also offered me the opportunity to participate in numerous scientific conferences and workshops, where I compared notes with international scientists working in the field of laser plasma physics.

Furthermore, I want to thank Prof. Dr. Wolfgang F. Ellermeier. For many years he educated and guided me through the fields of analytical mechanics, fluid mechanics and field theory. Whenever I encountered a problem or got stuck, he had an open door for me and helped me with his extensive knowledge about analytical physics and his advices. From him I received my excellent education in analytical physics and I owe him much.

Similar thanks goes to Prof. (emeritus) Dr. Peter Mulser, who has been my Mentor for my time as a PhD student. Our fruitful discussions often brought me to the right track. Within these discussions, Prof. (emeritus) Dr. Peter Mulser gave me an understanding of the complete spectrum of plasma physics and inspired me to extend my knowledge.

I also thank Prof. Dr. Ingo Hofmann, who showed me a more general classification of the laser acceleration within the field of accelerator and applied physics.

Further thanks goes to the head of the institute Prof. Dr. Herbert De Gersem and the former head of the institute, Prof. Dr. Thomas Weiland. The good working atmosphere at the TEMF institute gave me the support, necessary to finalize this work. Aside from this, the institute provided me with the necessary traveling money to attend the conferences I participated while my PhD student time.

I thank the graduate school HGS-HIRe and HIC for FAIR for supplying me with a scholarship and traveling budget during my time as a PhD student.

Special thanks goes to my friend Christopher Peuser, for proofreading the thesis and advancing it with their fruitful comments.

Moreover, I thank my office colleagues Oliver S. Haas and Dr. David Bizzozero for our good office atmosphere and the many availing discussions. Oliver Haas explained the basic concepts of computational physics and numerical methods to me and helped me to improve my work. Dr. David Bizzozero assisted me with mathematical details of the work and helped me to improve my English skills.

In addition I thank Dr. Uwe Niedermeyer and Dr. Paul Görgen for their organizational assistance and support in cases of computer issues.

Great gratitude is due to the whole TEMF team. The casual working atmosphere often backed me in times I became despair of my work.

In the end I want to express my gratitude to my family. My mother Monika Grün-Schmidt and my father Karlheinz Schmidt gave me the opportunity to study physics and encouraged me at all my interests and plans. Furthermore I thank my sister Rebecca Schmidt, my uncle Albert Schmidt and my grandmother Margarete Schmidt, who supported me while my studies and are always there for me.

My last thanks goes to all my friends for encouraging me and helping me coming to rest after work. Family and friends are the backbone of every great work.

A Minkowski Space $\mathbb{M}^4$ and Riemann Manifolds

Across this work, 4-vector notation for co-variant, as well as Lorentz-invariant fluid equations are used. This chapter provides a brief overview over Minkowski space and Riemann manifold. The interested reader is referred to the common literature [54, 55] for details. The notation used across this work coincides with the notation in [55].

Definition 1 (Minkowski Space)**.** *The four dimensional vector space $\mathbb{M}^4$ with the given metric*

$$ds^2 = \eta_{\alpha\beta} dx^\alpha dx^\beta = c^2 dt^2 - dx^2 - dy^2 - dz^2 \tag{A.1}$$

is called a Minkowski Space*. Here $x^\alpha = (ct, x, y, z)^T$ is the 4-vector, $\alpha, \beta = 0, 1, 2, 3$ is the index of the corresponding component of a 4-vector and $\eta_{\alpha\beta} = diag(1, -1, -1, -1)$ is identified as the* Minkowski Tensor*. The length is then defined by the integral*

$$\int ds = \int \sqrt{\eta_{\alpha\beta} u^\alpha u^\beta} d\tau \tag{A.2}$$

With $u^\alpha = dx^\alpha / d\tau$ and $u^\beta = dx^\beta / d\tau$ being the 4-velocities. The time scale τ is called eigen time *and is related to: $d\tau = ds/c$.*

Here Einstein Notation is used:

Definition 2 (Einstein Notation)**.** *In 4-vector notation, a term consisting of quantities with equal lower and upper index, are summed over this index. An index in* Minkowski Space *is raised or lowered by the Minkowski tensor: $x_\alpha = \eta_{\alpha\beta} x^\beta$ and therefore using the Einstein Notation $x^\alpha x_\alpha = x^\alpha \eta_{\alpha\beta} x^\beta = c^2 t^2 - x^2 - y^2 - z^2$.*

The Lorentz transformation is a direct consequence of the metric given in definition 1.

Definition 3 (Riemann Manifold)**.** *Given a smooth, differentiable manifold M with a metric*

$$ds^2 = g_{\mu\nu} dx^\mu dx^\nu \tag{A.3}$$

is called a Riemann Manifold *or* Riemann Metric Space*. The length is then defined by the integral*

$$\int ds = \int \sqrt{g_{\mu\nu} u^\mu u^\nu} d\tau \tag{A.4}$$

With $u^\mu = dx^\mu/d\tau$ and $u^\nu = dx^\nu/d\tau$ being the 4-velocities. The second rank quantity $g_{\mu\nu}$ is called Metric Tensor*, that reads:*

$$g_{\mu\nu}(x') = \eta_{\alpha\beta} \frac{dx^\alpha}{dx'^\mu} \frac{dx^\beta}{dx'^\nu} \tag{A.5}$$

Where the prime denotes quantities evaluated in the tangent space, given by the Minkowski Space $\mathbb{M}^4$.

B Supplementary notes to the analytical models

B.1 Pressure of a neutral plasma

In the limit of large scales, the equations of motion for the plasma reduce to the equations of a neutral one species fluid. The pressure term is composed by the electron pressure and the plasma mass density, given by the ion mass density:

$$\begin{aligned}\nabla p_e = \frac{\partial p_e}{\partial \rho_e}\nabla\rho_e &= \frac{\varkappa k_B n_{e,0} T_{e,0}}{n_{e,0} m_e}\left(\frac{m_e n_e}{m_e n_{e,0}}\right)^{\varkappa-1}\nabla m_e n_e \\ &= \varkappa k_B T_{e,0}\left(\frac{Z m_i n_i}{Z m_i n_{i,0}}\right)^{\varkappa-1}\frac{1}{m_i}\nabla m_i Z n_i \\ &= \frac{Z\varkappa k_B T_{e,0}}{m_i}\left(\frac{\rho}{\rho_0}\right)^{\varkappa-1}\nabla\rho \\ &= a_0^2\left(\frac{\rho}{\rho_0}\right)^{\varkappa-1}\nabla\rho, \quad a_0^2 = \frac{Z\varkappa k_B T_{e,0}}{m_i}\end{aligned} \tag{B.1}$$

Here, a_0 is the equilibrium isentropic speed of sound for the ion acoustic wave.

B.2 Conservation of the angular momentum

In this section, the angular momentum transfer from the laser to the plasma is reviewed. From Poynting's theorem [54] one obtains:

$$\frac{d}{dt}\left(\vec{L}_{EM} + \vec{L}_e + \vec{L}_i\right) = -\oint_{\partial V}\left(\underline{\underline{T}}\times\vec{r}\right)\hat{n}dS, \tag{B.2}$$

where the angular momentum of the electromagnetic wave $\vec{L}_{EM}$ is:

$$\vec{L}_{EM} = \int_V c^{-2}\vec{r}\times\vec{S}dV, \quad \vec{S} = \mu_0^{-1}\vec{E}\times\vec{B}, \tag{B.3}$$

with $\vec{S}$ being the Poynting vector and $T_{ij} = 1/2(\epsilon_0 E^2 + \mu^{-1}B^2)\delta_{ij} - \epsilon_0 E_i E_j - \mu^{-1}B_i B_j$ being the MAXWELL STRESS TENSOR. Thus, the conservation of the angular momentum states:

$$\begin{aligned}\frac{d}{dt}\int_V c^{-2}\vec{r}\times\vec{S}dV + \frac{d}{dt}\sum_{\alpha=e,i}\int_V n_\alpha m_\alpha \vec{r}\times\vec{u}_\alpha dV \\ = -\oint_{\partial V}\left(\underline{\underline{T}}\times\vec{r}\right)\hat{n}dS\end{aligned} \tag{B.4}$$

Assuming a plane, circular polarized laser pulse propagating in z-direction $\hat{k} = \vec{e}_z$ with $\vec{E} = E_0(z,t)\vec{e}_r$, with $E_0(z,t)$ being the field amplitude, slowly varying in space and time, $\vec{B} = c^{-1}E_0(z,t)\vec{e}_\varphi$ and phase $\varphi = kz - \omega t$, as well as the position vector $\vec{r} = r\vec{e}_r + z\vec{e}_z$ it holds: $\vec{S} = \epsilon_0 c E_0^2 \vec{e}_z$ and $\underline{\underline{T}} = \mathrm{diag}(0,0,\epsilon_0 E_0^2)$. The angular momentum density $\vec{l}_{EM} = c^{-2}\vec{r}\times\vec{S}$ of the electromagnetic wave thus reads: $\vec{l}_{EM} = \epsilon_0 c^{-1}E_0^2 r\vec{e}_\varphi$. Integration of the same over a full angle $\varphi \in [0, 2\pi]$ vanishes. The term $\underline{\underline{T}}\times\vec{r}$ with the given coordinate system is given as:

$$\underline{\underline{T}}\times\vec{r} = \frac{E_0^2}{\mu c^2}\begin{pmatrix}0 & 0 & 0\\ 0 & 0 & 0\\ -\sin\varphi & \cos\varphi & 0\end{pmatrix} \tag{B.5}$$

The normal vector of the plasma interface is $\hat{n} = -\vec{e}_z$, such that the product $\left(\underline{\underline{T}}\times\vec{r}\right)\hat{n} = 0$ vanishes, too. Thus, only the angular momentum from the ions and electrons remains. Moreover, it holds: $\vec{u}_\alpha = u_{\varphi,\alpha}\vec{e}_\varphi + u_{z,\alpha}\vec{e}_z$, since there is no radial velocity in case of a plane laser wave [74] and it holds: $\vec{r}\times\vec{u}_\alpha = -ru_{z,\alpha}\vec{e}_\varphi + ru_{\varphi,\alpha}\vec{e}_z - u_{\varphi,\alpha}z\vec{e}_r$. Again, all φ dependent terms cancel out by an integration over a full angle and the remaining terms give:

$$\frac{d}{dt}\int_V n_i m_i u_{\varphi,i}\vec{e}_z r dV = -\frac{d}{dt}\int_V n_e m_e u_{\varphi,e}\vec{e}_z r dV \tag{B.6}$$

Assuming quasi neutrality of the plasma, that is $Zn_i \approx n_e$, one obtains the relation of the ions and electrons azimuthal velocities, which is used across this work: $u_{\varphi,e}/u_{\varphi,i} = m_i/m_e \gg 1$.

B.3 Extended CF model

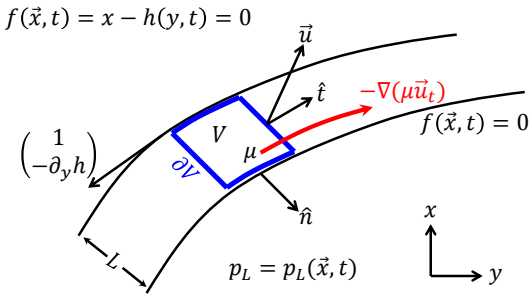

Figure B.1.: Illustration of the advanced current flag model: Assuming a fixed plasma slab thickness $L = const$, mass can only be transported transverse to the surface $f(x,y,t)$.

In this section, the CF model is further extended by an additional mass flow. As before, the plasma vacuum interface is described by an analytic function $f(\vec{x},t) : \mathbb{R}^2 \times \mathbb{R}_0^+ \to \mathbb{R}$, for which according to LIOUVILLE'S THEOREM 1 holds: $d_t f = 0$. The plasma flag is assumed to have a fixed thickness $L = const$, $L \in \mathbb{R} : L > 0$ and thus, mass can only be transported tangential to the interface f, as depicted in fig. B.1. If $\mu = \rho L$ is the areal plasma density, then the mass conservation states:

$$\begin{aligned} &\partial_t \mu + \nabla \cdot [\mu(\vec{u} - \hat{n}(\hat{n} \cdot \vec{u}))] = 0 \Leftrightarrow \\ &\partial_t \mu + \nabla \cdot \left[\mu \hat{t}(\hat{t} \cdot \vec{u})\right] = 0, \end{aligned} \tag{B.7}$$

where $\hat{n}$ is the surface normal vector and $\hat{t}$ is the surface tangential vector and $\mu(\vec{x},t) : \mathbb{R}^2 \times \mathbb{R}_0^+ \to \mathbb{R}_0^+$. Applying NEWTON'S SECOND LAW gives the momentum conservation:

$$\frac{d\mu\vec{u}}{dt} = p_L \hat{n} \tag{B.8}$$

Here, μ can not be excluded from the time derivative, since it is a function of space and time itself. For not to large slope $\hat{n} \approx \nabla f$ holds and one may write:

$$
\begin{aligned}
&\partial_t h + v\partial_y h - u = 0 \\
&\partial_t \mu + \left(v + u\partial_y h\right)\partial_y \mu + \mu\partial_y v = 0 \\
&\mu\frac{d\vec{u}}{dt} = p_L\hat{n} - \frac{\partial\mu}{\partial t}\vec{u}
\end{aligned}
\tag{B.9}
$$

These equations reveal interesting information about the influence of the surface slope to the areal density fluctuation: The continuity equation contains an additional term $\partial_y h\partial_y \mu u$, which transports mass depending on the surface slope $\partial_y h$. But more important, the equation of motion contains a friction term $-\partial_t \mu\vec{u}$ on the right hand side, whose friction coefficient $\partial_t \mu$ depends on time and space. Obviously the friction is dominated by the mass flow $\partial_t \mu$, which in other words states that the acceleration $d_t\vec{u}$ is decreased due to the mass flow. Part of the available laser energy is transferred into mass transport inside the plasma slab, such that the fraction of energy which contributes to the acceleration of the slab is decreased. From further re-arranging the equations, one obtains:

$$
\begin{aligned}
&\partial_t h + v\partial_y h - u = 0 \\
&\partial_t \mu + \partial_y\left(\mu v\right) = -u\partial_y \mu\partial_y h \\
&\mu\frac{du}{dt} = p_L \\
&\mu\frac{dv}{dt} = -p_L\partial_y h - v^2\frac{\partial\mu}{\partial y}
\end{aligned}
\tag{B.10}
$$

This shape of the equations reveals even more useful information: The mass conservation now has a mass sink $-u\partial_y \mu\partial_y h$ on the right hand side and one obtains that mass is transported away from areas of high surface slopes $\partial_y h$ to areas of vanishing surface slope. By that, high surface slope areas are diluted. The friction term in the transverse equation of motion $-v^2\partial_y \mu$ turns out to be very similar to a hydrodynamic pressure gradient $a_0^2\nabla\rho$, where the sound velocity a_0 in this case is interchanged by the plasma transverse velocity v. By that, the acceleration of the slab is decreased by the amount of energy which is converted into volume work of this pressure force term. Since Eqs. B.9 or B.10, respectively, are obtained by linearization, strictly speaking they are valid only in regions where $\partial_y h \ll 1$. However the ECFM yet provides useful information. An extensive analytic treatment of the ECFM Eqs. B.10 is inhibited by the mix derivatives $\partial_y h\partial_y \mu$, because due to that, Eqs. B.10 are not a strictly hyperbolic first order PDE system. In addition, a further series expansion up to linear order would erase all terms, which are connected

with a surface slope dependent mass transport, such that one would end up with the simple CFM.

Since the mass flow depends on the surface slope ∂_y, one expects that it has its maximum at the inflection points $\partial_{yy}h = 0$, where the surface slope has its extrema. Figure B.2 shows exemplary density plots of the plasma from the 2D full EM PIC simulation for different laser envelopes and intensities. For a Gaussian laser focus, as shown in fig. B.2a, the plasma concentrates around the extreme value at $y = 0$, where $\partial_y h = 0$ holds. As stated earlier, mass is transported from regions with high $\partial_y h$ to the center and to the flat outer wings of the plasma. In case of Lorentz function profile (see fig. B.2b), the highest plasma concentration is achieved at the plasma wings, for which hold $\lim y \to \pm\infty : \partial_y h \to 0$ as predicted by the above model. The same holds true for a 4^{th} order Gaussian laser focus, as obtained by fig. B.2c. Additional to that, a plasma concentration is achieved at the saddle point center plateau at $y = 0$. Figure B.2d shows the density distribution for a Gaussian laser, but with a four times higher intensity. In this case, the RPA is dominated by the RTI, which is clearly visible from the density fluctuations in fig. B.2d and in C.5d. Unfortunately, the RTI causes turbulences, or in other words loops of the plasma interface f, such that $\exists y \in \mathbb{R}$ with $x_1 = h(y)$, $x_2 = h(y)$ and $x_1 \neq x_2$ holds. By that, the uniqueness of the image is violated and thus, $h(y,t)$ is not an analytic map anymore. Therefore, this case can not be treated by the extended CFM (ECFM) [1].

A numerical solution of Eqs. B.10 is shown in the density plots in fig. B.3, for a Gaussian (cf. fig. B.3a), a Lorentz (cf. fig. B.3b) and a 4^{th} order Gaussian (cf. fig. B.3c) laser spot. Good agreement with results from the PIC simulations (cf. fig. B.2) is achieved for the shape, as well as the density distribution of the emerging plasma, validating the analytical model.

In summary, the extended current flag model is suitable to estimate the density distribution of the RPA beam. It turns out that low slope regions in the plasma center accumulate mass, whilst the plasma flanks are diluted. Supposing an isentropic plasma, the temperature is given as $T_e = T_{e,0}(\mu/\mu_0)^{\varkappa-1}$, such that, according to the previous results, the heating is strongest in the plasma center. Moreover, the model adds a correction to the previously derived divergence, since the friction force decreases the transverse velocity.

[1] To solve this issue, one may transfer the adv. CFM to the complex plane, where an analytic function with loops can be constructed.

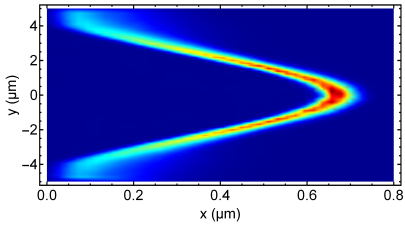

(a) Gaussian, $I = 5 \cdot 10^{20}\,\mathrm{W/cm^2}$.

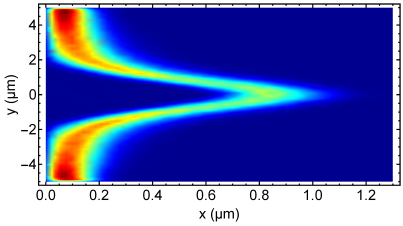

(b) Lorentz, $I = 5 \cdot 10^{20}\,\mathrm{W/cm^2}$.

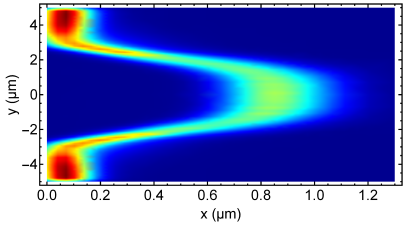

(c) 4^{th} order Gaussian, $I = 5 \cdot 10^{20}\,\mathrm{W/cm^2}$.

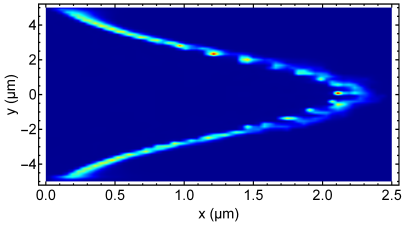

(d) Gaussian, $I = 2 \cdot 10^{21}\,\mathrm{W/cm^2}$.

Figure B.2.: Density plot for different laser spot shapes and intensities.

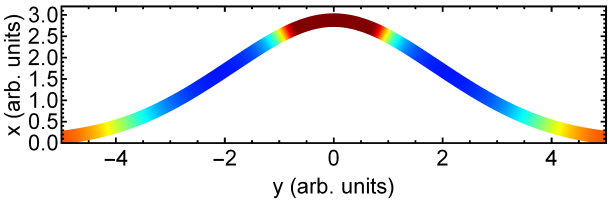

(a) Gaussian.

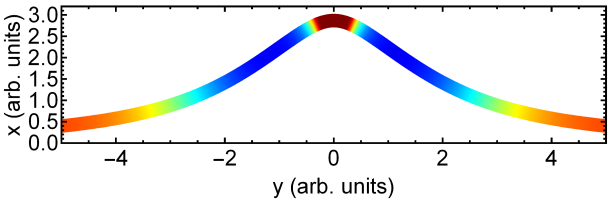

(b) Lorentz.

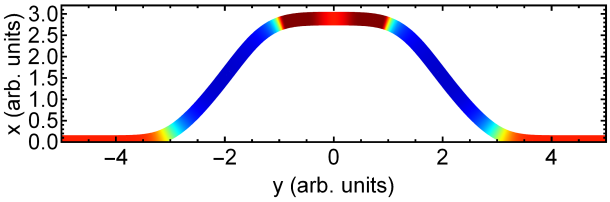

(c) 4^{th} order Gaussian.

Figure B.3.: Density plot for different laser spot shapes obtained by the numerical integration of Eqs. B.10, for arbitrary parameters.

B.4 Complete solution of the transmission reflexion problem

In this section, the full solution of the reflection transmission problem in section 6.2.4 is provided. The Fourier transformation of the electrical field components is:

$$F^k\left(x',\omega'\right)=\frac{1}{\sqrt{2\pi}}\int_{-\infty}^{\infty}E_{\perp}^{k}(x',t')e^{-it'\omega'}dt' \tag{B.11}$$

With the usual Ansatz

$$\begin{aligned}\hat{F}^{I\prime}\left(x',\omega'\right)&=\hat{F}_i'\left(\omega'\right)e^{ik_I'x'}+\hat{F}_t'\left(\omega'\right)e^{-ik_I'x'}\\ \hat{F}^{II\prime}\left(x',\omega'\right)&=\hat{F}_t'\left(\omega'\right)e^{ik_{II}'x'}+\hat{F}_{r,rear}'\left(\omega'\right)e^{-ik_{II}'x'}\\ \hat{F}^{III\prime}\left(x',\omega'\right)&=\hat{F}_{t,rear}'\left(\omega'\right)e^{ik_{III}'x'},\end{aligned} \tag{B.12}$$

the full solution of the problem shown in Fig. 6.9 in the frequency domain is:

$$\begin{aligned}\hat{F}^{I\prime}\left(x',\omega'\right)&=\hat{F}_i'\left(\omega'\right)e^{ik_I'x'}\\ &+\hat{F}_i'\left(\omega'\right)\frac{\left(k_I'-k_{II}'\right)\left(k_I'+k_{II}'\right)\sin k_{II}'L'}{2ik_I'k_{II}'\cos k_{II}'L'+\left(k_I^{2\prime}+k_{II}^{2\prime}\right)\sin k_{II}'L'}e^{-ik_I'x'},\end{aligned} \tag{B.13}$$

$$\begin{aligned}&\hat{F}^{II\prime}\left(x',\omega'\right)=\\ &\hat{F}_i'\left(\omega'\right)\frac{-2\left(k_I'+k_{II}'\right)k_I'}{\left(k_I'-k_{II}'\right)^2e^{2ik_{II}'L'}-\left(k_I'+k_{II}'\right)^2}e^{ik_{II}'x'}\\ &+\hat{F}_i'\left(\omega'\right)\frac{2\left(k_I'-k_{II}'\right)k_I'e^{2ik_{II}'L'}}{\left(k_I'-k_{II}'\right)^2e^{2ik_{II}'L'}-\left(k_I'+k_{II}'\right)^2}e^{-ik_{II}'x'},\end{aligned} \tag{B.14}$$

$$\begin{aligned}&\hat{F}^{III\prime}\left(x',\Omega'\right)=\\ &\hat{F}_i'\left(\omega'\right)\frac{2ie^{-ik_I'L'}k_I'k_{II}'}{2ik_I'k_{II}'\cos k_{II}'L'+\left(k_I^{2\prime}+k_{II}^{2\prime}\right)\sin k_{II}'L'}e^{ik_I'x'},\end{aligned} \tag{B.15}$$

where $\hat{F}_i'(\omega')$ is the frequency spectrum of the incident laser wave, $k_{I,II}'=\omega'/c$ and $k_{II}'=\omega'/c\sqrt{1-\omega_{pe}^2/\omega'^2}$ are the wave numbers and L' is the slab width in the reference frame S'.

B.5 Additional notes to the divergence angle

For a proper comparison of the divergence for different laser focal spot shapes, it is obviously necessary to keep the overall laser energy constant, that is: Having two different laser shape functions $g(\eta,\tau)$ and $f(\eta,\tau)$, it holds:

$$\int_0^\infty \int_{-\infty}^\infty g(\eta,\tau)d\eta d\tau = \int_0^\infty \int_{-\infty}^\infty f(\eta,\tau)d\eta d\tau \tag{B.16}$$

Consider for instance $g(\eta,\tau) = 4\tau^2\exp(-a^2\eta^2)\exp(-4\tau^2+1)$, with $a^2 = L^2/2\sigma^2$ and $f(\eta,\tau) = 4\tau^2\exp(-b^2\eta^4)\exp(-4\tau^2+1)$, it is:

$$\frac{\sqrt{\pi}}{a} = \frac{2\Gamma(5/4)}{b} \quad \rightarrow \quad b = \frac{2a\Gamma(5/4)}{\sqrt{\pi}} \approx 1.023a \tag{B.17}$$

Where $\Gamma(x)$ is the Eulerian Gamma function, defined as $\Gamma(n+1) = n!$. For that case the inflection point of the shape function f is: $\eta_{ip} = \sqrt{\pi}\ln(2)^{1/4}/2\Gamma(5/4)a \approx 0.89/a$. With these parameters, one obtains from Eq. 7.8, the divergence angle:

$$\vartheta = \arctan(\frac{(8-7\sqrt{2})\Gamma(5/4)\ln(2)^{3/4}}{16\sqrt{\pi}}aA_0^2) \approx \arctan(0.046aA_0^2) \tag{B.18}$$

Another example can be constructed if one chooses the laser envelope to be shaped by a Lorentz function $f(\eta) = 1/(1+\eta^2/c^2)$, with $c = 1/\sqrt{\pi}a$, and $\eta_{ip} = c$. Then the divergence angle of the plasma beam is:

$$\vartheta \approx \arctan(0.072aA_0^2) \tag{B.19}$$

If one refers to the above time/pulse envelope and only changes the transverse focal spot shape, the derivation can be simplified to:

$$\vartheta = \arctan\left(\frac{(7\sqrt{2}-8)e}{64}A_0^2 g'(\eta)\big|_{\eta=\pm\eta_{ip}/2}\right) \tag{B.20}$$

B.6 Notes on the stability of the emerging plasma

In chapter 7 it is observed, that the RTI has severe influence on the dynamic of the emerging plasma. The RTI is a two fluid instability and thus not accessible by a one fluid model. Particularly, the required uniqueness of the interface function f is lost due to the turbulence, driven by the RTI. However, a similar instability can be derived from the CFM. Recalling the equations of motion:

$$\begin{aligned}
&\partial_\tau \xi + \beta_y \partial_\eta \xi - \beta_x = 0 \\
&\partial_\tau \beta_x + \beta_y \partial_\eta \beta_x - A_0^2 g(\eta,\tau)\left(1 - \partial_\eta \xi^2\right) = 0 \\
&\partial_\tau \beta_y + \beta_y \partial_\eta \beta_y - A_0^2 g(\eta,\tau)\partial_\eta \xi = 0,
\end{aligned} \tag{B.21}$$

where the second equation is expanded to the next higher order in $\partial_\eta \xi$. A linearization with respect to small perturbations in β_y gives:

$$\begin{aligned}
&\partial_\tau \xi - \beta_x = 0 \\
&\partial_\tau \beta_x - A_0^2 g(\eta,\tau)\left(1 - \partial_\eta \xi^2\right) = 0 \\
&\partial_\tau \beta_y - A_0^2 g(\eta,\tau)\partial_\eta \xi = 0
\end{aligned} \tag{B.22}$$

This series expansion is accurate for small divergence angles or equivalently large laser spot sizes. By that, the first and second equation decouple from the third. Differentiation of the first equation with respect to τ and inserting the second finally gives:

$$\partial_{\tau\tau} \xi - A_0^2 g(\eta,\tau)\left[1 - \partial_\eta \xi^2\right] = 0 \tag{B.23}$$

Equation B.23 is a second order, non-linear partial differential equation with time and space dependent coefficients. Unfortunately, Eq. B.23 can not be split into a system of two, first order hyperbolic equation. Thus, the mathematical treatment of Eq. B.23 is very difficult. But some general statements may regardless be made. The acceleration $\partial_{\tau\tau}\xi$ of the plasma slab depends on the spatial derivative $\partial \eta \xi$ of the same. Thus, the acceleration of the plasma decreases in areas where $\partial_\eta \xi$ is larger compared to areas with smaller $\partial_\eta \xi$. Due to the square in $\partial_\eta \xi^2$, the acceleration is furthermore independent of the direction of the derivative. If we require the function ξ to have initial conditions, Eq. B.23 formally expands to a CAUCHY PROBLEM:

$$\begin{aligned}
&\partial_{\tau\tau}\xi - A_0^2 g(\eta,\tau)\left[1-\partial_\eta \xi^2\right] = 0\\
&\xi(0,\eta) = f(\eta)\\
&\partial_\tau \xi(\eta,0) = 0,
\end{aligned} \tag{B.24}$$

with the requirement: $f : \mathbb{R} \to \Omega \subset \mathbb{R}$, with Ω bounded, is an analytic, bounded and non constant function, thus it holds: $\exists \eta_1, \eta_2 \in \mathbb{R}$ with $\eta_1 \neq \eta_2$ for which holds: $f(\eta_1) \neq f(\eta_2)$. From the requirement of a continuously differentiable function follows non-constant f. For these conditions, the CAUCHY-KOWALEWSKAJA THEOREM secures the existence of a unique solution of B.24:

Theorem 2 (Cauchy-Kowalewskaja Theorem)**.** *If F and $_j$ are analytic functions near $t = 0$, then the non-linear Cauchy problem of type*

$$\begin{aligned}
\partial_t^k h = F\left(x, t, \partial_t^j \partial_x^\alpha h\right), \quad \textit{where} \quad j < k \quad \textit{and} \quad |\alpha| + j \leq k\\
\partial_t^j h(x,0) = f_j(x), \quad 0 \leq j < k
\end{aligned} \tag{B.25}$$

has a unique and analytic solution near 0*.*

Proof. See e.g. [70]. □

For instance, f could be given as an initial ripple $f(\eta) = \lambda_p \cos(\varkappa_p \eta)$, which would represent initial fabrication errors of the target. It follows that $\exists \eta \in \mathbb{R}$ such that $\partial_\eta \xi(\eta,0) \neq 0$. By that, the initial perturbation is amplified, since $\partial_{\tau\tau}\xi = \partial_{\tau\tau}\xi(\eta)$. For $\partial_\eta \xi > 1$ a sign inversion appears and thus the type of solution changes, which can be seen as an instability. Whether this happens or not, depends on the amplitude of the initial perturbation $f(\eta)$, the impact time τ and the acceleration A. If the initial perturbation satisfies $\partial_\eta f(\eta) > 1$ for some $\eta \in \mathbb{R}$ this sign inversion obviously appears instantaneously. For $\partial_\eta f(\eta) < 1$ and a bounded acceleration, that is $g(\eta,\tau) \to 0$ for $\tau \to \infty$, the occurrence of a sign inversion depends on the impact time and the acceleration. If one uses a DC laser, that is $g = g(\eta)$, there will always be a $\tau \in \mathbb{R}_0^+$ for which the acceleration becomes unstable. In other words, an initially non-flat foil driven by a DC laser will always become unstable after a finite time.

The Rayleigh Taylor Instability causes turbulence of the plasma vacuum interface f, such that uniqueness is violated and thus, this effect can not be described by a unique, analytic function f. Below, we give a short proof of this statement:

Theorem 3 (Violation of uniqueness by turbulence)**.** *In case of turbulence, loops arise in the interface f, such that $\exists y(\tau) \in \mathbb{R}$, $\tau \in \mathbb{R}^+$ with $x_1 = h(y,\tau)$, $x_2 = h(y,\tau)$ with $x_1 \neq x_2$. Then the uniqueness of the interface $f(x,y,t)$ is violated and thus f is not a map.*

Proof. Proof by contradiction: Assume a unique $f = x - h(y,t)$, which satisfies Liouville's Theorem 1, with $d_t f = d_t x - d_t y\,\partial_y h - \partial_t h = 0$. According to the assumption, it holds:

$$\begin{aligned} d_t x_1 - d_t y\,\partial_y h - \partial_t h = 0 \\ d_t x_2 - d_t y\,\partial_y h - \partial_t h = 0 \end{aligned} \tag{B.26}$$

Subtraction of the first from the second equation gives: $d_t x_2 - d_t x_2 = 0$. Integrating once with respect to t then gives: $x_2 = x_1 + c$, where $c \in \mathbb{R}$ is an arbitrary constant $c = const$. But then $f_2 = f_1 - c$ and thus $f_2 \neq f_1$ and by that uniqueness and therefore the above assumption is violated. □

B.7 Justification of the CFM

A justification for the CFM can be obtained by showing that the continuity equation for the charge and current density is inevitably satisfied by the boundary conditions. In a system S' co-moving with the current flag (cf. fig. 3.2), the boundary conditions

$$\begin{aligned} \hat{n} \times \left[\vec{E}'\right] = 0, \quad \hat{n} \cdot \left[\vec{D}'\right] = \sigma_s' \\ \hat{n} \cdot \left[\vec{B}'\right] = 0, \quad \hat{n} \times \left[\vec{B}'\right] = \mu_0 \vec{j}_s', \end{aligned} \tag{B.27}$$

remain valid. From this one obtains:

$$\begin{aligned} \sigma_s' &= \hat{n}' \cdot \vec{E}_1' \\ \vec{j}_s' &= \mu_0^{-1} \hat{n}' \times \vec{B}_1' \end{aligned} \tag{B.28}$$

The continuity equation in S' is:

$$\begin{aligned} & \partial_{t'} \sigma_s' + \nabla' \vec{j}_s' = 0 \\ \Leftrightarrow\ & \partial_{t'} \left(\hat{n}' \cdot \vec{E}_1'\right) + c^2 \nabla' \left(\hat{n}' \times \vec{B}_1'\right) = 0 \\ \Leftrightarrow\ & \hat{n}' \cdot \partial_{t'} \vec{E}_1' + \partial_{t'} \hat{n}' \cdot \vec{E}_1' + c^2 \left[\vec{B}_1' \left(\nabla' \times \hat{n}'\right) - \hat{n}' \left(\nabla' \times \vec{B}_1'\right)\right] = 0 \end{aligned} \tag{B.29}$$

With $\hat{n}' \approx \nabla' f'$ and re-arranging one obtains:

$$\nabla' f' \cdot \left[\underbrace{\partial_{t'} \vec{E}_1' - c^2 \nabla' \times \vec{B}_1'}_{=0} \right] + c^2 \vec{B}_1' \left(\underbrace{\nabla' \times \nabla' f'}_{=0} \right) + \partial_{t'} \nabla' f' \cdot \vec{E}_1' = 0 \tag{B.30}$$
$$\implies \partial_{t'} \nabla' f' \cdot \vec{E}_1' = 0$$

The kinematic boundary condition in the laboratory is:

$$\partial_t f + u \partial_x f + v \partial_y f = 0 \tag{B.31}$$

In the co-moving frame S' the kinematic boundary condition takes the form:

$$\partial_{t'} f' = 0 \tag{B.32}$$

Since $u, v = 0$ in S'. This immediately proofs the statement of Eq. B.30 and furthermore, the continuity equation immediately follows from the boundary conditions.

B.8 Additional notes to entropy production

Given the general representation of the laser $\vec{E} = E_0 \vec{\pi}_\varphi$ with the amplitude function $E_0(x,t) : \mathbb{R} \times \mathbb{R}_0^+ \to \mathbb{R}_0^+$ and the polarization vector function $\vec{\pi}_\varphi(x,t) : \mathbb{R} \times \mathbb{R}_0^+ \to \Omega \subset \mathbb{R}^3$ and the set $\Omega = \left\{\vec{v} \in \mathbb{R}^3 : |\vec{v}| \leq 1, x := 0\right\}$, from the electron transverse equation of motion one obtains:

$$\vec{u}_{e,\perp} \approx -\frac{e}{m_e} \int E_0 \vec{\pi}_\varphi dt = -\frac{e}{m_e} \sum_{k=0}^{\infty} (-1)^k \frac{\partial^k E_0}{\partial t^k} \int \vec{\pi}_\varphi dt^{k+1}, \tag{B.33}$$

where integration by parts is used in the last step. The parameter φ determines the polarization and $\varphi = 0$ is linearly and $\varphi = \pm\pi/2$ is a circularly polarized laser. In addition the polarization vector satisfies:

$$\int \vec{\pi}_\varphi dt^k = \frac{(-1)^k}{\omega^{2k}} \frac{\partial^k \vec{\pi}_\varphi}{\partial t^k} \tag{B.34}$$

One obtains:

$$\vec{u}_{e,\perp} \approx \frac{e}{m_e} \sum_{k=0}^{\infty} \frac{1}{\omega^{2k+2}} \frac{\partial^k E_0}{\partial t^k} \frac{\partial^{k+1} \vec{\pi}_\varphi}{\partial t^{k+1}} \tag{B.35}$$

The entropy production Eq. 5.10 is:

$$\partial_\mu \left(s_e u_e^\mu\right) \approx -2e n_e \gamma_e^2 \vec{u}_{e,\perp} \vec{E} = \frac{2e^2 n_e \gamma_e^2}{m_e T_e} E_0 \vec{\pi}_\varphi \sum_{k=0}^{\infty} \frac{1}{\omega^{2k+2}} \frac{\partial^k E_0}{\partial t^k} \frac{\partial^{k+1} \vec{\pi}_\varphi}{\partial t^{k+1}} \tag{B.36}$$

C Evaluation of thermodynamic and gas-dynamic quantities from simulation

C.1 Energy conversion for RPA

A major concern in laser ion acceleration is the transfer of laser energy into particle energy. However, from a microscopic point of view, this energy transfer takes place in the dual- and skin layer structure at the front side of the laser plasma interaction mentioned in the introduction. But since this microscopic structure is not part of the presented model, these processes cannot be accessed directly from the model. To proceed the overall laser energy is calculated and the overall plasma energy (kinetic and thermal) after the acceleration process and relate them via a efficiency parameter C:

$$\int_{-1/2c\tau_L}^{1/2c\tau_L} \frac{2I(x)}{c} dx = C \cdot \left[\int_{-\infty}^{\infty} \left(\frac{1}{2} \rho_\infty u_\infty^2 + p_\infty \right) dx - \int_{-\infty}^{\infty} p_0 dx \right] \tag{C.1}$$

Here, the subscript infinity denotes the evaluation of the density ρ, velocity u, and pressure p after the acceleration process. Unfortunately, exact analytical expressions for ρ, u and p are usually not accessible, thus the evaluation of the integral on the right hand side of Eq. C.1 must be numerically computed. [75] reports a deeper analysis of the transfer of laser energy into the generation of hot electrons and moderately relativistic ions in the dual layer. By applying a relativistic RANKINE-HUGONIOT CONDITION, [75] calculate a general lower and upper band for the energy conversion efficiency as a function of the particle density and laser parameters. To compare the results obtained in this work with [75], the integral in Eq. C.1 is evaluated numerically by using the data previously noted.

For an electron proton plasma with $n_{e0} = 25 n_c$ and $W_{th,e,0} \approx 13\,\mathrm{keV}$ three different laser intensities are compared: $I_{L,thr} \geq 9.4 \cdot 10^{18}\,\mathrm{W/cm^2}$ (see fig. 6.21),

$I_L = 0.2 I_{L,thr}$ (see fig. 6.22) and $I_L = 5 I_{L,thr}$ (see fig. 6.23). In all cases, the laser wavelength is $\lambda = 1\,\mu$m and the initial target thickness is $L = 5\,\mu$m. While the laser has an infinite pulse length, the integration is carried out at the end of the simulation. According to the simulation results, all three cases satisfy the requirement $I_l \lambda_l^2 > 1.3 \cdot 10^{18}\,\mathrm{Wcm^{-2}}\mu\mathrm{m}^2$, giving the absorption bounds of $0.012 \leq f_1 \leq 0.872$, $0.0054 \leq f_2 \leq 0.362$ and $0.03 \leq f_3 \leq 0.975$. From the simulation, one obtains an absorption efficiency $C_1 \approx 0.017$, $C_2 \approx 0.048$ and $C_3 \approx 0.04$, respectively. All absorption coefficients C_k fit well within the bounds predicted by [75]. Furthermore, one obtains that the energy transfer is of the same order of magnitude in all cases, but one notices that the energy conversion is only a few percent. Note that the energy transfer is relatively high for the lowest laser intensity, where no shock acceleration occurs. This fact is explained by the components of the electrons' and ions' energy separately. In case of the $I_{L,thr} \geq 9.4 \cdot 10^{18}\,\mathrm{W/cm^2}$ laser, the ions' contribution to the transfer coefficient is $C_{1,i} \approx 0.011$ where the electrons' contribution is $C_{1,e} \approx 0.007$. For the strong laser with $I_L = 5 I_{L,thr}$ the contributions are $C_{1,i} \approx 0.039$ and $C_{1,e} \approx 0.0007$, respectively, which is of the same order as for the moderate laser. In both cases, the fraction of the laser energy transferred to the ions is much larger than the fraction of energy transferred to the electrons and this disparity increases with increasing laser intensity. While this effect may seem typical for RPA generated beams, considering the weak laser with $I_L = 0.2 I_{L,thr}$, the energy fractions are $C_{1,i} \approx 0.015$ and $C_{1,e} \approx 0.034$, where the fraction of the laser energy transferred to the electrons is higher than the energy transferred to the ions, contrary to the two other cases. This is expected for $I_L < I_{thr}$, since the energy transfer to the electrons is dominant in a laser radiation pressure driven dilution wave.

C.2 Evaluation of the laser piston and the shock from simulation data

To obtain the piston motion and the shock wave from the numerical results of the 1D PIC simulation, a piecewise fitting is performed as follows: In the first step, a smooth density function of the plasma is generated. This curve is then subdivided into several mesh points (see fig. C.1) with coordinates $(x_i, f(x_i))$. The spatial distance between two points $\delta = x_{i+1} - x_i$ is fixed. Afterwards the slope of each secant between two mesh points is calculated: $m_i = f(x_{i+1}) - f(x_i)/\delta$. The maximum of this list of slopes corresponds to the piston position, whereas the minimum (maximum negative value) corresponds to the shock. This way one can follow the piston and shock in time (see fig. C.2).

Finally, a straight line is fitted to the curves in fig. C.2 and by that one obtains the piston path and shock wave trajectory.

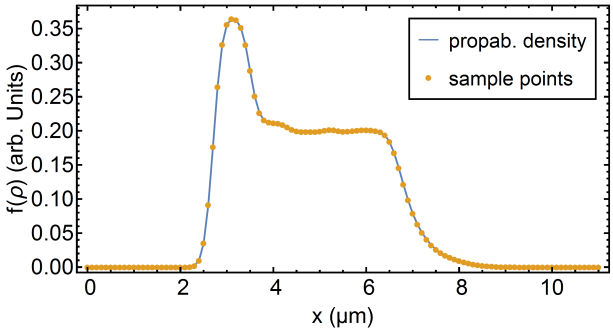

Figure C.1.: Probability density function (blue line) of the plasma and mesh points (orange points) for the evaluation of the slope.

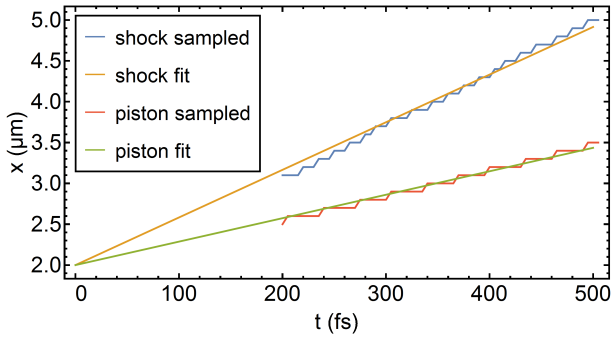

Figure C.2.: Piston path and shock wave trajectory from the numerical evaluation , as well as a fit line.

C.3 Evaluation of the initial plasma temperature from PIC simulation

The initial electron temperature (plasma temperature) is a crucial parameter for the radiation pressure acceleration. To apply the obtained scaling laws from chapter 6.3 it is therefore necessary to evaluate the electron temperature in advance. Typically, one sets the electron temperature in a PIC simulation by an appropriate velocity distribution for the electron species. However, the desired electron temperature may change over the first simulation time steps due to the finite resolution of the mesh grid, the interpolation order used for the field interpolation, interaction with the ion species and other effects. It is therefore essential to determine the

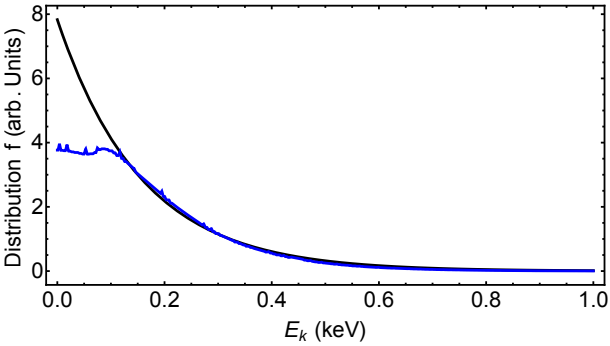

Figure C.3.: Evaluation of the initial electron temperature in simulation: The electron kinetic energy distribution is fitted with a Boltzmann distribution.

plasma temperature from the PIC simulation for the comparison with the analytic model. This determination is done as follows: From the simulation electron particle data the kinetic energy distribution $f = f(W_k^e)$ is calculated, as shown in fig. C.3. Then, one fits a BOLTZMANN DISTRIBUTION of the form $f(W_k^e) = f_0 \exp(-W_k^e / k_B T_e)$ to the numerical distribution, where f_0 and T_e are the fit parameters, see fig. C.3. With this done, one obtains the approximate electron temperature T_e. For the example shown in fig. C.3 one obtains an electron temperature of $W_{th}^e \approx 6.4\,\mathrm{keV}$.

C.4 Evaluation of the divergence angle from PIC simulation

Obtaining the divergence angle of the plasma sheet from the 2D PIC simulation is challenging. The procedure follows two steps: In the first step, a Gaussian curve is fitted to the particle distribution obtained from the simulation, as shown in fig. C.4a. From the Gaussian fit the position of the infliction point (x_{ip}, y_{ip}) is determined. Subsequently, a circle with center (x_{ip}, y_{ip}) and radius δr is plotted on top of the particle distribution (cf. fig. C.4b). The set of particle that are within the circle is: $\Omega = \left\{(x_j, y_j) \in \mathbb{R}^2 : (x_j - x_{ip})^2 + (y_j - y_{ip})^2 \leq \delta r\right\}$, with j being the particle index.

Finally the divergence angle of the plasma is identified as the average divergence of the particles within the circle:

$$\vartheta = \frac{1}{N} \sum_{j=1}^{N} \vartheta_j, \tag{C.2}$$

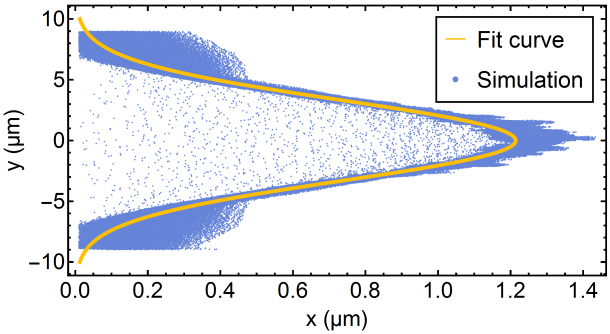

(a) Fit curve and particles from simulation.

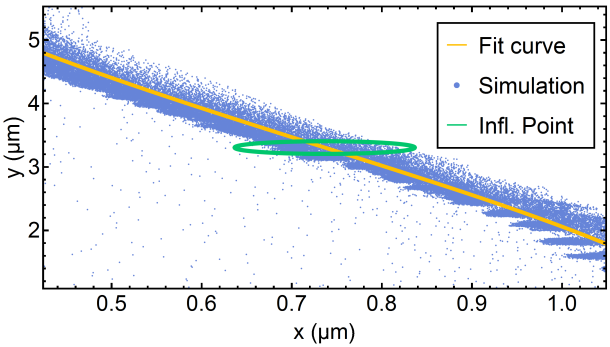

(b) Circle around infliction point.

Figure C.4.: Evaluation of the divergence angle: A Gaussian curve is fitted to the particle distribution from the simulation. The infliction point is determined. A circle around the infliction point encloses the particles contributing to the divergence.

with $N \in \mathbb{N}$ being the number of elements in the set Ω and the divergence of a particle in the set of Ω:

$$\vartheta_j = \arctan \frac{v_j}{u_j} \tag{C.3}$$

For this procedure, the circle's radius δr is chosen such that is at least as large as the width of the plasma sheet.

C.5 Neutrality of the emerging plasma

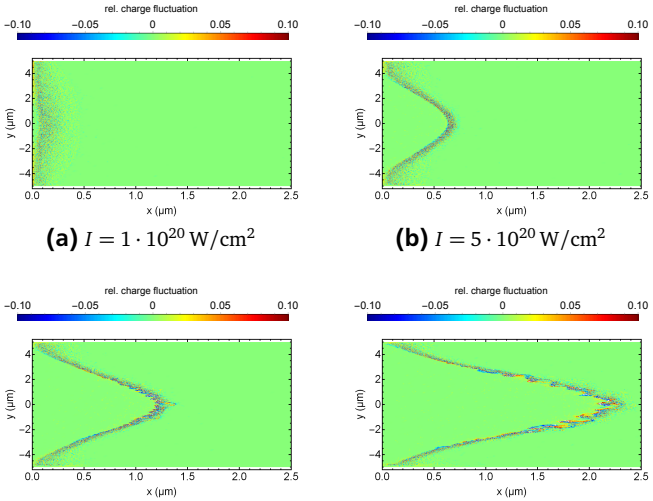

(a) $I = 1 \cdot 10^{20}\,\mathrm{W/cm^2}$ **(b)** $I = 5 \cdot 10^{20}\,\mathrm{W/cm^2}$

(c) $I = 1 \cdot 10^{21}\,\mathrm{W/cm^2}$ **(d)** $I = 2 \cdot 10^{21}\,\mathrm{W/cm^2}$

Figure C.5.: Relative charge density (color) $Zn_i - n_e/n_{e,0}$ as a function of x and y at $t = 142.5\,\mathrm{fs}$ for different laser intensities.

In this section, the neutrality of the plasma emerging while the RPA is examined. For this purpose, the charge fluctuation in the four simulations presented in chapter 7.1.2 is exemplary examined. Figure C.5 shows a density plot of the relative charge fluctuation $Zn_i - n_e/n_{e,0}$ after the acceleration process. As indicated in fig. C.5a and C.5b, the charge fluctuation is randomly distributed and small, that is $Zn_i - n_e \ll n_{e,0}$ for the lower intensities. Thus this is a quasi neutral plasma, in accordance with the definition in chapter 2.1.

However, as clarified by fig. C.5c and C.5d, the Rayleigh Taylor Instability (RTI) is amplified by higher intensities and leads to an increase of the charge density and the emerging of charge separation layers. The RTI emerges between the electron gas and the ion gas and thus separates both. With the help of the CFM, derived in chapter 3.3.3 this can be investigated in more detail: From Eq. 3.60, one obtains the surface charge density:

$$\sigma_s \approx \epsilon_0 \partial_y h E_{1y} (1 - u_x/c) \tag{C.4}$$

Where $x = h(y,t)$ denotes the surface function, u_x is the longitudinal surface velocity and E_{1y} is the y-component of the electrical field. The RTI causes surface turbulence that leads to large surface slopes $\partial_y h$ and according to Eq. C.4, to an increase of the surface charge σ_s. Nevertheless, with increasing velocity u_x the surface charge will decrease and in case the external field E_{1y} vanishes, the surface charge σ_s will also vanish. Hence, one can expect, that the charge separation will disappear after a certain distance of flight.

List of Figures

List of Tables

Glossary

All units are given in SI (Systéme international d'unités). Arrows denote 3D vector quantities, quantities without arrows are the related absolute values. A quantity evaluated in a moving reference frame is labeled with a prime. Four-vector quantities are given in 4-vector notation with Greek indices running from $\alpha, \beta, ... = 0, 1, 2, 3$, whereas the index k is a species index, e.g. $k = e, i$ for electrons or protons, respectively. The index 0 denotes the initial or equilibrium state value of a quantity. Directional components are indexed with $\perp$for perpendicular components and $\parallel$ for parallel components with respect to the propagation direction of the plasma. Derivatives are written in abbreviated form, e.g. $d_t = d/dt$ is the total time derivative, $\partial_t = \partial/\partial t$ is the partial derivative with respect to time.

Term	**Unit**	**Description**
λ	μm	Laser wavelength
L	nm	Thickness of the plasma sheet/slab
λ_D	nm	General Debye Length
λ_{De}	nm	Electron Debye Length
δ	m	Penetration depth of a given EM wave into a plasma
d	nm	Size of the electron ion dual layer
l	m	Characteristic length of the problem, given by intrinsic or boundary scales, or as an external quantity
λ_c	m	Width of the EM shock
λ_{a0}	m	Width of the material shock
$k = \lvert\vec{k}\rvert$	m^{-1}	Wave number of the EM wave
τ_L	fs	Laser pulse duration
ω	s^{-1}	Laser angular frequency
ω_{pe}	s^{-1}	Electron plasma frequency
τ_{relax}	s	Electron relaxation time, related to electron plasma frequency $\tau_{relax} \propto \omega_{pe}^{-1}$
T	s	Characteristic time of the problem, given by intrinsic or boundary scales, or as an external quantity

Term	Unit	Description
ν_{ee}, ν_{ei}, ν_{ii}	Hz	Electron-electron-, electron-ion- and ion-ion collision frequency
$s_k(\vec{x},t)$	JK^{-1}	Entropy density of species k
$p_k(\vec{x},t)$	Nm^{-2}	Pressure of species k
$p(\vec{x},t)$	Nm^{-2}	Pressure of neutral plasma
$e_{0,k}$	J	Specific thermal energy of a fluid particle of species k: For ideal gases $e_{0,k} = f/2k_BT_k$
a_0	ms^{-1}	Isentropic speed of sound in state of rest for ion acoustic waves
a_e	ms^{-1}	Isentropic speed of sound for electron acoustic waves
$\varkappa$		Isentropic index of the neutral plasma: $\varkappa = (f+2)/f$
$\varkappa_e$		Isentropic index of the electrons
T_e	K	Electron temperature
T_i	K	Ion temperature
E_F	J	Electron's FERMI ENERGY: $E_F = \hbar^2(3\pi^2 n_e)^{2/3}/2m_e$
f		Degrees of freedom of a particle species
M_c		Mach-number of the plasma with respect to c: $M_c = a_0/c$
$\varpi_{th,k}$	Jm^{-3}	Thermal energy density of the species k: $\varpi_{th,k} = n_{0,k}e_{0,k}$
κ		Plasma compression factor: $\kappa = \rho/\rho_0$
κ_e		Compression factor of the electron gas: $\kappa_e = n_e/n_{e,0}$
$I(\vec{x},t)$	Wcm^{-2}	Laser intensity
W_{EM}	J	Energy of the electromagnetic field
$\rho_{el}(\vec{x},t)$	Cm^{-3}	Charge density of the plasma: $\rho_{el} = Zen_i - en_e$
$\vec{j}(\vec{x},t)$	Am^{-2}	Current density of the plasma: $\vec{j} = \vec{j}_e + \vec{j}_i$
$\vec{j}_e(\vec{x},t)$	Am^{-2}	Electron current density: $\vec{j}_e = -en_e\vec{u}_e$
$\vec{j}_i(\vec{x},t)$	Am^{-2}	Ion current density: $\vec{j}_i = Zen_i\vec{u}_i$
$\vec{S}(\vec{x},t)$	Wm^{-2}	Poynting vector of the electromagnetic wave
$\vec{\pi}_\varphi$	Wm^{-2}	Parametric polarization vector of the electromagnetic wave: $\varphi = 0 \rightarrow \mathrm{LP}, \varphi = \pm\pi/2 \rightarrow \mathrm{CP}$
w_0	m	Beam waist of the laser beam at focal spot
$E_0(\vec{x},t)$	Vm^{-1}	Amplitude of the electric field

Term	Unit	Description
$\vec{H}(\vec{x},t)$	Am^{-1}	Magnetic field strength
$\vec{B}(\vec{x},t)$	T	Magnetic flux density
$\vec{D}(\vec{x},t)$	Cm^{-2}	Electric displacement field
$\vec{E}(\vec{x},t)$	Vm^{-1}	Electric field strength
$p_L(\vec{x},t)$	Nm^{-2}	Radiation pressure of the laser
$\sigma_s(\vec{x},t)$	Cm^{-2}	Surface charge on the material interface of the plasma sheet
$\vec{j}_s(\vec{x},t)$	Am^{-2}	Surface current on the material interface of the plasma sheet
$I_0,\ I_L$	Wcm^{-2}	Laser peak intensity
$\vec{\varepsilon}(\vec{x},t)$		Dimensionless electric field, normalized with E_0
$\vec{\beta}(\vec{x},t)$		Dimensionless magnetic field, normalized with E_0/c
$R(\omega,L)$		Reflective index as a function of the EM wave frequency ω and the plasma slab width L
ϖ_{EM}	Jm^{-3}	Energy density of the EM field: $\varpi_{EM} = \epsilon_0 E_0^2$
ε_L	Jm^{-2}	Areal energy density of the laser
$\hat{F}_k^{x,y,z}$		Fourier transformed of the x,y,z component of the electric field in region k
$\underline{\underline{T}}$	Jm^{-2}	Maxwell stress tensor of the EM field in 3D
α	deg	Angle of incidence between laser propagation and plasma surface normal
a,b,c	m^{-1}	Laser focal spot width parameters for different spot envelopes
σ_y	m	Half transverse expansion of the laser focal spot for Gaussian beams
ϕ	V	Electrostatic potential
$\hat{k} = \vec{k}/\lvert\vec{k}\rvert$	m^{-1}	Unit wave-vector of the electromagnetic wave
$\hat{n}(\vec{x},t), \hat{t}(\vec{x},t)$		Normal- and tangential unit vector of the plasma material interface
$f(x,y,t)=0$		function describing the material interface of the plasma sheet; Equivalent representation: $f = x - h(y,t) = 0$
$\mathbb{C}$		Set of the complex numbers
$\mathbb{R}^n$		Real space of dimension n, with $n \in \mathbb{N}$
$\mathbb{N}$		Set of the integer numbers
$\mathbb{M}^4$		Minkowski Space

Term	Unit	Description
δ_{ij}		Kronecker Delta: $i = j: \ \delta_{ij} = 1, i \neq j: \ \delta_{ij} = 0$ with $i, j \in \mathbb{N}$
$\delta(x)$		Dirac Delta distribution: $\delta(0) = 1, \delta(x) = 0, x \neq 0$
tr(.)		Trace of a tensor
ε		Small parameter: $\varepsilon \ll 1$
$\vec{\xi} = (\xi, \eta)^T$		Dimensionless length, normalized by an inner or outer length scale
τ		Dimensionless time, normalized by an inner or outer time scale
∇_ξ		Nabla operator with respect to the dimensionless coordinates $\vec{\xi}$
$\vec{e}_{x,y,z}$		Unit vector into x, y, z direction
$\vec{e}_{\phi,r}$		Unit vector into ϕ, r direction in cylindrical coordinates
$\vec{u}$	ms^{-1}	Barycentric velocity of the neutral plasma: $\vec{u} = (\rho_i \vec{u}_i + \rho_e \vec{u}_e)/(\rho_i + \rho_e)$
$\vec{u}_e$	ms^{-1}	Barycentric velocity of the electrons
$\vec{u}_i$	ms^{-1}	Barycentric velocity of the ions
$\vec{v}(\vec{x}, t)$		Dimensionless velocity, normalized with c
$\vec{l}_{e,i,EM}(\vec{x}, t)$	Nm^{-2}	Angular momentum density of the electrons (e), ions (i) or EM wave (EM)
δX	arb.units	Small perturbation of a quantity X with respect to its equilibrium or rest state X_0
$\tilde{X}$	arb.units	Dimensionless representation of a quantity X normalized to its equilibrium or rest state X_0
u, v, w	ms^{-1}	Components of the velocity in x, y, z direction
ρ	kgm^{-3}	Mass density of the neutral plasma: $\rho = \rho_e + \rho_i$
ρ_e	kgm^{-3}	Electron mass density: $\rho_e = n_e m_e$
ρ_i	kgm^{-3}	Ion mass density: $\rho_i = n_i m_i$
μ	kgm^{-2}	Areal mass density of the neutral plasma: $\mu = \rho L$
$\bar{Z}$		Average charge state in the plasma
$\bar{W}_i$	eV	Average ionization energy of the plasma atoms
W_{kin}	eV	Kinetic energy of the plasma
m_i	kg	Plasma ion mass
Z		Plasma ion charge state/charge number

Term	Unit	Description
N_D		Plasma parameter: Number of electrons in a Debye sphere
n_c	m^{-3}	Critical electron number density with respect to a given laser frequency ω
n_A	m^{-3}	Number density of the neutral atoms
$n_e(\vec{x},t)$	m^{-3}	Electron number density
$n_i(\vec{x},t)$	m^{-3}	Ion number density
u_p	ms^{-1}	Velocity of the laser piston
x_p	m	Position of the laser piston
u_s	ms^{-1}	Velocity of the shock wave
x_s	m	Position of the shock wave
$\vec{L}_{e,i,EM}(\vec{x},t)$	$\mathrm{N}\times\mathrm{m}$	Angular momentum of the electrons (e), ions (i) or EM wave (EM)
ϖ_0	Jm^{-3}	Rest energy density of the plasma: $\varpi_0 = \rho_0 c^2$
E_k	Jkg^{-1}	Energy density of a particle of species k: $E_k = e_{0,k}/m_k + 1/2u_k^2$
A_0		Dimensionless acceleration parameter of the plasma
$f_k(\varpi_{kin}, y)$		Kinetic energy probability density with respect to the transverse coordinate y
x_f	m	Position of the plasma front in longitudinal direction
r	m	Mean beam radius of the emerging plasma
C_k		Energy transfer efficiency from the laser into kinetic energy of species k
ϑ	deg	Divergence angle of the emerging plasma
$T_k^{\alpha\beta}$	Nm^{-2}	Four-energy-stress tensor of species k, with coordinate indices $\alpha,\beta = 0,1,2,3$
$F^{\alpha\beta}$	T	Four-Field-strength tensor, with coordinate indices $\alpha,\beta = 0,1,2,3$
$\varepsilon^{\alpha\beta\gamma}$		Levi-Civita pseudo tensor, with coordinate indices $\alpha,\beta,\gamma = 0,1,2,3$
$g^{\mu\nu}, g_{\mu\nu}$		Co- and contra-variant metric tensor, with coordinate indices $\mu,\nu = 0,1,2,3$
$\eta^{\alpha\beta}, \eta_{\alpha\beta}$		Co- and contra-variant Minkowski Tensor, with coordinate indices $\alpha,\beta = 0,1,2,3$: $\eta_{\alpha\beta} = \mathrm{diag}(1,-1,-1,-1)$

Term	Unit	Description
$\|g\|$		Absolute value of the determinant of the metric tensor $\det(g^{\mu\nu}) = g$, with coordinate indices $\mu, \nu = 0, 1, 2, 3$
j_k^α	Am^{-2}	Four-current density of species k, coordinate indices $\alpha = 0, 1, 2, 3$: $j_k^\alpha = \gamma_k \rho_{el}(c, \vec{u}_k)^T$
ds	m	Line element in four dimensional space time
τ	s	Eigen-time in a reference frame: $d\tau = ds/c$
Λ_β^α		Lorentz-transformation tensor, with coordinate indices $\alpha, \beta = 0, 1, 2, 3$
α_ν^μ		Transformation tensor for general coordinate transformation, with coordinate indices $\mu, \nu = 0, 1, 2, 3$: $\alpha_\nu^\mu = \partial x'^\mu / \partial x^\nu$
$\beta = u/c$		Relativistic factor
γ		Lorentz factor: $\gamma = (1 - \beta^2)^{-1/2}$
γ_0		Average Lorentz factor
$h_{\mu\nu}$		Perturbation metric tensor, with coordinate indices $\mu, \nu = 0, 1, 2, 3$: $g_{\mu\nu} \approx \eta_{\mu\nu} + h_{\mu\nu}$
λ_ν^μ		Perturbation from Lorentz transformation, with coordinate indices $\mu, \nu = 0, 1, 2, 3$: $\alpha_\nu^\mu \approx \Lambda_\nu^\mu + \lambda_\nu^\mu$

Physical constants

Term	Unit	Description
k_B	JK^{-1}	Boltzmann constant: $k_B \approx 1.38065 \cdot 10^{-23}\,\mathrm{JK}^{-1}$
ϵ_0	Fm^{-1}	Vacuum permittivity: $\epsilon_0 \approx 8.85419 \cdot 10^{-12}\,\mathrm{Fm}^{-1}$
μ_0	NA^{-2}	Vacuum permeability: $\mu_0 = 4\pi \cdot 10^{-7}\,\mathrm{NA}^{-2}$
c	ms^{-1}	Vacuum speed of light: $c \approx 299,792,458\,\mathrm{ms}^{-1}$
e	C	Elementary charge: $e \approx 1.602177 \cdot 10^{-19}\,\mathrm{C}$
m_e	kg	Electron rest mass: $m_e \approx 9.109 \cdot 10^{-31}\,\mathrm{kg}$
$\hbar$	Js	Reduced Planck constant: $\hbar \approx 1.0546 \cdot 10^{-34}\,\mathrm{Js}$
e		Euler number: $\mathrm{e} \approx 2.718282$
π		Mathematical constant, ratio of circumference and diameter of a circle: $\pi \approx 3.14159$
$i = \sqrt{-1}$		Imaginary unit

Acronyms

CPA	Chirped Pulse Amplification
RPA	Radiation Pressure Acceleration
LP	Linearly Polarized, Linear Polarization
CP	Circularly Polarized, Circular Polarization
TNSA	Target Normal Sheath Acceleration
DPEFA	Dual-Peaked Electrostatic-Field Acceleration
BOA	Break-Out Afterburner
JuSPARC	Jülich Short-Pulsed pArticle and Radiation Center
JETI40	Jenaer Titan:Saphir 40 Terawatt Laser
PIC	Particle In Cell
VSim	VSim - Name of the simulation software packes used
RTI	Rayleigh Taylor Instability
EM	Electromagnetic
1D,2D,3D	one-, two- or three dimensional
CFL	Courant-Friedrichs-Lewy Condition
LIF	Laser induced Focusing
PDE	Partial Differential Equation

MHD	Magneto-Hydrodynamic
CFM	Current Flag Model
ECFM	Extended Current Flag Model
FDTD	Finite Difference Time Domain Method
GPU	Graphic Processor Unit
PPC	Particles Per Cell
HR	High Resolution simulation
LR	Low Resolution simulation

Bibliography

[1] J. Schreiber, F. Bell, F. Grüner, U. Schramm, M. Geissler, M. Schnürer, S. Ter-Avetisyan, B. M. Hegelich, J. Cobble, E. Brambrink, J. Fuchs, P. Audebert, and D. Habs, "Analytical model for ion acceleration by high-intensity laser pulses," *Physical Review Letters*, vol. 97, no. 4, 2006.

[2] D. Strickland and G. Mourou, "Compression of amplified chirped optical pulses," *Optics Communications*, vol. 56, no. 3, pp. 219–221, 1985.

[3] B. Aurand, S. Kuschel, O. Jäckel, C. Rödel, H. Y. Zhao, S. Herzer, a. E. Paz, J. Bierbach, J. Polz, B. Elkin, G. G. Paulus, a. Karmakar, P. Gibbon, T. Kuehl, and M. C. Kaluza, "Radiation pressure-assisted acceleration of ions using multi-component foils in high-intensity laser-matter interactions," *New Journal of Physics*, vol. 15, p. 033031, 2013.

[4] B. Aurand, S. Kuschel, O. Jäckel, C. Rödel, H. Y. Zhao, S. Herzer, A. E. Paz, J. Bierbach, J. Polz, B. Elkin, A. Karmakar, P. Gibbon, M. C. Kaluza, and T. Kuehl, "Enhanced radiation pressure-assisted acceleration by temporally tuned counter-propagating pulses," *Nuclear Instruments and Methods in Physics Research, Section A: Accelerators, Spectrometers, Detectors and Associated Equipment*, vol. 740, pp. 83–86, 2014.

[5] S. Busold, D. Schumacher, O. Deppert, C. Brabetz, S. Frydrych, F. Kroll, M. Joost, H. Al-Omari, a. Blažević, B. Zielbauer, I. Hofmann, V. Bagnoud, T. E. Cowan, and M. Roth, "Focusing and transport of high-intensity multi-MeV proton bunches from a compact laser-driven source," *Physical Review Special Topics - Accelerators and Beams*, vol. 16, p. 101302, 2013.

[6] P. Mora, "Thin-foil expansion into a vacuum," *AIP Conference Proceedings*, vol. 827, no. May, pp. 227–236, 2006.

[7] Z. Lécz, O. Boine-Frankenheim, and V. Kornilov, "Target normal sheath acceleration for arbitrary proton layer thickness," 2013.

[8] A. Macchi, M. Borghesi, and M. Passoni, "Ion acceleration by superintense laser-plasma interaction," *Reviews of Modern Physics*, vol. 85, no. 2, pp. 751–793, 2013.

[9] M. Roth, T. E. Cowan, M. H. Key, S. P. Hatchett, C. Brown, W. Fountain, J. Johnson, D. M. Pennington, R. A. Snavely, S. C. Wilks, K. Yasuike, H. Ruhl, F. Pegoraro, S. V. Bulanov, E. M. Campbell, M. D. Perry, and H. Powell, "Fast ignition by intense laser-accelerated proton beams," *Physical Review Letters*, vol. 86, pp. 436–439, 2001.

[10] M. Roth, D. Jung, K. Falk, N. Guler, O. Deppert, M. Devlin, A. Favalli, J. Fernandez, D. Gautier, M. Geissel, R. Haight, C. E. Hamilton, B. M. Hegelich, R. P. Johnson, F. Merrill, G. Schaumann, K. Schoenberg, M. Schollmeier, T. Shimada, T. Taddeucci, J. L. Tybo, F. Wagner, S. A. Wender, C. H. Wilde, and G. A. Wurden, "Bright laser-driven neutron source based on the relativistic transparency of solids," *Physical Review Letters*, vol. 110, p. 044802, 2013.

[11] E. Esarey, C. B. Schroeder, and W. P. Leemans, "Physics of laser-driven plasma-based electron accelerators," *Reviews of Modern Physics*, vol. 81, no. 3, pp. 1229–1285, 2009.

[12] C. G. R. Geddes, C. S. Toth, J. Van Tilborg, E. Esarey, C. B. Schroeder, D. Bruhwiler, C. Nieter, J. Cary, and W. P. Leemans, "High-quality electron beams from a laser wakefield accelerator using plasma-channel guiding.," *Nature*, vol. 431, no. 7008, pp. 538–541, 2004.

[13] S. Busold, A. Almomani, V. Bagnoud, W. Barth, S. Bedacht, A. Blažević, O. Boine-Frankenheim, C. Brabetz, T. Burris-Mog, T. E. Cowan, O. Deppert, M. Droba, H. Eickhoff, U. Eisenbarth, K. Harres, G. Hoffmeister, I. Hofmann, O. Jaeckel, R. Jaeger, M. Joost, S. Kraft, F. Kroll, M. Kaluza, O. Kester, Z. Lecz, T. Merz, F. Nürnberg, H. Al-Omari, A. Orzhekhovskaya, G. Paulus, J. Polz, U. Ratzinger, M. Roth, G. Schaumann, P. Schmidt, U. Schramm, G. Schreiber, D. Schumacher, T. Stoehlker, A. Tauschwitz, W. Vinzenz, F. Wagner, S. Yaramyshev, and B. Zielbauer, "Shaping laser accelerated ions for future applications - The LIGHT collaboration," *Nuclear Instruments and Methods in Physics Research, Section A: Accelerators, Spectrometers, Detectors and Associated Equipment*, vol. 740, pp. 94–98, 2014.

[14] S. Busold, D. Schumacher, O. Deppert, C. Brabetz, F. Kroll, A. Blažević, V. Bagnoud, and M. Roth, "Commissioning of a compact laser-based proton beam line for high intensity bunches around 10 MeV," *Physical Review Special Topics - Accelerators and Beams*, vol. 17, p. 031302, 2014.

[15] J. Fuchs, P. Antici, E. D'Humiéres, E. Lefebvre, M. Borghesi, E. Brambrink, C. A. Cecchetti, M. Kaluza, V. Malka, M. Manclossi, S. Meyroneinc, P. Mora,

J. Schreiber, T. Toncian, H. Pépin, and P. Audebert, “Laser-driven proton scaling laws and new paths towards energy increase,” 2006.

[16] M. Passoni, L. Bertagna, and A. Zani, “Target normal sheath acceleration: Theory, comparison with experiments and future perspectives,” *New Journal of Physics*, vol. 12, p. 045012, 2010.

[17] T. Ceccotti, A. Lévy, F. Réau, H. Popescu, P. Monot, E. Lefebvre, and P. Martin, “TNSA in the ultra-high contrast regime,” 2008.

[18] A. Diaw and P. Mora, “Rarefaction shock in plasma with a bi-Maxwellian electron distribution function,” *Physical Review E - Statistical, Nonlinear, and Soft Matter Physics*, vol. 84, p. 036402, 2011.

[19] J. Schreiber, F. Bell, and Z. Najmudin, “Optimization of relativistic laser-ion acceleration,” *High Power Laser Science and Engineering*, vol. 2, no. 2014, p. e41, 2014.

[20] H. Schwoerer, S. Pfotenhauer, O. Jäckel, K.-U. Amthor, B. Liesfeld, W. Ziegler, R. Sauerbrey, K. W. D. Ledingham, and T. Esirkepov, “Laser-plasma acceleration of quasi-monoenergetic protons from microstructured targets,” *Nature*, vol. 439, pp. 445–448, 2006.

[21] T. E. Cowan, J. Fuchs, H. Ruhl, A. Kemp, P. Audebert, M. Roth, R. Stephens, I. Barton, A. Blazevic, E. Brambrink, J. Cobble, J. Fernández, J.-C. Gauthier, M. Geissel, M. Hegelich, J. Kaae, S. Karsch, G. P. L. Sage, S. Letzring, M. Manclossi, S. Meyroneinc, A. Newkirk, H. Pépin, and N. Renard-LeGalloudec, “Ultralow Emittance, Multi-MeV Proton Beams from a Laser Virtual-Cathode Plasma Accelerator,” *Physical Review Letters*, vol. 92, p. 204801, 2004.

[22] D. Neely, P. Foster, A. Robinson, F. Lindau, O. Lundh, A. Persson, C.-G. Wahlstrømm, and P. McKenna, “Enhanced proton beams from ultrathin targets driven by high contrast laser pulses,” *Applied Physics Letters*, vol. 89, p. 021502, 2006.

[23] A. J. Mackinnon, Y. Sentoku, P. K. Patel, D. W. Price, S. Hatchett, M. H. Key, C. Andersen, R. Snavely, and R. R. Freeman, “Enhancement of Proton Acceleration by Hot-Electron Recirculation in Thin Foils Irradiated by Ultraintense Laser Pulses,” *Physical Review Letters*, vol. 88, p. 215006, 2002.

[24] E. L. Clark, K. Krushelnick, M. Zepf, F. N. Beg, M. Tatarakis, A. Machacek, M. I. K. Santala, I. Watts, P. A. Norreys, and A. E. Dangor, "Energetic Heavy-Ion and Proton Generation from Ultraintense Laser-Plasma Interactions with Solids," *Physical Review Letters*, vol. 85, p. 1654, 2000.

[25] A. V. Korzhimanov, E. S. Efimenko, S. V. Golubev, and A. V. Kim, "Generating high-energy highly charged ion beams from petawatt-class laser interactions with compound targets," *Physical Review Letters*, vol. 109, p. 245008, 2012.

[26] B. Eliasson, C. S. Liu, X. Shao, R. Z. Sagdeev, and P. K. Shukla, "Laser acceleration of monoenergetic protons via a double layer emerging from an ultra-thin foil," *New Journal of Physics*, vol. 11, p. 073006, July 2009.

[27] M. Chen, N. Kumar, A. Pukhov, and T. P. Yu, "Stabilized radiation pressure dominated ion acceleration from surface modulated thin-foil targets," *Physics of Plasmas*, vol. 18, no. 7, 2011.

[28] H. B. Zhuo, Z. L. Chen, W. Yu, Z. M. Sheng, M. Y. Yu, Z. Jin, and R. Kodama, "Quasimonoenergetic Proton Bunch Generation by Dual-Peaked Electrostatic-Field Acceleration in Foils Irradiated by an Intense Linearly Polarized Laser," *Physical Review Letters*, vol. 105, p. 065003, 2010.

[29] A. P. L. Robinson, R. M. G. M. Trines, N. P. Dover, and Z. Najmudin, "Hole-boring radiation pressure acceleration as a basis for producing high-energy proton bunches," *Plasma Physics and Controlled Fusion*, vol. 54, no. 11, p. 115001, 2012.

[30] B. Qiao, M. Zepf, M. Borghesi, B. Dromey, M. Geissler, A. Karmakar, and P. Gibbon, "Radiation-pressure acceleration of ion beams from nanofoil targets: The leaky light-sail regime," *Physical Review Letters*, vol. 105, no. 15, 2010.

[31] A. P. L. Robinson, M. Zepf, S. Kar, R. G. Evans, and C. Bellei, "Radiation pressure acceleration of thin foils with circularly polarized laser pulses," *New Journal of Physics*, vol. 10, p. 013021, 2008.

[32] S. G. Rykovanov, J. Schreiber, J. Meyer-ter Vehn, C. Bellei, A. Henig, H. C. Wu, and M. Geissler, "Ion acceleration with ultra-thin foils using elliptically polarized laser pulses," *New Journal of Physics*, vol. 10, p. 113005, 2008.

[33] N. P. Dover and Z. Najmudin, "Ion acceleration in the radiation pressure regime with ultrashort pulse lasers," *High Energy Density Physics*, vol. 8, pp. 170–174, 2012.

[34] S. C. Wilks, A. B. Langdon, T. E. Cowan, M. Roth, M. Singh, S. Hatchett, M. H. Key, D. Pennington, A. MacKinnon, and R. A. Snavely, "Energetic proton generation in ultra-intense laser-solid interactions," *Physics of Plasmas*, vol. 8, pp. 542–549, 2001.

[35] T. Esirkepov, M. Borghesi, S. V. Bulanov, G. Mourou, and T. Tajima, "Highly efficient relativistic-ion generation in the laser-piston regime," *Physical Review Letters*, vol. 92, no. 17, p. 175003, 2004.

[36] A. Macchi, F. Cattani, T. V. Liseykina, and F. Cornolti, "Laser acceleration of ion bunches at the front surface of overdense plasmas," *Physical Review Letters*, vol. 94, p. 165003, 2005.

[37] A. Macchi, S. Veghini, T. V. Liseykina, and F. Pegoraro, "Radiation pressure acceleration of ultrathin foils," *New Journal of Physics*, vol. 12, p. 045013, 2010.

[38] A. Macchi, S. Veghini, and F. Pegoraro, "light sail acceleration reexamined," *Physical Review Letters*, vol. 103, p. 085003, 2009.

[39] A. Macchi, "Theory of light sail acceleration by intense lasers: an overview," *High Power Laser Science and Engineering*, vol. 2, no. 2014, p. e10, 2014.

[40] B. Qiao, M. Geissler, S. Kar, M. Borghesi, and M. Zepf, "Stable ion radiation pressure acceleration with intense laser pulses," *Plasma Physics and Controlled Fusion*, vol. 53, no. 12, p. 124009, 2011.

[41] B. M. Hegelich, B. J. Albright, J. Cobble, K. Flippo, S. Letzring, M. Paffett, H. Ruhl, J. Schreiber, R. K. Schulze, and J. C. Fernández, "Laser acceleration of quasi-monoenergetic MeV ion beams.," *Nature*, vol. 439, pp. 441–444, 2006.

[42] I. Kim, K. Pae, C. Kim, and H. Kim, "Towards radiation pressure acceleration of protons using linearly polarized ultrashort petawatt laser pulses," *arXiv preprint arXiv: ...*, 2013.

[43] I. J. Kim, K. H. Pae, C. M. Kim, H. T. Kim, C.-l. Lee, I. W. Choi, H. Singhal, J. H. Sung, S. K. Lee, H. W. Lee, and P. V. Nickles, "New frontier of laser particle acceleration : driving protons to 80 MeV by radiation pressure," *arXiv.org*, no. 1411.5734, 2014.

[44] S. Kar, K. F. Kakolee, B. Qiao, A. Macchi, M. Cerchez, D. Doria, M. Geissler, P. Mckenna, D. Neely, J. Osterholz, R. Prasad, K. Quinn, B. Ramakrishna, G. Sarri, O. Willi, X. Y. Yuan, M. Zepf, and M. Borghesi, "Ion Acceleration in Multispecies Targets Driven by Intense Laser Radiation Pressure," *Physical Review Letters*, vol. 109, no. 185006, p. 185006, 2012.

[45] R. A. Snavely, M. H. Key, S. P. Hatchett, I. E. Cowan, M. Roth, T. W. Phillips, M. A. Stoyer, E. A. Henry, T. C. Sangster, M. S. Singh, S. C. Wilks, A. MacKinnon, A. Offenberger, D. M. Pennington, K. Yasuike, A. B. Langdon, B. F. Lasinski, J. Johnson, M. D. Perry, and E. M. Campbell, "Intense high-energy proton beams from petawatt-laser irradiation of solids," *Physical Review Letters*, vol. 85, pp. 2945–2948, 2000.

[46] Tech-X, "Vsim." Website, 2015. `http://www.www.txcorp.com`.

[47] T. Boyd, J. Sanderson, and E. Zita, *The Physics of Plasmas*, vol. 74. Cambridge University Press, 2006.

[48] R. O. Dendy, *Plasma dynamics*. New York: Oxford University Press Inc., 1990.

[49] P. Mulser and D. Bauer, *High Power Laser-Matter Interaction*, vol. 238. Springer-Verlag Berlin Heidelberg, 2010.

[50] W. H. Kegel, *Plasmaphysik*. Heidelberg: Springer-Verlag Berlin Heidelberg 1998, 1998.

[51] V. Karpman, vol. 1. Akademie Verlag Berlin, DDR, 1977.

[52] Y. B. Zel'dovich and Y. P. Raizer, *Physics of Shock Waves and High-Temperature Hydrodynamic Phenomena*. Dover Publishing Inc., 2002.

[53] A. Henig, S. Steinke, M. Schnürer, T. Sokollik, R. Hörlein, D. Kiefer, D. Jung, J. Schreiber, B. M. Hegelich, X. Q. Yan, J. Meyer-Ter-Vehn, T. Tajima, P. V. Nickles, W. Sandner, and D. Habs, "Radiation-pressure acceleration of ion beams driven by circularly polarized laser pulses," *Physical Review Letters*, vol. 103, p. 245003, 2009.

[54] E. Rebhan, *Theoretische Physik: Relativitätstheorie und Kosmologie*. Springer-Verlag Berlin Heidelberg, 2012.

[55] T. Fliessbach, *Allgemeine Relativitätstheorie*, vol. -1. Springer Spektrum, 2012.

[56] E. Freitag and R. Busam, *Funktionentheorie 1*, vol. 4. Springer, 2006.

[57] A. Taflove and S. C. Hagness, *Computational Electrodynamics: The Finite-Difference Time-Domain Method*, vol. 3. Artech House Inc., 2015.

[58] S. D. Gedney, *Introduction to the Finite-Difference Time-Domain (FDTD) Method for Electromagne*, vol. 3. Morgan & Claypool Publishers, 2011.

[59] T. Esirkepov, "Exact charge conservation scheme for Particle-in-Cell simulation with an arbitrary form-factor," *Computer Physics Communications*, vol. 135, pp. 144–153, 2001.

[60] K. Oswatitsch, *Grundlagen der Gasdynamik*, vol. 1. Springer, 2013.

[61] J. D. Anderson Jr., *Fundamentals of Aerodynamics*, vol. 5. Springer, 2011.

[62] C. A. J. Palmer, J. Schreiber, S. R. Nagel, N. P. Dover, C. Bellei, F. N. Beg, S. Bott, R. J. Clarke, A. E. Dangor, S. M. Hassan, P. Hilz, D. Jung, S. Kneip, S. P. D. Mangles, K. L. Lancaster, A. Rehman, A. P. L. Robinson, C. Spindloe, J. Szerypo, M. Tatarakis, M. Yeung, M. Zepf, and Z. Najmudin, "Rayleigh-Taylor instability of an ultrathin foil accelerated by the radiation pressure of an intense laser," *Physical Review Letters*, vol. 108, no. 22, 2012.

[63] S. V. Bulanov, E. Y. Echkina, T. Z. Esirkepov, I. N. Inovenkov, M. Kando, F. Pegoraro, and G. Korn, "Unlimited energy gain in the laser-driven radiation pressure dominant acceleration of ions," *Physics of Plasmas*, vol. 17, no. 6, 2010.

[64] S. S. Bulanov, C. B. Schroeder, E. Esarey, and W. P. Leemans, "Optimized laser pulse profile for efficient radiation pressure acceleration of ions," in *AIP Conference Proceedings*, vol. 1507, pp. 785–790, 2012.

[65] P. Schmidt, O. Boine-Frankenheim, and P. Mulser, "Optimum laser parameters for 1d radiation pressure acceleration," *Laser and Particle Beams*, vol. FirstView, pp. 1–10, 6 2015.

[66] P. Schmidt and O. Boine-Frankenheim, "A gas-dynamical approach to radiation pressure acceleration," *Physics of Plasmas*, vol. x, p. Publication in progress, 2015.

[67] G. B. Whitham, *Linear and Nonlinear Waves*, vol. 28. John Wiley & Sons Inc., 1974.

[68] W. A. Strauss, *Partielle Differentialgleichungen*. Wiesbaden: Springer Fachmedien, 1995.

[69] D. Meschede, *Gerthsen Physik*. Springer Spektrum, 2015.

[70] L. Debnath, *Nonlinear Partial Differential Equations*, vol. 3. Birkhäuser, 2012.

[71] R. Courant and K. Friedrichs, *Supersonic flow and shock waves*, vol. 5. Springer-Verlag Berlin Heidelberg New York, 1999.

[72] T. Schlegel, N. Naumova, V. T. Tikhonchuk, C. Labaune, I. V. Sokolov, and G. Mourou, "Relativistic laser piston model: Ponderomotive ion acceleration in dense plasmas using ultraintense laser pulses," *Physics of Plasmas*, vol. 16, p. 083103, 2009.

[73] P. Schmidt, O. Boine-Frankenheim, and P. Mulser, "Laser induced focusing for over-dense plasma beams," *Physics of Plasmas*, vol. 22, p. 093120, 2015.

[74] R. Hertel, "Theory of the inverse Faraday effect in metals," *Journal of magnetism and magnetic materials*, vol. 303, pp. L1–L4, 2006.

[75] M. C. Levy, S. C. Wilks, M. Tabak, S. B. Libby, and M. G. Baring, "Petawatt laser absorption bounded," *Nature Communications*, vol. 5, p. 4149, 1 2014.

Peter Schmidt – Curriculum Vitae

Address	Kirchstr. 21, 64283 Darmstadt, Germany	Office Phone eMail	+49 6151 16 24034 schmidt@temf.tu-darmstadt.de

Date of Birth	16.01.1987, Wiesbaden
Nationality	German
Marital Status	Single

Education

Dec. 2013 – present	PhD Candidate, TU Darmstadt Institute for computational electromagnetics (TEMF), Darmstadt, Germany Field of research: Radiation Pressure Acceleration and advanced transport; Awarded with Letter of Recognition by committee of the 34th International Workshop on High Energy Density Physics in Hirsch, Austria (Jan. 31st 2014) for outstanding achievements
Mar. 2011 – Nov. 2013	Master of Science in Engineering Physics, TU Darmstadt, focus: MHD and plasma physics, final grade 1.3 Master Thesis: Transport and focusing of laser accelerated ion beams (grade 1.7)
Oct. 2006 – Mar. 2011	Bachelor of Science in Physics, TU Darmstadt, focus: Hydrodynamics & MHD, final grade 2.6 Bachelor Thesis: Regularization of the MHD Rayleigh Problem (grade 1.3)
Sept. 1993 – Jun. 2006	Abitur, Taunusschule, Bad Camberg, major subjects: Physics and Chemistry, final grade 1.4 & Award for outstanding performance in science classes by DPG (German physicists association)

Work experience

Dec. 2013 – present	PhD Candidate at TU Darmstadt Institute for computational electromagnetics (TEMF), Darmstadt, Germany Field of research: Analytical and numerical investigation of the plasma dynamics appearing at Radiation Pressure Acceleration. Development of analytic laws for target and laser requirements, development of laser driven focusing method for over-dense plasma sheets
May 2006 – Nov. 2013	Private/extra lessons teacher for math, physics, chemistry, geology, history, biology, engineering (school and university), Bad Camberg, Germany
Aug. 2006 – Sept. 2006	Laborer at A.M. Ramp & Co. GmbH (Ruco) in locksmithery, Eppstein, Germany
Mar. 2004 – Apr. 2004	Trainee at Aventis, Hoechst, Germany Assistant in insulin QA laboratory

Grants and Scholarships

Dec. 2012 – present	HGs-HIRe, traveling money scholar ship for PhD students
Dec. 2012 – present	HIC for FAIR, PhD students scholarship
Mar. 2011 – Nov. 2012	W. u. E. Heraeus Stiftung, scholarship for traveling money

Computer and Software Skills (EDP)

Operating systems	Windows (excellent skills in all distributions), Linux (basic skills)
Office	MS Office (excellent skills in all packages), OpenOffice (excellent skills), HTML (moderate Skills), LATEX (excellent skills)
Programming	Delphi (Object Pascal, advanced skills), Python 2.x/3.x (moderate skills, including science packages), Basic (basic skills)

Scientific Computing	Wolfram Mathematica (excellent skills), Matlab & Simulink (advanced skills), common CAD software (excellent skills), CST Studio (EM computation, excellent Skills), Siemens NX (excellent skills)
Other	μController programming (moderate skills with Atmel AVR's)

Language Skills

German	Native
English	Fluent in speaking and writing
Latin	Basic skills

Peer-reviewed Publications

P. Schmidt, O. Boine-Frankenheim and P. Mulser, *Optimum laser parameters for 1D radiation pressure acceleration*, Laser and Particle Beams, **33**, pp 387-396 (2015)

P. Schmidt, O. Boine-Frankenheim and P. Mulser, *Laser induced focusing for over-dense plasma beams*, Physics of Plasmas, **22**, 093120 (2015)

P. Schmidt, O. Boine-Frankenheim, *A gas-dynamical approach to radiation pressure acceleration*, Physics of Plasmas, **23**, 063106 (2016)

Index